DETECTING INDIVIDUAL TREES FROM LIDAR

Anahita Khosravipour

Graduation committee:

Chairman/Secretary

Prof. dr. ir. A. Veldkamp	

Supervisor

Prof.dr. A.K. Skidmore	University of Twente

Co-supervisor

Dr. Y.A. Hussin	University of Twente

Members

Prof.dr.ir. A. Veldkamp	University of Twente
Prof.dr. M.G. Vosselman	University of Twente
Prof.dr. P. Krzystek	Hochschule Munchen
Prof.dr. I.H. Woodhouse	University of Edinburgh
Dr. M. Isenburg	Rapidlasso GmbH

ITC dissertation number 309
ITC, P.O. Box 217, 7500 AE Enschede, The Netherlands

ISBN 978-90-365-4396-5
DOI 10.3990/1.9789036543965

Cover designed by Benno Masselink
Printed by ITC Printing Department

UNIVERSITY OF TWENTE.

FACULTY OF GEO-INFORMATION SCIENCE AND EARTH OBSERVATION

DETECTING INDIVIDUAL TREES FROM LIDAR

DISSERTATION

to obtain
the degree of doctor at the University of Twente,
on the authority of the rector magnificus,
prof.dr. T.T.M. Palstra,
on account of the decision of the graduation committee,
to be publicly defended
on Friday 29 September 2017 at 12:45 hrs.

by

Anahita Khosravipour

born on 14 September, 1982

in Tehran, Iran

This thesis is approved by
Prof.dr. A.K. Skidmore, supervisor
Dr. Y.A. Hussin, co-supervisor

“The world is my country and science is my religion”

Christiaan Huygens

Acknowledgements

This PhD research has been a challenging and amazingly adventurous journey for me over these past few. This work would not have been possible without the support of my family members but also particularly that of my ITC family.

First and foremost, I would like to express my sincere thanks and highest appreciation to my promoter and supervisor, Prof. Dr. Andrew Skidmore. “Andrew, thank you!”. Thank you for giving me the opportunity to undertake the PhD and making me feel welcome in this little beautiful country. Thank you for your continuous support and for always being patient with encouraging about my progress. I have learned a lot from you that not only has an ineffable reflected on my scientific career but is also reflected in my daily life. You taught me an analytic way to think and the philosophy of science. Your positive attitude always encouraged me to continue and not to give up whenever I faced seemingly insurmountable obstacles.

I am extending profound thanks to my co-promoter, Dr. Yousif Hussin for his guidance and encouragement in all respects of my PhD. His advice and support helped evolve my research. Dear Yousif, Thank you for your valuable assistance and motivation starting from the first day of my PhD until my last day at ITC. I will always remember your warm smile and your kindness that motivate me from the first day.

I owe my sincere gratitude to Dr. Martin Isenburg from rapidlasso GmbH, for his guidance, support and engorgement during my PhD. You really taught me what LiDAR “is” and how to intuitively “feel” the point clouds! You patiently taught me each step of the LiDAR data processing pipeline and brainstormed with me during any free time that we found at conferences. Your advice and your critical reviews were extremely helpful in enhancing the quality of my research and without your valuable support this thesis would have been very difficult to complete. I felt extremely comfortable and enjoyed working with you through the long journey of my PhD. Thank you also for also giving me the opportunity to volunteer as your assistance teacher at various international summer schools and for

introducing me to many of the most famous LiDAR scientist around the world.

A heartfelt thanks to Eva Skidmore, who not only did excellent English editing to publish my papers and thesis but also for her great support throughout my stay in Enschede. Special thanks are extended to all staff members of NRS department for their support throughout my study. I am particularly indebted to Esther Hondebrinks for patiently arranging all my meeting and for friendly helping me with every little problem whenever I faced. I also extend a spatial thanks to Job Duim and Benno Masselink for their support and dealing with my requests, especially for poster preparations.

I would like to thank everyone at ITC who support me from my first correspondence with ITC until the end; from Adrie Scheggetman, Loes Colenbrander and Paul van Dijk and who coordinated my graduate program, from Thereza van den Boogaard and Marie Chantal Metz who have always immediately handled all my bureaucracy in the Netherlands and made my life easier at ITC. Special thanks to the ITC helpdesk, Gerrit Polman and Aiko Mulder, for solving all my computer problems. My debt of gratitude is also to the library staff, Marga Koelen, Carla Gerritsen and Desirée Snoek, who worked hard to make accessible all the books and papers that I requested. I would like to thank the department of finances, Tonny Boeve and Marion Pierik for handling all my financial problems. Many thanks to Roelof Schoppers for happily greeting me every morning during these years. I am also grateful to the entire ITC International Hotel members, Saskia Groenendijk, Patrick Hartlief, Anneloes Lammerink, for making me feel at home while I was away.

The last but not least, my family. This PhD would not have been undertaken without the financial and emotional support of my parents and my lovely brother whom I am deeply indebted. Mum, dad, “thank you”! Thank you for your unwavering love and support in any stage of my life. Thank you for your motivation and your words: “Ani, you can DO IT!”, that helped me to be stronger and didn’t allow me to give up in all the difficulties that I have faced. You are the best mum and dad I could ever wish for. Thank you for being in my life.

Table of Contents

List of figures

List of tables

Chapter 1

General Introduction

1.1 Importance of forest inventory

Forest inventory deals with the methods of obtaining detailed and accurate information about forest composition and structure (Spurr, 1951). Forest structure is described by various attributes associated with spatiotemporal properties of forest stands, such as height, diameter at breast height (DBH), canopy closure and volume (Latifi et al., 2015). These forest inventory are an important source of information for a variety of strategic and tactical forest management purposes, including silviculture (Pond et al., 2014), ecological restoration (Benayas et al., 2009), wildland fire risk assessment (Morsdorf et al., 2004; Pierce et al., 2009), biomass estimation and carbon stock management (Brown, 2002; Nelson et al., 1988; Patenaude et al., 2005), as well as assessment of biodiversity and habitat (Martinuzzi et al., 2009; Turner et al., 2003). Remote sensing techniques have become an integral part of forest inventory to provide accurate and timely forest and tree characteristics at different scales to support this variety of forest management purposes (Latifi, 2012; White et al., 2016; Zhang et al., 2014).

1.2 LiDAR remote sensing technology of forest inventory

Among remote sensing techniques, small-footprint airborne laser scanning (ASL), also known as airborne LiDAR (Light Detection And Ranging), has rapidly gained popularity in forest inventory, due to its unique capability to measure the 3D structural information of trees directly (Hyyppä et al., 2008; Lim et al., 2003b; White et al., 2016).

The two main strategies for using LiDAR data in forest inventories are the area-based approach (ABA) and individual tree detection (ITD) (Hyyppä et al., 2012). ABAs rely on statistical principles and predict forest attributes based on parametric regression or nonparametric imputation models built between using field measured variables and features derived from LiDAR data (Kathuria et al., 2016; Næsset, 2002). For instance, in ABAs statistical features, such as percentiles of laser canopy height distribution, are used as predictors in a model-based framework to estimate forest height characteristics in a certain sampling area (e.g., raster grid cell

or segment) (Nelson et al., 1988; Vastaranta et al., 2011). ABAs can perform well under low LiDAR point densities and are currently applied in operational forest inventory to provide a wall-to-wall estimation of forest attributes at stand-level (Zhang et al., 2014). In ITD approaches, an initial take is to detect the trees. Then, the ITDs measure or predict tree-level variables, such as height and volume, from LiDAR data and aggregate them to obtain stand-level forest inventory results (Vastaranta et al., 2011). ITD approaches have an advantage over ABAs regarding improving the prediction of species-specific forest attributes (Yao et al., 2012) and the prediction of timber assortments (Kathuria et al., 2016; Vastaranta et al., 2011; Zhang et al., 2014). Another advantage of ITCs is that they can reduce the amount of or potentially even replace the expensive fieldwork required for ABAs (Hyyppä et al., 2008; Vastaranta et al., 2012). Therefore, ITD approaches have attracted more attention in the LiDAR research community than ABA approaches (Duncanson et al., 2014; Hyyppä et al., 2012; Jing et al., 2012a; Koch et al., 2006; Li et al., 2012; Lu et al., 2014; Mongus and Žalik, 2015; Popescu and Wynne, 2004; Reitberger et al., 2009b).

1.3 LiDAR technology of individual tree detection

The key point in ITD approaches (including treetop detection and crown delineation) is the detection of trees from LiDAR data. Hyyppä and Inkinen (1999) and Persson et al. (2002) were among the first to prove the potential effectiveness of airborne LiDAR systems for the recognition of single trees. Numerous ITD approaches have been developed in the past, such as Region Growing (Hyyppä et al., 2001), Watershed (Chen et al., 2006) and Normalized Cut (Yao et al., 2012). These methods have the initial identification of local maxima (i.e. treetops) in common, based on geometric information from LiDAR data (Duncanson et al., 2014; Mongus and Žalik, 2015; Vastaranta et al., 2011; Véga and Durrieu, 2011; Zhang et al., 2014). The initial step in such a method relies on the generation of a Digital Surface Model (DSM) or normalized Digital Surface Model (nDSM), describing the geometry of the uppermost layer of the canopy (Hyyppä et al., 2008). ITD approaches identify the local maxima in the generated DSM (or nDSM) that are considered to correspond to the

positions of the treetops. Subsequently, the local maxima are used as reference points (or seed points) for crown segmentation and height estimation (Véga and Durrieu, 2011). Even though many successful results have been reported in the literature in terms of individual tree detection, some issues remain to be resolved.

1.3.1 Challenges regarding Individual Tree Detection

The main challenge faced when implementing an ITD approach is that the accuracy of detection can be strongly affected by the quality of the DSM (or nDSM) derived from the LiDAR data (Hyyppä et al., 2008). With ITD approaches, either the LiDAR-derived DSM, which is a raster image interpolated from LiDAR points depicting the uppermost layer of the canopy (Chen et al., 2006; Duncanson et al., 2014; Heurich, 2008; Jing et al., 2012a; Wu et al., 2016), or the original LiDAR raw data point clouds can be used (Ferraz et al., 2012; Li et al., 2012; Lu et al., 2014; Reitberger et al., 2009b; Yao et al., 2012).

The major advantage of using point cloud-based methods is that all LiDAR returns can be used so that no information is omitted (Duncanson et al., 2014). However, such point cloud-based ITD techniques are computationally demanding and limited to small areas, thus may not be applicable across a larger range of forest types (Duncanson et al., 2014; Hu et al., 2014; Mongus and Žalik, 2015; Wu et al., 2016). Irrespective of whether the ITD approaches are based on a raster DSM or the point cloud, most ITDs require a high density of laser pulse footprints (Lefsky et al., 2002). Augmenting the density of laser pulse footprints increases the chance of the laser sampling the “true” treetop (Chen et al., 2006).

Typically, a high-resolution DSM raster has been generated by interpolating all first returns of LiDAR, often by Delaunay triangulating their x-y coordinates into a Triangulated Irregular Network (TIN) (Axelsson, 1999; Khosravipour et al., 2015; Van Leeuwen et al., 2010; Wu et al., 2016). Nevertheless, any 2D interpolation of first returns will struggle to produce a realistic representation of the canopy surface when there are first returns that have very similar x-y coordinates but very different z values (Axelsson, 1999). When triangulated into a TIN, such

variations will form needle-shaped triangles that appear as *spikes* and result in pixels with unnaturally low values called *data pits* – or simply *pits* – when the TIN is rasterized (Khosravipour et al., 2016). Intuitively, pits or spikes form and appear whenever the laser beam penetrates deeply into a tree crown, hitting a lower branch or the ground instead of uppermost vegetation layer before producing a first return. These geometric irregularities often turn the corresponding DSM rasters into extremely jagged surfaces, which subsequently reduce the accuracy of tree detection by increasing the omission (undetected tree) and commission (falsely detected) errors. For example, Persson et al. (2002) stated that data pits create difficulties for recognizing separate tree crowns, while Gaveau and Hill (2003) claimed that data pits cause canopy height underestimation (especially of small trees), due to the omission of treetops. Alternative suggestions have been to generate a canopy surface regular grid, recording either the maximum laser elevation value (Chen et al., 2006) or the last LiDAR return (Hyyppä et al., 2012) for each cell. However, both these options struggle to produce a reliable high-resolution representation of the canopy surface.

In order to improve the accuracy of tree detection, a number of studies have recommended applying image smoothing methods (e.g., Gaussian filter) by removing data pits or/and irrelevant local maxima (Brandtberg et al., 2003; Persson et al., 2002; Yu et al., 2011). However, all pixels of a DSM are altered when smoothing their values with respect to their nearest neighbors. Subsequently, smoothed DSMs often underestimate the true tree height due to the omission of treetops, especially with small and suppressed trees (Eysn et al., 2015; Hyyppä et al., 2000; Solberg et al., 2006).

A number of studies indicate that various forest conditions (e.g., crown size, age, tree species, forest density, site type and steep terrain) can also significantly influence the quality of DSMs and thereby the performance of ITD approaches (Falkowski et al., 2008; Pitkänen et al., 2004; Popescu and Wynne, 2004; Vauhkonen et al., 2012a; Yu et al., 2011). For example, complex forest terrain presents a challenging problem whenever a height-normalized DSM – also known as Canopy Height Model (CHM) – is

produced for tree detection. A CHM, is typically created by subtracting the Digital Terrain Model (DTM) from the DSM (Lim et al., 2003b). The CHM represents absolute canopy height above the bare-earth terrain surface. However, complex forest terrain affects the performance of the height normalization step by distorting the CHM, thus possibly reducing the accuracy of tree detection (Vega et al., 2014). On steep slopes, the raw elevation values located, for example, on either the downhill or the uphill part of a tree crown are height-normalized with parts of the DTM that may be much lower or higher than the tree stem base, respectively (Breidenbach et al., 2008). Therefore, in the CHM, the downhill part of the crown will "rise" while the uphill part will "sink", causing the entire tree crown to be systematically distorted. In tree detection, a "rising" branch overhanging lower terrain in the downhill part can turn into a "false" local maximum at some distance from the true treetop. Considering the location of such a "false" local maximum as the actual treetop negatively effects subsequent crown delineation and height estimation.

1.4 General research objectives

The aim of this study is to develop a new approach to generate a high-quality LiDAR-derived DSM that improves the accuracy of individual tree detection. The specific objectives of this study are as follows.

(1) To develop a new "pit-free" algorithm that is able to remove pits efficiently and generate a pit-free CHM (nDSM) raster (after elevations have been normalized)
(2) To quantify the effect of the slope gradient on the accuracy of treetop detection when using a pit-free LiDAR-derived CHM.
(3) To develop a novel "spike-free" algorithm that generates a DSM with the highest possible resolution using all relevant LiDAR returns (without needing to normalize the elevations).
(4) To assess the accuracy of treetop detection using a DSM generated with the spike-free algorithm for different types of forests and LiDAR point densities.

1.5 Outline

This thesis consists of four main chapters, each aiming to fulfill part of the objective of this study: to improve the accuracy of tree detection using airborne LiDAR data.

Chapter 1 is a general introduction to the study. Chapter 2 aims to present a new "pit-free" algorithm able to create a pit-free CHM raster by using subsets of LiDAR points to close pits. In order to demonstrate the robustness of the algorithm for generating a CHM, the algorithm has been applied to both a high- and low- LiDAR point density datasets. The pit-free CHMs derived from LiDAR datasets were evaluated by assessing and comparing the accuracy of individual treetop detection using smoothed first-return CHMs.

Chapter 3 aims to theoretically and experimentally quantify the effect of slope on the accuracy of treetop detection when using a pit-free LiDAR-derived CHM. First, we present a simplified theoretical model to illustrate how the normalization causes a systematic error in CHM-based treetop detection when an individual tree is located on sloping terrain. Then, we assess the accuracy of treetop detection by using both the CHM/nDSM (i.e. with the normalized elevations) and the DSM (i.e. with original elevations). Finally, we compute the positional difference between the same treetop detected in both the CHM and the DSM, in order to investigate the influence of the slope on the horizontal displacement of CHM-detected trees as well as its effect on subsequent height estimation.

Chapter 4 endeavors to present a novel "spike-free" algorithm that can generate a spike-free DSM at the highest resolution supported by the LiDAR. The algorithm considers all relevant LiDAR returns (instead of only first returns) and systematically prevents the formation of spikes during the TIN construction. This new algorithm is evaluated by comparing the results of treetop detection using the generated spike-free DSM with those achieved using a common first-return DSM.

In Chapter 5 the accuracy is assessed of treetop detection using a DSM generated with the spike-free algorithm for different types of forest (a temperate plantation, a temperate mixed deciduous-coniferous forest and

a tropical rainforest) at different LiDAR point densities (low, moderate and high). We also evaluate the accuracy of treetop detection using a DSM generated with the spike-free algorithm compared to the accuracy using DSMs generated by interpolating first-return, highest-return, and last-return LiDAR points.

The thesis concludes with Chapter 6, describing the interrelationship between all chapters and posing suggestions for future research.

Chapter 2

Generating pit-free canopy height models from airborne LiDAR*

* This chapter is based on:
Khosravipour, A., Skidmore, A.K., Isenburg, M., Wang, T., Hussin, Y.A., 2014. Generating Pit-free Canopy Height Models from Airborne Lidar. *Photogrammetric Engineering & Remote Sensing*, 80, 863-872

Khosravipour, A., Skidmore, A.K., Isenburg, M., Wang, T., Hussin, Y.A., 2014. Development of an algorithm to generate a Lidar pit - free canopy height model. *In: Proc. Silvilaser2013 : 13th International conference on Lidar applications for assessing forest ecosystems*, Beijing, pp. 125-128.

Abstract

Canopy height models (CHMs) derived from LiDAR data have been applied to extract forest inventory parameters. However, variations in modeled height cause data pits, which form a challenging problem as they disrupt CHM smoothness, negatively affecting tree detection and subsequent biophysical measurements. These pits appear where laser beams penetrate deeply into a tree crown, hitting a lower branch or the ground before producing the first return. In this study, we develop a new algorithm that generates a pit-free CHM raster, by using subsets of the LiDAR points to close pits. The algorithm operates robustly on high-density LiDAR data as well as on a thinned LiDAR dataset. The evaluation involves detecting individual trees using the pit-free CHM and comparing the findings to those achieved by using a Gaussian smoothed CHM. The results show that our pit-free CHMs derived from high- and low-density LiDAR data significantly improve the accuracy of tree detection.

2.1 Introduction

The use of airborne Light Detection and Ranging (LiDAR) has been increasing in forestry. LiDAR is capable of providing accurate three-dimensional information on forest structure (Lim et al., 2003a), contributing significantly to the improved accuracy of forest inventories (Magnussen et al., 2010; Yu et al., 2011) and subsequent biophysical parameters such as biomass (Nelson et al., 1988; Popescu, 2007).

Typically, a LiDAR-derived Canopy Height Model (CHM) or a normalized Digital Surface Model (nDSM) is used for extracting relevant forest inventory information, such as detecting single trees for subsequent height estimation and crown delineation (Bortolot and Wynne, 2005; Forzieri et al., 2009). The CHM represents absolute canopy height above ground and it is typically calculated by interpolating the first return LiDAR points and determining their height above a digital terrain model. (Hyyppä et al., 2008; Van Leeuwen et al., 2010). Tree height measurement and crown delineation mainly rely on the identification of local maxima, with each local maximum corresponding to the location of an individual treetop and the surrounding segments forming the tree crown (Véga and Durrieu, 2011). Therefore, to be able to extract relevant structural parameters of trees (e.g. tree height) the correct location of single trees in the CHM is of fundamental importance (Chen et al., 2006; Persson et al., 2002; Yao et al., 2012). While some researchers have tried to find local maxima directly in the LiDAR points (Li et al., 2012), most operational users of LiDAR first calculate a raster CHM from the first return LiDAR points and then extract local maxima from that raster CHM (Hyyppä et al., 2008; Lim et al., 2003b).

The main challenges faced in treetop detection are commission errors (falsely detected trees) and omission errors (undetected trees) (Hosoi et al., 2012; Pouliot et al., 2005). These errors are mainly attributed to natural variation in tree crown size (Pitkänen et al., 2004) as well as to height irregularities within individual tree crowns in the input CHM (Solberg et al., 2006). To address natural variation in crown size, researchers have developed processing methods that adapt to the crown (object) size. Pitkänen et al. (2004) developed and tested three different adaptive

methods for individual tree detection based on canopy differences. Wulder et al. (2000) proposed the use of a local maxima filter with variable window sizes. However, if the selected window size is smaller or larger than the crown size, then the commission or omission error, respectively, will increase. In order to select the correct window size, Popescu and Wynne (2004) introduced an adaptively varying window technique, based on the idea that a moving local maxima filter should be adjustable to an appropriate width to account for different crown sizes.

To address irregularities in crown height, a number of researchers have suggested pre-processing CHMs to reduce commission and omission errors (Bortolot and Wynne, 2005; Brandtberg et al., 2003; Chen et al., 2006; Solberg et al., 2006).

Irregularities in canopy surface elevation, also called "data pits", form a challenging problem due to their disruptive influence on a CHM, reducing accuracy in tree detection and subsequent biophysical measurements (Ben-Arie et al., 2009; Gaveau and Hill, 2003; Zhao et al., 2009). For example, Shamsoddini et al. (2013) indicated that data pits may significantly affect the estimation of structural forest parameters, especially basal area and stand volume. Since the processing of raw LiDAR point clouds into a meaningful raster is a composition of many different procedures, there is no unified agreement on the cause of data pits. Axelsson (1999) found that some information from raw point clouds with similar *xy*-coordinates and different *z* values is lost when the points are interpolated into a raster. Such lost data become significant when multiple echoes are registered in a forested area. Ben-Arie et al. (2009) and Véga and Durrieu (2011) stated that the problem of data pits was due to laser scanning processing and/or post-processing of LiDAR point clouds. Data pits may also occur during classification of LiDAR point clouds into ground and non-ground points when creating a Digital Surface Model (DSM) or a Digital Terrain Model (DTM), depending on classification technique and LiDAR point density (Kraus and Pfeifer, 1998). Leckie et al. (2003) called such data pits "holes" and found them to be caused by merging different LiDAR flight lines and by laser beams penetrating through canopy branches and foliage to the ground below. Persson et al. (2002) stated that LiDAR penetration caused

"large height variations" within single tree crowns, creating difficulty in recognizing separate crowns. Gaveau and Hill (2003) reported the penetration of laser beams into a tree crown to be the cause of canopy height underestimation. Zhao et al. (2013) described data pits as "invalid values" or "abnormal elevation changes", which formed unnatural gray or black holes in CHM images. Many studies have claimed that LiDAR-derived tree parameters (e.g. height and crown diameter) may be misinterpreted due to the pits present in the CHM image (Gaveau and Hill, 2003; Persson et al., 2002).

A number of studies have recommended image smoothing, using methods such as a mean, median or Gaussian filter to reduce the data pits (Brandtberg et al., 2003; Hosoi et al., 2012; Persson et al., 2002; Yu et al., 2011). Typically, image smoothing consists of a two-dimensional (2D) isotropic kernel function, as widely used on 2D remote sensing images (Dralle and Rudemo, 1996) in order to remove "impulse noise" including salt-and-pepper noise and random-valued noise (Chan et al., 2005). However, the use of this technique is not appropriate when processing CHMs derived from highly accurate three-dimensional (3D) LiDAR data, because all pixels are altered when smoothing their values according to their nearest neighbors (Ben-Arie et al., 2009; Zhao et al., 2013). Smoothing methods have underestimated true tree height (especially of small trees) (Hyyppä et al., 2000), due to the omission of treetops, as well as underestimated crown radius, due to the reduction of crown shoulders (Solberg et al., 2006). Consequently, such errors reduce the accuracy of forest biomass and carbon estimations.

Other researchers have proposed different methods for removing data pits. Leckie et al. (2003) and Popescu and Wynne (2004) recommended that only the highest first return in each cell (pixel) be used, instead of using all first LiDAR returns that penetrate the crown. Chen et al. (2006) suggested using a large cell size to minimize height variation within crowns. However, large cell sizes (e.g. > 0.5 m) reduce the potential accuracy of the crown boundary. Ben-Arie et al. (2009) introduced a semi-automated pit-filling algorithm to fill the data pits. In this algorithm, a Laplacian filter is applied to the original CHM to find pits with a user-

defined threshold (visual decision). Evaluation of different threshold ranges indicated that choosing an incorrect threshold would cause an omission (under-filling) or commission error (over-filling). Zhao et al. (2013) improved the method proposed by Ben-Arie et al. (2009) by adding a morphological crown control threshold in order to minimize the overfilling problem. They assumed the crown shape of both coniferous and deciduous forest trees to be near circular. However, the algorithm could not remove all pits, especially not when a lower branch or leaf inside the canopy was encountered, rather than the ground. Shamsoddini et al. (2013) developed an adaptive mean filter method using variable window sizes in order to fill the pits. However, it is difficult to select an optimal window size that results in high accuracy for all tree structural parameters.

Due to advances in LiDAR technology, survey data with very high point densities (i.e. ~50 point/m^2 or more) have become available. Researchers have found that such high-resolution point clouds allow them to extract detailed data on forest structure (Holmgren et al., 2008; Hyyppä et al., 2001; Li et al., 2013). However, as it is very costly to obtain such high-density LiDAR data for large forested areas, the data sets used in practice often are of much lower density (e.g. 4 point/m^2 or less). Although less accurate, these low density data are used at canopy, as well as at individual tree level (Ke et al., 2010; Popescu, 2007; Yu et al., 2011). It is, therefore, useful to develop a pit removal algorithm that generates accurate CHMs without data pits for both high and low LiDAR point densities.

In this study, we present a new "pit-free" algorithm able to create a pit-free CHM raster. The specific objectives of this study are (1) to evaluate the applicability of the algorithm at different LiDAR point densities; (2) to evaluate pit-free CHMs by visual comparison with smoothed CHMs derived with a standard Gaussian smoothing technique (Dralle and Rudemo, 1996); and (3) to assess and compare the accuracy of individual tree detection using both the smoothed and the pit-free CHMs. To our knowledge, this is the first study that rigorously investigates how the removal of data pits from CHMs affects treetop detection.

2.2 Materials

2.2.1 Study area

The Bois Noir (black wood) forest forms part of the Barcelonnette basin, which is located in the southern French Alps (44° 23′ N, 6° 45′ E). The Barcelonnette basin is characterized by the Mediterranean climatic and geomorphological conditions observed in the southern French Alps (Flageollet et al., 1999). The size of the study area is about 1.3 km^2 and mainly covered by coniferous plantation forests and grasslands, all within an elevation range of 1400 to 2380 m above sea level. The forest predominantly consists of mountain pine (*Pinus uncinata*) and scots pine (*Pinus sylvestris*) plus a few *Larix decidua* and occasional deciduous trees (*Populus tremula and Fraxinus excelsior*).

2.2.2 Field measurements

Field inventory data were collected during two weeks in both September 2011 (seven plots) and September 2012 (48 plots). Stratified random sampling determined the position of the circular plots (r = 12.6 m), using a vegetation type map obtained from the French forest service (Office national des forêts, 2000). The vegetation map was superimposed on an aerial ortho-photograph and used in the field in order to improve visual interpretation. The measurements collected included tree location, tree height, tree crown diameter (CD), tree stem diameter at breast height (DBH) and tree species determination (Table 2.1). The total number of trees sampled was 694.

A Nikon hand-held laser rangefinder (electronically measuring distance and angle) was used for tree height measurement where the treetops could be seen. The DBH of all trees (larger than 7cm stem diameter at 1.3m above ground) within a plot was measured using a 60 cm caliper. The average crown diameter of the trees was measured in two perpendicular directions, as direct measurement proved difficult (Song et al., 2010).

In September 2011, the position of individual trees as well as the central point of each plot was recorded using the Leica 1200 Differential GPS System. A total station was used to measure tree positions where the

differential GPS signal was too weak due to canopy density. Setting up the geodetic base stations took a 24-hour period of static observation for each geodetic station (see Razak et al. (2011b) for more detail). Popescu (2007) reported that treetop positions may be determined with higher accuracy using a CHM image than with error-prone measurements derived from differential GPS in the field. Therefore, a printed CHM image (at a scale of 1:100) with 0.15 m pixel size was used in September 2012 to determine tree location where the differential GPS signal was too weak. Using the CHM technique for the 2012 fieldwork allowed us to survey many more plots in two weeks than in 2011.

Table 2.1: Descriptive statistics of the tree field measurements.

	All (n= 694)			deciduous (n= 33)			Larix (n= 29)			Pinus sylvestris (n=325)			Pinus uncinata (n=307)		
	DBH (cm)	Height (m)	CD (m)	DBH (cm)	Height (m)	CD (m)	DBH (cm)	Height (m)	CD (m)	DBH (cm)	Height (m)	CD (m)	DBH (cm)	Height (m)	CD (m)
Min	7	6	0.5	13	7	1.5	13	6.6	3.7	8	6	0.9	7	6	0.5
Max	61	25	9.1	43	24	6.3	61	25	8.9	59	23	9.1	41	25	6.7
Median	23	13.5	2.6	25	15.5	3.8	36	17.6	6	25	13	3.4	20	13.5	1.7
Mean	24.1	13.5	3	24.8	16.8	3.6	34.9	17.8	6.2	26	12.9	3.6	20.9	13.4	1.9
SD	8.2	3.2	1.6	9.4	6	1.3	10.5	4	1.4	8.5	3	1.4	5.4	2.4	0.9

2.2.3 LiDAR data

The LiDAR data and aerial photographs (0.15 m pixel size) were simultaneously acquired during the leaf-on season in July 2009 using a helicopter flying about 300 m above ground level (Table 2.2). A full-waveform airborne laser scanning system (RIEGL VQ-480), which was developed for surveying mountainous forested areas, was utilized by Helimap (Vallet and Skaloud, 2004). The system provides high-speed data acquisition using a fast line scanning mechanism and a narrow infrared laser beam. Moreover, the system performs on-line full waveform analysis (in hardware) to extract discrete returns from the waveforms. For our data set, the VQ-480 system used a laser pulse repetition rate of up to 300 kHz and recorded up to five returns for each pulse. The initial aim of this survey

was to accurately map complex landslides in forested terrain (Razak et al., 2011b). Therefore, to increase the point cloud density, the area was covered by seven flights. The mean point density was 160 point/m^2 with an average distance between laser points of 0.08 m.

Table 2.2: The airborne laser scanning characteristics.

Acquisition (month/year)	July- 2009
Laser scanner	Riegl VQ480i
IMU system	iMAR FSAS - record 500Hz
GPS system	Topcon legacy - record 5Hz
Laser pulse repetition rate	300 kHz
Measurement rate	Up to 150 000 s^{-1}
Laser wavelength	Near infrared
Beam divergence	0.3 mrad
Laser beam footprint	75 mm at 250 m
Field of view	60°
Scanning method	Rotating multi-facet mirror

There is a time difference between the collected data by LiDAR acquisition in July 2009 and the field measurements in September 2011 and 2012. However, our study area consists of mature forest and is characterized by relatively low temperatures during most of the year, which results in a relatively low tree growth rate. Therefore, we assume that the difference in tree height due to natural growth between the time of the LiDAR survey and the acquisition of ground data is negligible.

2.3 Methods

2.3.1 Preprocessing LiDAR data

Our original LiDAR dataset was stored separately in adjacent irregular tiles and classified into ground-points and non-ground-points. To avoid edge effects along tile boundaries (Brandtberg et al., 2003), the LiDAR points were retiled with a 25 meter buffer around each tile. This essentially moves potential artifacts into the tile buffer. Unlike other methods that create a raster CHM from the difference between two rasters (i.e. by subtracting the DTM raster from the DSM raster), our method first height-

normalized the raw LiDAR points and then generated a CHM raster. The LiDAR points were height-normalized by replacing the elevation of each point (i.e. the z coordinate) with its height above the ground. Consequently, the height of all returns classified as ground is zero. Afterwards, the ground returns were interpolated with a triangular irregular network (TIN) constructed through Delaunay triangulating (Isenburg et al., 2006a) the x and y coordinates in 2D. Then, the height of non-ground returns was computed as the vertical distance to the TIN (i.e. the distance in the z direction from the TIN to the points). These normalized LiDAR points were used as input for the pit-free algorithm, described in the following section. The preprocessing was implemented via batch-scripting the *lastile* and *lasheight* modules of LAStools (rapidlasso GmbH, 2013).

2.3.2 Description of pit-free algorithm

In this section, we describe how to efficiently generate a pit-free raster CHM from LiDAR point clouds. The pit-free algorithm comprises two stages. The first stage is to construct a standard CHM from all first returns and, most importantly, a number of partial CHMs from only those first returns that correspond to higher-up vegetation hits. The second stage is to combine all these CHMs into one CHM based on the highest value across all CHMs for each x and y raster position (Figure 2.1). This algorithm can easily be implemented in the command line with a batch script that uses an efficient combination of the *las2dem* and *lasgrid* modules of LAStools (rapidlasso GmbH, 2013).

2.3.2.1 Partial CHMs

Pits in the canopy appear whenever the laser beam is able to penetrate deeply through canopy branches before producing a first return. The depth and the distribution of pits in a standard CHM depend on the crown structure and the diameter of the laser beam as well as the sensitivity of the system processing the returning waveform (Gaveau and Hill, 2003). Instead of hitting the highest point of the canopy, the laser pulses may produce their first return when they hit a lower branch or even after they penetrate all the way through the crown to the ground. Hence, the depth of

different canopy pits varies greatly, making it impossible to use a fixed threshold to define (and potentially remove) them (Ben-Arie et al., 2009). To address this issue, a set of partial CHMs was computed by excluding all first returns below a certain height so that each CHM represents only some higher part of the canopy. The fundamental idea is to compute the shape of the canopy at different levels. The American Society for Photogrammetry and Remote Sensing (ASPRS) classifies LiDAR points into three layers: low vegetation (0.5 m < height ≤ 2.0 m), medium vegetation (2.0 m < height ≤ 5.0 m), and high vegetation (5.0 m < height) (ASPRS, 2008). We used a similar layering of the vegetation to construct our partial CHMs. All first return points were used to construct the first CHM (CHM_{00}). This CHM is the standard CHM that other researchers have typically generated from the first return LiDAR points (Hyyppä et al., 2008). The second CHM (CHM_{02}) was constructed by including first returns at a height of 2 and above. The first returns of ground level, low vegetation and medium vegetation were removed in the third CHM (CHM_{05}). The fourth CHM (CHM_{10}) and fifth CHM (CHM_{15}) were constructed by excluding first returns from heights less than 10 and 15 m, respectively (Figure 2.1). Distance intervals of 5 m, as used in this study, are called height thresholds and aim to preserve the original morphological structure of the tree crowns. We applied CHM_{00} to CHM_{15}, as only 5 % of the trees in the study area are taller than 20 m.

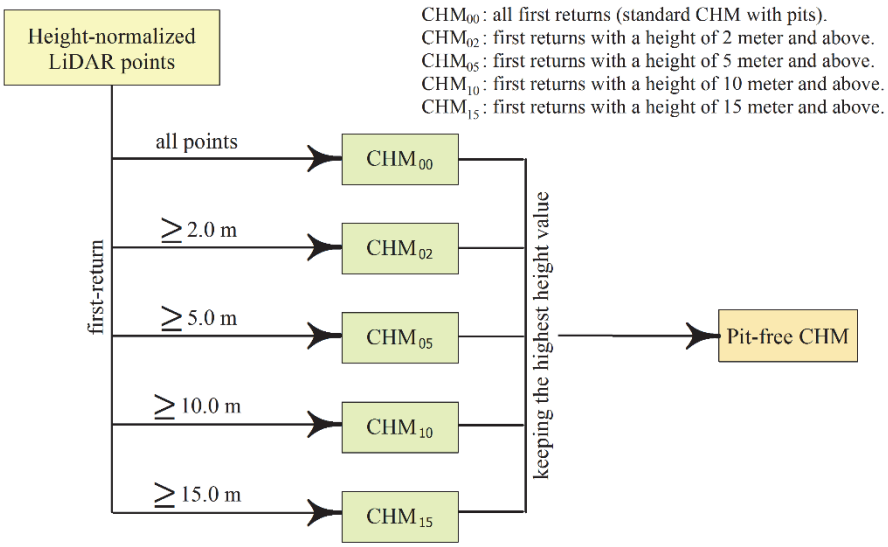

Figure 2.1: Diagram of pit-free algorithm methodology.

2.3.2.2 Generating partial CHM rasters

The partial CHM_{XX} rasters were generated by triangulating only those first returns with a height (i.e. normalized z coordinate) exceeding the respective height thresholds and by rasterizing only those triangles where all three edge lengths fall within a particular cutoff point. The latter tries to assure that only triangles connecting first returns from the same tree crown are rasterized. Intuitively speaking, this rasterization threshold needs to be larger than the average point spacing, but smaller than the space that separates individual trees. We experimentally found 0.45 meter to be an optimal rasterization threshold for our study area and our LiDAR point density. Figure 2.2 illustrates the TIN generation of normalized raw LiDAR point clouds as well as the partial CHM_{XX} raster created at each stage. Moreover, it shows that the long triangles are removed from each partial CHM raster by the particular threshold.

The cell size of the raster is a key parameter when creating a CHM, especially for accurate derivation of individual tree attributes (Chen et al., 2006). Pouliot et al. (2002) have suggested a ratio of crown diameter to grid size appropriate for defining crown shape. Based on these results, we determined a grid size of 0.15 m in the CHM to be sufficient for recognizing a minimum crown diameter of 0.50 m from our field survey.

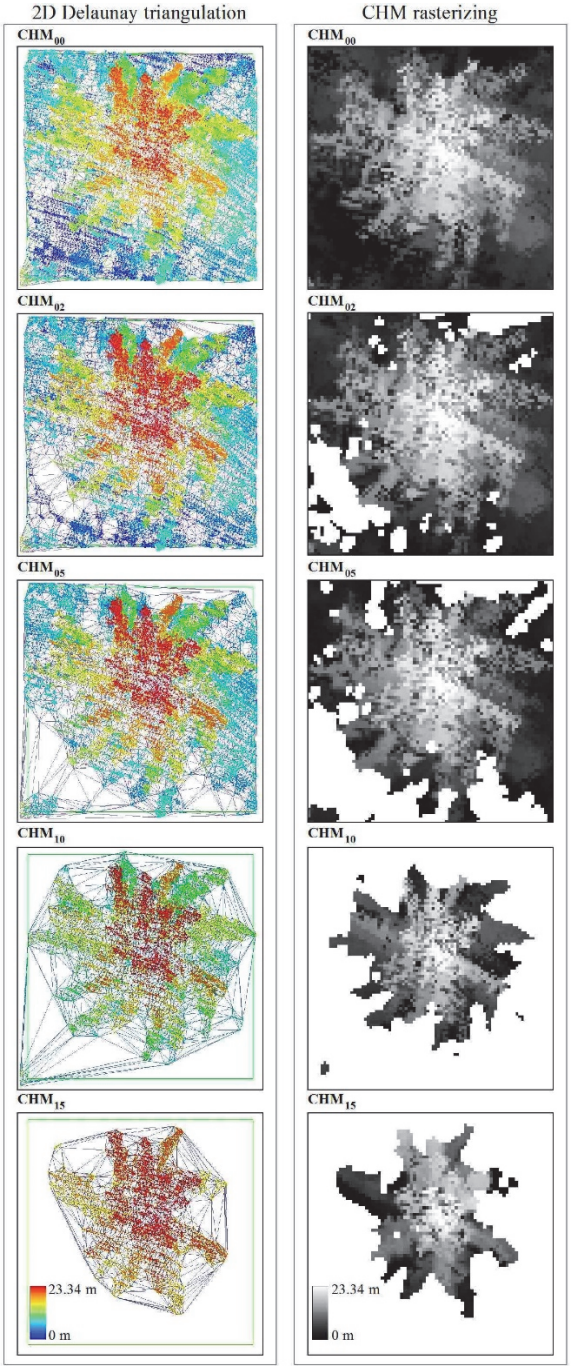

Figure 2.2: The generated TINs and rasters of partial CHMs for an individual tree.

2.3.2.3 Composing a pit-free CHM

In a final step, a pit-free CHM raster was created by combining the partial CHM_{XX} (CHM_{00} to CHM_{15}) rasters. This process can be envisaged by stacking the CHM_{XX} rasters on top of each other in order of height, with CHM_{00} at the bottom and CHM_{15} at the top. This simple cell-based calculation creates a final output raster (i.e. the pit-free CHM) with the output value at each location being the maximum value of all input rasters, CHM_{00} to CHM_{15}, without the need to involve any neighboring cells (Figure 2.3).

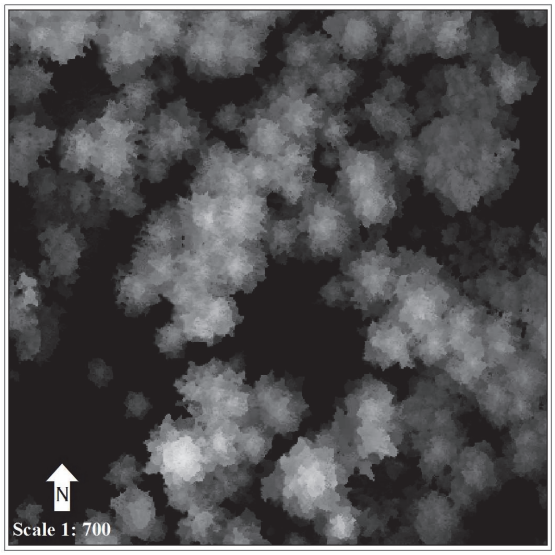

Figure 2.3: Subset of pit-free CHM.

2.3.3 Evaluation of the pit-free algorithm

In order to demonstrate the robustness of our algorithm for generating a pit-free CHM, a lower-density version of LiDAR data was created artificially from the original LiDAR survey. The pit-free CHMs derived from both LiDAR datasets were evaluated by visually comparing them with the standard CHMs after applying a Gaussian smoothing filter.

2.3.3.1 Thinning LiDAR data

The low-density version of LiDAR data was created using a simple point thinning algorithm, keeping only every nth (for example, the 15th) first return along the time line from the original dataset. By applying the keep-

every-nth-return filter to the first returns of each pulse, filtering takes place per-pulse rather than per-return. This step is important for two reasons: firstly, applying the filter to all returns of a high-return pulse positively affects the odds regarding the survival of its first return; and secondly, subsequent CHMXX production only utilizes the first return of each pulse. The algorithm was implemented in LAStools with a batch script that used every 15th first return from the entire point dataset and created a poor low-density dataset with mean point density of 7 points/m^2.

We should point out that keeping every nth first return does not properly simulate a survey undertaken at higher altitude with a slower scan rate. The diameter of the laser beam on the canopy increases with the altitude of the aircraft's flight path due to beam divergence of the laser (Lim et al., 2008). In an actual survey of lower density LiDAR, fewer laser pulses would sample the ground, each with a wider footprint and thus more likely to interact with the canopy higher-up (Hall et al., 2009). However, in our artificially created lower density survey, the beam width remains unchanged and the likelihood of the thin laser beams penetrating deeply into the canopy remains high. This creates the desired low-density data set of "especially poor quality".

The pit-free algorithm created a pit-free CHM with a pixel size of 0.50 m, derived from the low-density LiDAR data. Experimenting with this rasterizing process, we found 1.5 m to be an optimal rasterization threshold for such a low-density LiDAR dataset.

2.3.3.2 Smoothing CHM using Gaussian Filter

The degree of smoothness of a CHM is determined by the standard deviation (Gaussian scale) and the window kernel size (Dralle and Rudemo, 1996). In all our comparisons (on CHMs with 0.15 and 0.5 m pixel size, based on high and low density data, respectively), a Gaussian filter with a 5×5 kernel was used, as the next kernel size down of 3×3 had no noticeable effect regarding removing data pits from the standard CHMs.

2.3.4 Individual tree detection

For individual tree detection we used the variable window technique, developed by Popescu and Wynne (2004), which automatically detects

treetops. This approach uses a local maxima method with a circular variable window size to locate treetops with a well-defined crown in coniferous forests (Popescu, 2007). The variable window size of local maxima operates by assuming there is a relationship between tree height and crown size and uses these parameters to detect treetops (see Popescu and Wynne (2004) for more details).

2.3.4.1 Accuracy assessment of individual tree detection

Detection accuracy was assessed by comparing the automatically detected trees with the trees measured in the field. Errors of omission and commission were assessed by tree species and by stem diameter. For each tree species, the closest detected treetop within the reference crown boundary was considered to be a correctly detected tree. If more than one treetop is detected, the others are considered commission errors. Omission errors occur when no treetop is detected within the boundary. The overall accuracy of tree detection was computed by the accuracy index (*AI*) as defined by Pouliot et al. (2002):

$$AI\ (\%) = \left[\ (n - O + C)\right)/n] \times 100$$

where n is the number of reference trees in the study area, O is the omission error and C is the commission error. Based on the DBH distribution (Table 2.1) the range in DBH of the trees was divided into three classes: DBH less than 20 cm, DBH from 20 to 40 cm, and DBH greater than 40 cm. The proportion of correctly detected trees was calculated as a percentage of the total number trees in each class.

2.4 Results

2.4.1 Comparing the pit-free CHMs with smoothed CHMs

The efficacy of the pit-free algorithm was visually compared with the result from a 5×5 Gaussian filter. Figure 2.4 shows that the data pits – small dark squares – within the tree crowns, which are clearly visible in the standard CHM, are not present in the pit-free CHM.

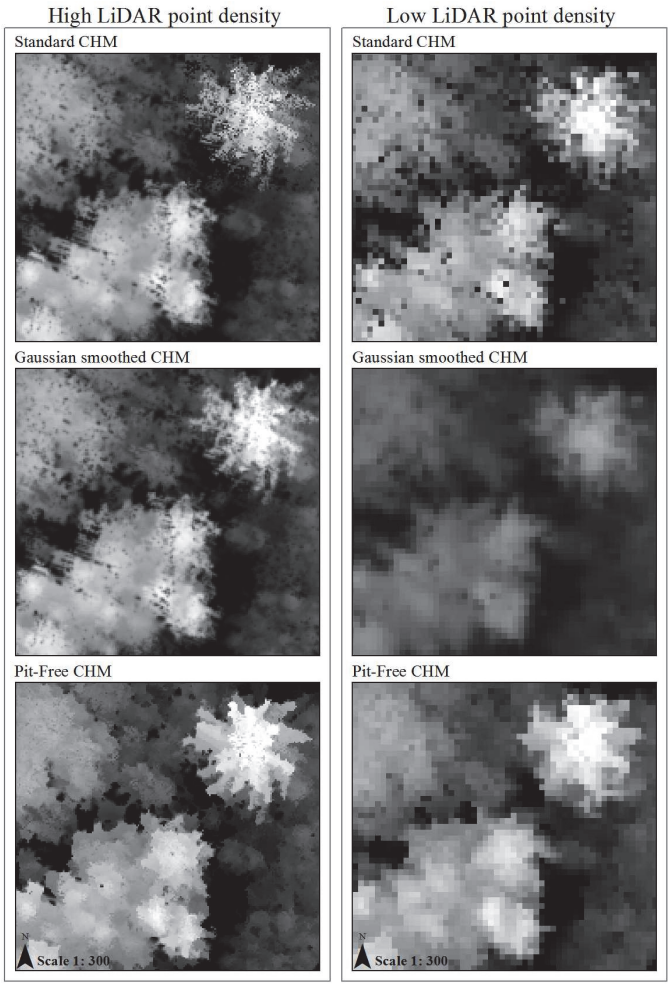

Figure 2.4: Visual representations of the pit-free algorithm compared to the standard CHM and Gaussian filter for both high-density and low-density LiDAR data.

The Gaussian filter also removed pits, but some pits remained compared to the pit-free CHM generated from the high-density dataset (Figure 2.4 (left)). The filter over-smoothed the CHM image derived from the low-density dataset, especially around the shoulders of tree crowns (Figure 2.4 (right)). The algorithm is seen in Figure 2.4 to operate robustly even with the poor quality, thinned LiDAR data. In our experiments, the algorithm effectively removed the pits as well as preserved the edges of canopy gaps and crowns for both the high and the low-density datasets (Figure 2.4, pit-free CHMs, left and right, respectively).

2.4.2 Assessing individual tree detection

The variable window technique was applied to both the smoothed and pit-free CHMs. Figure 2.5 shows examples of correctly detected trees, omission errors and commission errors for the pit-free CHM derived from high-density LiDAR data (white points and circles show the position of field trees and their crown size, respectively; gray stars indicate automatically detected treetops).

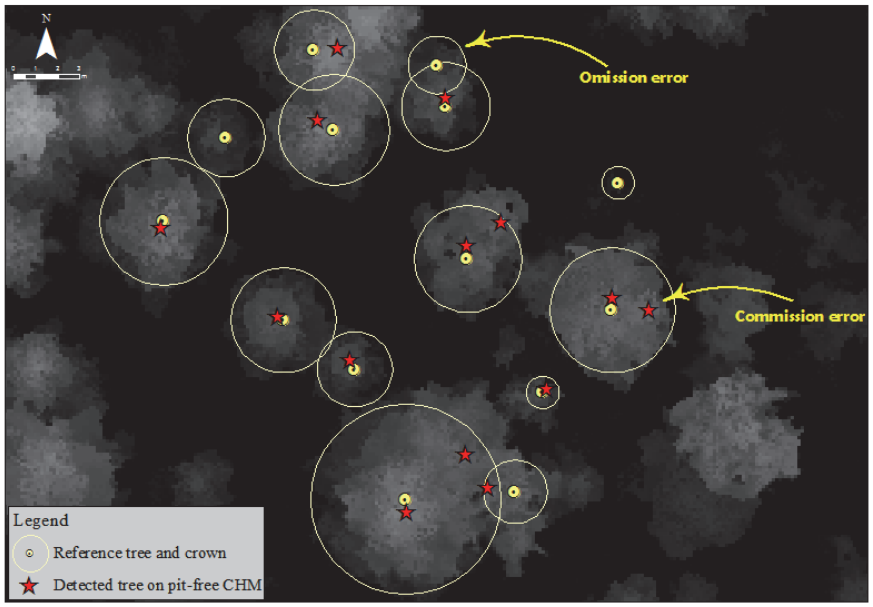

Figure 2.5: Example of detected trees, illustrating correctly identified crowns, omission errors, and commission errors of the pit-free CHM derived from high-density LiDAR data.

Table 2.3 presents the number and percentage of correctly detected trees, omission and commission errors, as well as the overall accuracy index based on high-density LiDAR data. As can be seen in the table, the total accuracy index for tree detection from the pit-free CHM (74.2%) is higher than from the smoothed CHM (70.6%). For the 33 measured deciduous trees (*Fraxinus excelsior, Populus tremula*), the detection accuracy was 51.5% for the pit-free CHM and 45.5% for the smoothed CHM. For coniferous trees, the overall detection rates were better. In addition, we tested whether there is a statistically significant difference between the

number of correctly detected trees using the CHMs derived from the Gaussian method and the pit-free method. The Chi-square test showed a statistically significant difference between the number of correctly detected trees in the smoothed CHM (511) and the pit-free CHM (544): $x^2 = 4.302$ and $p = 0.038$.

Table 2.3: Tree detection results for the smoothed CHM and the pit-free CHM. Both models have a pixel size of 0.15 m and were derived from high-density LiDAR data.

Field-measured trees		Gaussian Smoothed CHM				Pit-free CHM			
number of trees	Species	Correct n (%)	Omission n (%)	Commission n (%)	AI (%)	Correct n (%)	Omission n (%)	Commission n (%)	AI (%)
33	deciduous trees	19 (57.5)	14 (42.5)	4 (12.1)	45.5	21 (63.6)	12 (36.4)	4 (12.1)	51.5
29	Larix decidua	26 (89.6)	3 (10.4)	3 (10.4)	79.3	25 (86.2)	4 (13.8)	2 (6.8)	79.3
325	Pinus sylvestris	261(80.3)	64 (19.7)	13 (4.0)	76.3	273(84.0)	52 (16.0)	23 (7.0)	76.9
307	Pinus uncinata	205(66.8)	102 (33.2)	1 (0.3)	66.4	225(73.3)	82 (26.7)	0 (0.0)	73.3
694	Total	511(73.7)	183(26.3)	21 (3.0)	**70.6**	544(78.4)	150 (21.6)	29 (4.1)	**74.2**

The results of the tree detection assessment in evaluating the pit-free algorithm based on poor quality LiDAR data can be seen in Table 2.4. As expected, the decrease of the point density from 160 point/m^2 to 7 point/m^2 resulted in a very low accuracy (i.e. more commission error) when using Gaussian filters for both deciduous and coniferous trees. The pit-free CHM improved the total accuracy of the tree detection in comparison to the smoothed CHM, resulting in Accuracy Index values of 67.7% and 35.7%, respectively. Considering all 694 reference trees, 74.8% of the trees were detected correctly in the pit-free CHM and 69.8% in the smoothed CHM. The total commission error was 34% for the smoothed CHM, while it was only 6.9% for the pit-free CHM. The total omission error was 25.2% for the pit-free CHM and 30.2% for the smoothed CHM. In addition, the Chi-square test indicated a statistically significant difference between the pit-free CHM and the smoothed CHM, with the pit-free CHM resulting in a higher number of correctly detected trees ($x^2 = 4.403$, $p = 0.036$).

Table 2.4: Tree detection results for the smoothed CHM and the pit-free CHM. Both models have a pixel size of 0.50 m and were derived from low-density LiDAR data.

Field-measured trees		Gaussian Smoothed CHM				Pit-free CHM			
number of trees	Species	Correct n (%)	Omission n (%)	Commission n (%)	AI (%)	Correct n (%)	Omission n (%)	Commission n (%)	AI (%)
33	deciduous trees	17 (51.5)	16 (48.5)	10 (30.3)	21.2	20 (60.6)	13 (39.4)	8 (24.2)	33.3
29	Larix decidua	26 (89.7)	3 (10.3)	6 (23.0)	69	26 (89.7)	3 (10.3)	1 (3.4)	86.2
325	Pinus sylvestris	257(79.0)	68 (21.0)	139 (42.7)	36.3	268(82.5)	57 (17.5)	35 (10.7)	71.7
307	Pinus uncinata	184(60.0)	123 (40.0)	81 (26.3)	33.6	205(66.8)	102 (33.2)	4 (1.3)	65.5
694	Total	484(69.8)	210 (30.2)	236 (34.0)	**35.7**	519(74.8)	175 (25.2)	48 (6.9)	**67.7**

The range of DBH values in the study site (Table 2.5) allowed us to assess how the pit-free CHM compared to the smoothed CHM for both datasets. Trees with a DBH of more than 20 cm were successfully detected with both different types of CHM and data. However, a large portion of the missed trees had a DBH of less than 20 cm, with 71.3% and 62% of them correctly detected with a pit-free CHM using high- and low-density data, respectively. Only 60.4% and 50.3% of trees this size were detected with a smoothed CHM derived from high- and low-density data, respectively. The Chi-square test showed a significant difference between the pit-free CHM and the smoothed CHM regarding the number of correctly identified trees with DBH less than 20 cm (high-density: $p = 0.009$; low-density: $p = 0.008$). However, there was no significant difference between the types of CHM in detecting trees with a DBH of more than 20 cm (high-density: $p = 0.0714$; low-density: $p = 0.646$) or more than 40 cm (high-density: $p = 0.745$; low-density: $p = 1.000$).

Table 2.5: Proportion of correctly identified trees for the three stem diameter classes for each CHM and point density.

		All (n= 694)		
Portion of DBH range (cm)		< 20 (n = 258)	20-40 (n = 397)	> 40 (n = 39)
High-density LiDAR	smoothed CHM	156 (60.4 %)	322 (81.1 %)	33 (84.6 %)
	Pit-free CHM	184 (71.3 %)	326 (82.1 %)	34 (87.1 %)
Low-density LiDAR	smoothed CHM	130 (50.3 %)	322 (81.1 %)	32 (82 %)
	Pit-free CHM	160 (62 %)	327 (82.3 %)	32 (82 %)

2.5 Discussion

One of the challenges in creating a canopy height model through interpolation of first returns is that pits appear whenever a laser beam is able to penetrate a tree crown deeply before it generates the first return. Based on this observation we propose a new "pit-free" algorithm, which is able to remove pits efficiently and shows good potential for improving the detection of forest trees. Our algorithm is novel in that it removes the data pits directly from the LiDAR point clouds during the CHM creation. Other approaches, including automated methods (e.g. a smoothing filter) and semi-automated methods (i.e. a pit-filling algorithm) do not accurately target only the pits, but alter all pixels of the CHM raster (Ben-Arie et al., 2009; Shamsoddini et al., 2013). Moreover, automated and semi-automated methods do not consider the natural 3D structure of individual tree crowns when removing height variations. They consider the crown shape of forest trees as a circle (in nadir view on the raster CHM) (Zhao et al., 2013).

Our algorithm makes use of the knowledge that a tree crown tends to create LiDAR returns at a wide range of heights and generates a set of partial CHMs to remove the pits. There are two important thresholds in generating the partial CHMs: 1) the height thresholds, which define the set of partial CHMs; and 2) the rasterization threshold, which includes only those triangles with edge lengths below a particular value. There is a direct relationship between the number of partial CHMs (e.g. CHM_{02} to CHM_{15}) and the number of height thresholds (e.g. 2, 5, 10 and 15 m). When we decrease the spacing between height thresholds and consequently use a larger number of partial CHMs, shallower pits (i.e. with less variation in

height) are removed from the CHM across all vegetation levels. When we increase the rasterization threshold and consequently include larger triangles in the partial CHMs, larger pits (i.e. covering greater areas) are removed as well. Both thresholds, but especially the latter, change the appearance of the morphological structure of the tree crown. In this study, we experimentally selected height thresholds every 5 m for the partial CHMs of the taller trees (i.e. high vegetation class). The assignment of height thresholds was successfully applied here to CHMs with average tree heights of 13.5 m, but some variation in DBH, as shown in table 2.5; further research will establish performance of such thresholds on CHMs generated for different types of forest. We discovered that 0.45 m and 1.5 m are suitable rasterization thresholds for the high-density and low-density LiDAR data, respectively (i.e. the length of 3 pixels in each CHM). A larger threshold may increase the omission error in tree detection because it then becomes more likely for triangles from neighboring crowns to join together during rasterization. Although we evaluated the suitability of these thresholds for detecting individual trees, it would be useful to study their effect regarding the morphological structure of tree crowns further.

Our results show that the pit-free algorithm is visually superior to the Gaussian smoothing filter. Data pits are evident in the CHM_{00} raster (standard CHM) generated through standard Delaunay TIN rasterizing of all first returns. Nearby points with similar x and y coordinates but different heights tend to form small and steep triangles in the Delaunay TIN. When the x and y raster position of a CHM pixel falls within such a triangle, the linearly-interpolated height value of this cell may drastically differ from that of neighboring cells. The Gaussian filter generates new values for all cells based on the values of their nearest neighbors, thus affecting the original structure of the tree crown, especially when using low-density LiDAR data. By contrast, our pit-free algorithm removes pits from the CHM without altering the value of any other cells and thus preserves the original structure of tree crowns, for small trees as well, for both datasets. The pit-free algorithm offers the possibility to efficiently acquire detailed information on tree crown characteristics that play a critical role in a variety of applications (e.g., ecological, hydrological and

meteorological) sensitive to vegetation evolution at local and regional scale.

We also evaluated the algorithm by comparing the accuracy of tree detection using the pit-free CHM versus the smoothed CHM. The statistical analysis showed that there is a significant difference, with the pit-free CHM producing a higher number of correctly detected trees with high-density (p = 0.038) as well as low-density (p = 0. 036) LiDAR data. The result indicated the robustness of the pit-free algorithm at individual tree level in removing data pits for all crown sizes. The Gaussian method, however, reduces the effect of the pits based on a predefined window kernel size that cannot be optimal for all different crown types, especially at tree level (Shamsoddini et al., 2013). Compared to the Gaussian filter our algorithm is also significantly better at correctly detecting small trees (DBH of less than 20 cm) for both LiDAR datasets. Because the pit-free algorithm does not smooth the CHM, it does not remove true treetops of small trees as happens with the Gaussian filter (Hyyppä et al., 2000; Kaartinen et al., 2012; Säynäjoki et al., 2008; Solberg et al., 2006). Our algorithm was only evaluated for CHMs generated from first LiDAR returns as such CHMs are commonly used for tree detection. However, the study of Hyyppä et al. (2012) showed that creating CHMs from last LiDAR returns can also be used for locating individual trees. Last returns might show greater variation in height as the laser pulses will either penetrate all the way to the ground, or reach only the middle of the tree, or already get stuck in the crown. We believe that our pit-free algorithm benefits CHMs generated from both first and last return data.

The results indicate that the pit-free algorithm is especially successful for LiDAR data with many pits, such as our artificial example data where a small footprint laser beam samples the canopy with low density. Here the pit-free algorithm results in an accuracy index of 67.7%. This is particularly impressive compared to the Gaussian filtering, which produces a low accuracy index of 35.7%. Though many studies have underlined the importance of high density LiDAR data to improve tree detection, the result of this study suggests that laser point density has less impact on tree detection than the pit removal method. The study by

Shamsoddini et al. (2013) also revealed that the accuracy of tree attribute estimation, using low point density LiDAR data, will vary significantly depending on the particular pit removal algorithm chosen. The results of this study demonstrate with low point density LiDAR data, our pit-free algorithm will yield a higher accuracy regarding tree detection than Gaussian smoothing will.

2.6 Conclusions

In this study, we introduced a novel pit-free algorithm that can construct pit-free CHMs directly from LiDAR data. The impact of the pit-free algorithm on tree detection accuracy was investigated and compared with the Gaussian smoothing method. The results reveal that our algorithm can be adapted to work with different LiDAR point densities, and demonstrates a statistically significant improvement in the accuracy of tree detection. It will be interesting to investigate whether our pit-free CHMs also improves height estimation, crown segmentation and subsequent biophysical parameters such as biomass.

Chapter 3

Effect of slope on treetop detection using a LiDAR canopy height model*

* This chapter is based on:
Khosravipour, A., Skidmore, A.K., Wang, T., Isenburg, M., Khoshelham, K., 2015. Effect of slope on treetop detection using a LiDAR Canopy Height Model. *ISPRS Journal of Photogrammetry and Remote Sensing*, 104, 44-52.

Abstract

Canopy Height Models (CHMs) or normalized Digital Surface Models (nDSM) derived from LiDAR data have been applied to extract relevant forest inventory information. However, generating a CHM by height normalizing the raw LiDAR points is challenging if trees are located on complex terrain. On steep slopes, the raw elevation values located on either the downhill or the uphill part of a tree crown are height-normalized with parts of the digital terrain model that may be much lower or higher than the tree stem base, respectively. In treetop detection, a highest crown return located in the downhill part may prove to be a "false" local maximum that is distant from the true treetop. Based on this observation, we theoretically and experimentally quantify the effect of slope on the accuracy of treetop detection. The theoretical model presented a systematic horizontal displacement of treetops that causes tree height to be systematically displaced as a function of terrain slope and tree crown radius. Interestingly, our experimental results showed that the effect of CHM distortion on treetop displacement depends not only on the steepness of the slope but more importantly on the crown shape, which is species-dependent. The influence of the systematic error was significant for Scots pine, which has an irregular crown pattern and weak apical dominance, but not for mountain pine, which has a narrow conical crown with a distinct apex. Based on our findings, we suggest that in order to minimize the negative effect of steep slopes on the CHM, especially in heterogeneous forest with multiple species or species which change their morphological characteristics as they mature, it is best to use raw elevation values (i.e., use the un-normalized DSM) and compute the height after treetop detection.

3.1 Introduction

Information on individual trees is critical for a variety of forest activities and for environmental modeling at the local and regional scales (Lichstein et al., 2010). In the last decade, airborne Light Detection and Ranging (LiDAR) has become a reliable remote sensing technique for estimating individual tree parameters, due to its capability to generate detailed and very precise three-dimensional tree information (Hyyppä et al., 2008; Lim et al., 2003b).

As an initial and important step in any analysis of LiDAR data on individual trees, treetop detection has attracted much attention and research (Hosoi et al., 2012; Hyyppä et al., 2012; Jing et al., 2012a; Kaartinen et al., 2012; Popescu and Wynne, 2004; Vastaranta et al., 2011). Identifying the correct treetop can provide accurate information on crown characteristics and the tree height information, which in turn are useful inputs for growth and volume estimation models (Gebreslasie et al., 2011; Vastaranta et al., 2011; Wulder et al., 2000). A widespread approach is to identify local maxima, which generally correspond to the location and height of individual trees, and then to construct crown segments (Falkowski et al., 2006; Næsset and Økland, 2002; Solberg et al., 2006; Véga and Durrieu, 2011).

The local maxima are typically obtained from the height variation of a LiDAR-derived Canopy Height Model (CHM), also known as a normalized Digital Surface Model (nDSM) (Forzieri et al., 2009; Li et al., 2012; Persson et al., 2002; Yu et al., 2011). There are two ways to create a CHM: with rasters or with point clouds (Li et al., 2012; Persson et al., 2002). When working with rasters, the LiDAR ground returns are used to create a raster DTM (Digital Terrain Model), and the highest or first LiDAR returns are used to create a raster DSM (Digital Surface Model). Then the raster DTM is subtracted from the raster DSM to create the final raster CHM (Lim et al., 2003b). When working with point clouds, the classified LiDAR is height-normalized by replacing the raw elevation of each return (i.e. its z coordinate) with its height above the DTM (Khosravipour et al., 2014; Van Leeuwen et al., 2010). Either way, the end result is the absolute canopy height above the bare-earth terrain surface.

Although the procedure of computing local maxima from a CHM is conceptually simple, the accuracy of its result largely depends on the quality of the acquired LiDAR data, its processing and/or post-processing, and the forest conditions (Kaartinen et al., 2012). For example, the use of a higher density of laser pulse footprints improves the chance of the laser hitting the treetops (Hyyppä et al., 2008; Lefsky et al., 2002), and the use of an efficient local maxima technique enhances treetop identification by reducing commission and omission errors (Chen et al., 2006; Kaartinen et al., 2012; Vauhkonen et al., 2012a). A new study suggests that the accuracy of treetop detection can be improved further by removing height irregularities in the CHM (Khosravipour et al., 2014). Moreover, a number of studies indicate that the various forest conditions (e.g., crown sizes, ages, site types, tree species and forest density) can significantly influence intermediate LiDAR derivatives and thereby the performance of tree detection algorithms (Falkowski et al., 2008; Pitkänen et al., 2004; Popescu and Wynne, 2004; Vauhkonen et al., 2012a; Yu et al., 2011).

Complex forest terrain presents a challenging problem, as it affects the performance of the height normalization step by distorting the CHM, which can reduce the accuracy of extracted tree biophysical parameters (Vega et al., 2014). On steep slopes, the raw elevation values located, for example, on either the downhill or the uphill part of a tree crown are height-normalized with parts of the DTM that may be much lower or higher than the tree stem base, respectively (Breidenbach et al., 2008). Therefore, in the CHM, the downhill part of the crown will “rise” while the uphill part will “sink”, causing the entire tree crown to be systematically distorted. In treetop detection, the “rising” branch overhanging lower terrain in the downhill part can turn into a “false” local maximum that is distant from the true treetop. This problem was posed in Isenburg’s keynote speech at Silvilaser 2012 (Isenburg, 2012). He found a CHM that overestimated true tree height by more than double: eucalyptus trees on steep and eroded slopes in the Canary Island of Tenerife were estimated as being 51 meters tall whereas their true height was 25 meters. Takahashi et al. (2005) and Véga and Durrieu (2011) also reported that one of the sources of tree height overestimation from LiDAR-derived

CHM is a horizontal offset error between field and LiDAR treetop detection, particularly on steeper slopes. They concluded the difference may be due to the LiDAR-derived treetop simply being identified as the maximum value of CHM within the crown area on steeper slopes. Heurich et al. (2003) pointed out that this error increases for leaning trees and/or steeper terrain slopes. Breidenbach et al. (2008) reported an increasing underestimation of the CHM-derived height with steeper upward slopes and vice versa for downward slope, which can cause tree height – one of the most important stand characteristics determined in forest inventory – to be misinterpreted, thereby affecting estimates of subsequent biophysical parameters such as biomass, volume and carbon sequestration. The recent study of Vega et al. (2014) suggested using un-normalized elevation values (i.e. using the DSM), and computing the height after a tree crown segmentation step, to avoid the undesirable effect of steep slopes on the CHM. However, until now, the influence of the normalization process on treetop detection and height estimation has neither been studied nor quantified.

The aim of this study was to quantify the effects of slope gradient on the accuracy of treetop detection when using a LiDAR-derived CHM. We first present a simplified theoretical model to illustrate how normalization causes a systematic error in CHM-based treetop detection when an individual tree is located on a slope. We then assess the accuracy of treetop detection by using both the CHM (i.e. the normalized elevations) and the DSM (i.e. un-normalized elevations). Next, we compute the positional difference between the same tree detected in both the CHM and the DSM, in order to investigate the influence of the slope on the horizontal displacement of CHM-detected trees and its effect on subsequent height estimation.

3.2 Theoretical model

The systematic error in CHM-based treetop identification can be quantified by using a conceptual model that is based on field measurement of tree heights. In the field, the original tree height is determined as a vertical distance from tree apex to the upslope root crown (Husch et al.,

1982). According to the model (illustrated graphically in Figure 3.1), the height of a tree is calculated as the magnitude (length) of a vector h originating at the base of the tree and ending at the treetop. Without loss of generality, we can assume that the tree height is formulated as:

$$h = b + 2r \tag{3.1}$$

where b is the crown base height and r is the radius of the hypothetical tree crown.

When computing the tree height from the height-normalized model (i.e., CHM) the distance from the highest crown return to its projection on the DTM is used, which introduces a systematic error when the terrain is sloping (Takahashi et al., 2005; Véga and Durrieu, 2011; Vega et al., 2014). We assume a tree on a terrain of constant slope with an idealized spherical crown is always hit at the highest point across the canopy by the laser pulses (i.e. no canopy penetration). Although a tree crown is never have perfectly spherical in nature, tree crowns (e.g., coniferous or deciduous) are typically considered to be circular in nadir view (Biging and Gill, 1997; Doruska and Burkhart, 1994). Then we can use the following simplified theoretical model and estimate the CHM-derived tree height as the local maximum of the function $h_{CHM}(x)$ within $-r \leq x \leq r$:

$$h_{CHM}(x) = b + c(x) + s(x) \tag{3.2}$$

where b is the constant crown base height, and $c(x)$ and $s(x)$ are the contribution of the tree crown and slope in the estimation of CHM-derived tree height, respectively.

The crown contribution $c(x)$ includes a constant r as the crown radius, and a vertical distance that is a function of the horizontal displacement x from the original treetop (see Figure 3.1). This perpendicular distance can be calculated with the Pythagoras theorem that relates the lengths of the three sides of any right triangle as:

$$c(x) = r + \sqrt{r^2 - x^2} \tag{3.3}$$

The slope contribution $s(x)$ describes a vertical distance that is also a function of the horizontal displacement x from the original treetop. It is based on the terrain slope that is assumed to be constant below the tree:

$$s(x) = -mx \tag{3.4}$$

where m is the constant terrain slope.

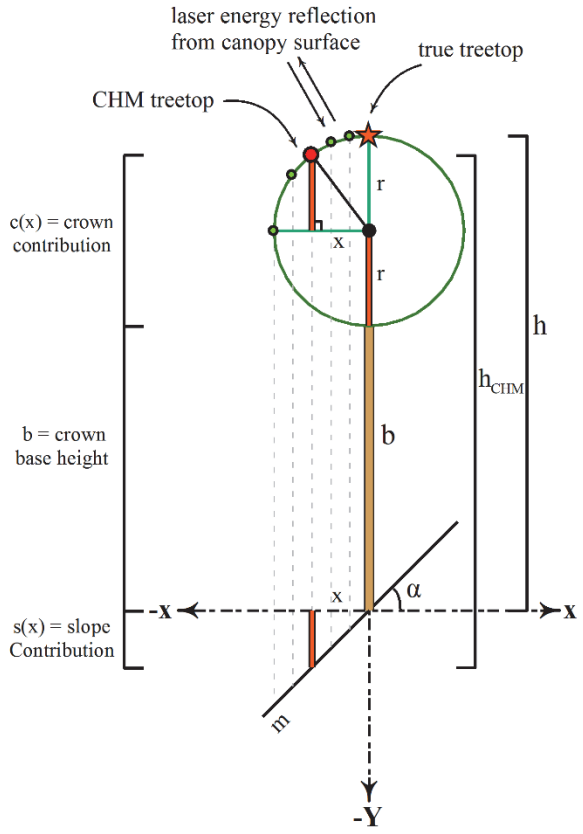

Figure 3.1: Schematic diagram of the geometry involved in the treetop detection based on the effect of slope gradient on a LiDAR-derived CHM.

The resulting function $h_{CHM}(x)$ expresses the tree height that we expect to measure for our idealized circular crown along a line that goes through the true treetop in the direction of the steepest slope for a given radius r and a constant slope m. The x_{max} is the x that locally maximizes the function $h_{CHM}(x)$ within the crown diameter (i.e. $-r \leq x \leq r$). The x_{max} estimates the expected systematic horizontal displacement from the true treetop ($x = 0$). The value $h_{CHM}(x_{max})$ estimates the expected CHM-derived tree height.

The two extrema x_{ext} – one *local maximum* and one *local minimum* – of the function $h_{CHM}(x)$ can be determined by finding the zero crossings of its

derivative function $h_{CHM}'(x)$ so that the x_{max} can be found by solving $h'_{CHM}(x) = 0$:

$$h_{CHM}(x) = b + r + \sqrt{r^2 - x^2} - mx \tag{3.5}$$

$$h'_{CHM}(x) = -x/\sqrt{r^2 - x^2} - m$$

$$h'_{CHM}(x_{ext}) = -x/\sqrt{r^2 - x^2} - m = 0$$

$$x_{ext} = \pm mr/\sqrt{m^2 + 1}$$

The horizontal displacement is always directed downhill. Represented in our schematic diagram (Figure 3.1), the horizontal displacement will be negative for positive slope ($m > 0$) but positive for negative slopes ($m < 0$).

$$horizontal\ displacement = x_{max}$$

$$x_{max} = -mr/\sqrt{m^2 + 1} \tag{3.6}$$

By substituting the x value in the CHM-derived tree height function (equation 3.2) with the result obtained for x_{max}, we can estimate the expected CHM-derived tree heights. The expected error difference (vertical displacement) can be calculated by subtracting the true tree height (equation 3.1) from the expected CHM-derived one (equation 3.2):

$$vertical\ displacement = h_{CHM}(x_{max}) - h$$

$$vertical\ displacement = r(\sqrt{m^2 + 1} - 1) \tag{3.7}$$

Though the theoretical model over-simplifies crowns in the real world, it is adequate to demonstrate the systematic error introduced by sloping terrain during the normalization step: the height of LiDAR canopy returns is overestimated downhill of the tree stem and it is underestimated uphill of the tree stem. This systematic error is one of the sources of error that usually leads to tree height being misinterpreted due to steep slope (Breidenbach et al., 2008; Takahashi et al., 2005; Véga and Durrieu, 2011).

The formulas in equation (3.6) and (3.7) suggest that for a constant slope (m) both the expected horizontal and vertical displacement increase linearly when the crown radius (r) increases (an elliptical crown behaves similarly). However, for a constant radius (r), when slope increases, slope

effect on horizontal displacement increases asymptotically whereas slope effect on vertical displacement increases exponentially. As an example, we simulate the theoretical model for different slopes for a constant radius (r) of 3.5m (Figure 3.2). The asymptotic effect on horizontal displacement is clearly visible when the slope approaches 40 degrees. The effect of slope on vertical displacement increases exponentially, especially when the slope reaches 45 degrees, and goes to infinity as the slope approaches 90 degrees.

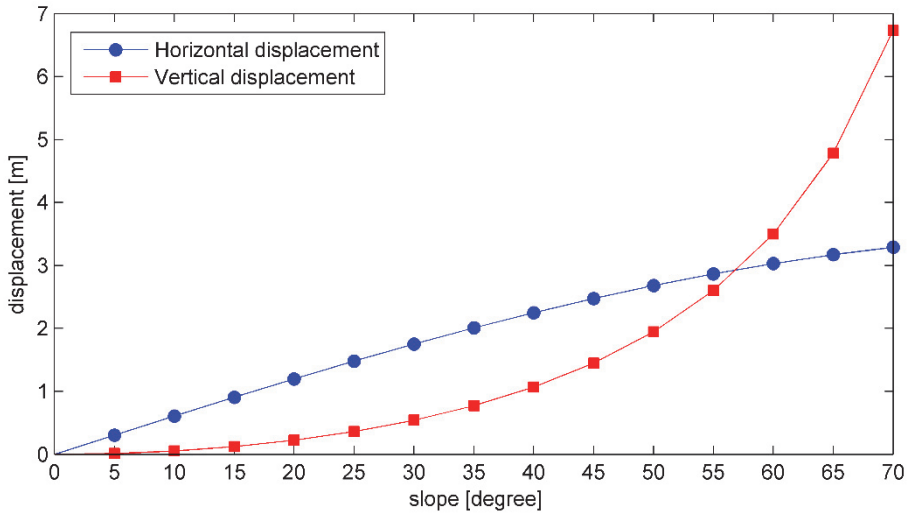

Figure 3.2: The relationship between slope, horizontal displacement, and vertical displacement for an idealized spherical crown with a radius of 3.5 meters.

3.3 Experimental data

3.3.1 Study area

Bois Noir (44° 23′ N, 6° 45′ E) is a forest in the Barcelonnette basin in the southern French Alps (Figure 3.3). The northern part of Bois Noir is characterized by irregular rugged topography with slope gradients ranging from 10° to 35° (Thiery et al., 2007) and the southern part is characterized by extensive steep scree slopes of up to 70° (Razak et al., 2011b). The test area was 1.30 km^2, with a cover predominantly of mountain Pine (*Pinus uncinata*) and Scots pine (*Pinus sylvestris*), at an elevation ranging from 1400 to 2380 m above sea level (Razak et al., 2013).

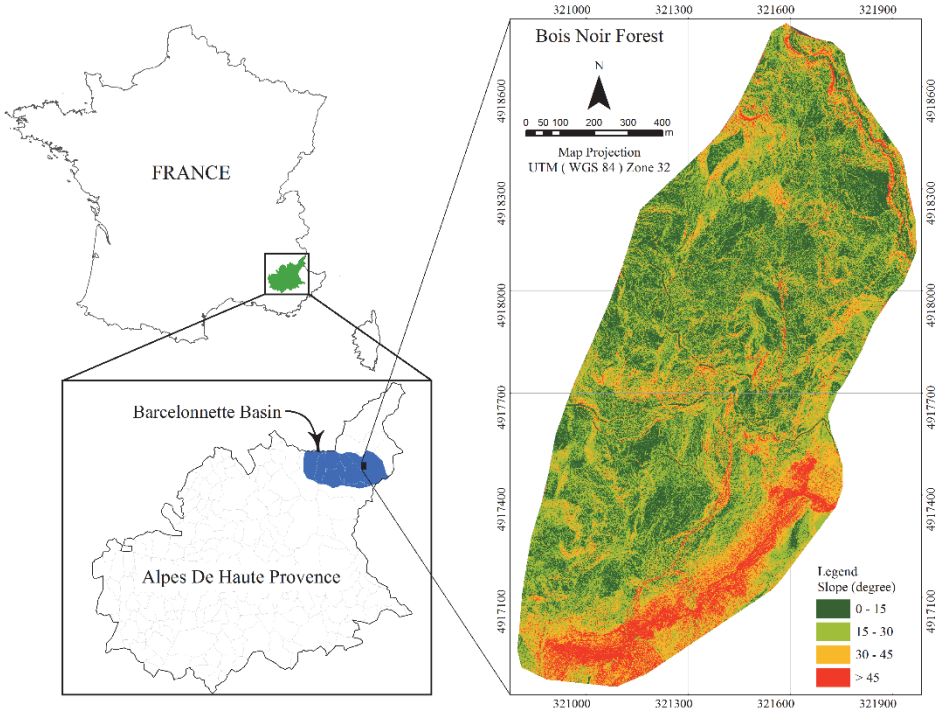

Figure 3.3: Location of the Barcelonnette basin in the map of France (left) and the slope map of the Bois Noir Forest (right).

3.3.2 Field data

Field inventory data were collected during September 2011 and 2012. Some parts of the forest had been affected by a landslide that had caused the tree stems to bend and tilt. We used the landslide boundaries provided by Thiery et al. (2007) and Razak et al. (2011a) to establish 46 plots outside the landslide area. For this research, the measurements collected included tree location, tree crown diameter (in two perpendicular directions) and tree species determination (Table 3.1). The position of individual trees and the central point of each plot were recorded using the Leica 1200 Differential GPS System and a total station (see Khosravipour et al. (2014) for more detail). The total number of trees sampled was 514.

Table 3.1: Descriptive statistics of the tree crown diameter measurements (m).

	All (n= 514)	Scots pine (n=263)	mountain pine (n=251)
Minimum	0.50	0.90	0.50
Maximum	9.10	9.10	6.70
Median	2.50	3.45	1.70
Mean	2.82	3.66	1.94
Std Dev	1.47	1.40	0.92

3.3.3 LiDAR data and pre-processing

The LiDAR data were acquired using a helicopter in July 2009. The small footprint full-waveform LiDAR system (RIEGL VQ-480i) utilized by Helimap has been developed specifically for mapping mountainous forested area (Vallet and Skaloud, 2004). The system was operated at a laser pulse repetition rate of 300-kHz and a scan width of 60° and performed on-line full-waveform analysis to extract up to five discrete returns for each pulse. The survey was flown 250 m above ground level, resulting in a mean footprint diameter of 75 mm on the ground. In order to increase the laser pulse density, the area was covered by seven overlapping flight lines. The mean point density of all return was 160 points/m^2.

The LiDAR data were stored separately in adjacent, non-overlapping tiles. The LiDAR points were retiled to a tile size of 300 m with a 15 m buffer along all sides of each tile, in order to avoid edge artifacts at the tile boundaries during tile-based processing (Isenburg et al., 2006b). The LiDAR points were classified into ground and non-ground returns, using automatic progressive TIN (triangular irregular network) densification filtering as developed by Axelsson (2000). Once classified, the ground returns point clouds were interpolated with a TIN by Delaunay triangulating (Isenburg et al., 2006a), which was then rasterized onto a grid with 0.15 m^2 spatial resolution, to create the DTM. This LiDAR-derived DTM of the Bois Noir forest was quantitatively and qualitatively assessed, using procedures described by Razak et al. (2011b). The vertical accuracy of the DTM varied between 0.28 and 0.36 m compared to the field data, depending on whether the terrain was open or forested. From this DTM a slope gradient raster was computed with ESRI's ArcGIS software, which implements the third-order finite difference method (Horn, 1981). The

slope at each tree stem location used in our analysis was calculated as the mean terrain slope within the reference tree crown.

The first returns were used for generating the DSM and the CHM. Such LiDAR-derived surface models often contain so-called "data pits" which occur, for example, when a laser pulse penetrates deep into the canopy before producing its first return, or when multiple flight lines that scan the canopy from different viewpoints are merged (Axelsson, 1999; Ben-Arie et al., 2009; Leckie et al., 2003). The pit-free algorithm, developed by Khosravipour et al. (2014), was used for generating the pit-free CHM. This algorithm consists of two stages: the first stage normalizes the height of the LiDAR returns and generates a standard CHM raster from all first returns and several partial CHM rasters from only those first returns that are above a set of increasing height thresholds (e.g., above 2 m, 5 m, 10 m and 15 m). The second stage composes the standard and all partial CHM rasters into one final CHM by keeping for each pixel the highest value across all CHMs. A variation of the pit-free algorithm was used to generate the pit-free DSM simply by omitting the normalization step and operating on the original elevations. The CHM and DSM were rasterized to the same 0.15 m^2 grid spacing as that of the DTM. The pre-processing was implemented by batch-scripting several modules of the LAStools software (rapidlasso GmbH, 2014).

3.3.4 Individual treetop detection

In order to extract individual treetops, a method based on morphological opening and reconstruction was applied to both the CHM and the DSM. The mathematical morphological opening operation (erosion followed by dilation) with an appropriate structuring element (which defines a neighborhood around a given point) is an image-processing technique that can separate different objects (Serra, 1982; Vincent, 1993) and preserve the structural information of each object, based on the structuring element's shape (Wang et al., 2004). The shape and size of the structuring element are commonly based on the shape and size of the objects of interest. In this study, a flat disk with a diameter of 1.05 m (7 pixel sizes) was experimentally found appropriate (based on the field crown size data) to identify the treetops. The opening operations removed "*foreground*"

objects (i.e., treetops) that were smaller than the selected structuring element in the image. The result is an *opened image*. Afterwards, morphological reconstruction, which is a very efficient method for extracting regional maxima (Khoshelham et al., 2010; Vincent, 1993), was implemented. The opened image was selected as a *marker* under the original canopy surface as a *mask* image, in order to retrieve the shape of tree crown boundaries that were smoothed by the opening operation. Subsequently, the reconstructed image was subtracted from the original canopy surface in order to isolate the individual treetops that had been removed by the opening operation as regional maxima. The local maxima of each regional component were extracted from the image. They are the estimated treetop points (x, y, and z). For the CHM, the z coordinate of each treetop point corresponds to the estimated tree height. For the DSM, the z coordinate of each treetop point was height-normalized using its projection onto the DTM.

3.3.4.1 Accuracy assessment of individual treetop detection

The performance of the treetop detection was evaluated by comparing the automatically detected trees from both the CHM and DSM with the trees measured in the field. If one treetop had been detected within a reference crown boundary, the detection was considered correct. If more than one treetop was detected, the closest reference tree was considered as correct, and other trees were then defined as commission errors. However, if no LiDAR-detected treetop was found, this error was considered as an omission error. Subsequently, the distance between the trees detected from the CHM and those detected from the DSM was measured, in order to calculate the horizontal displacement of detected trees in the CHM. The linear regression model was used to find the relationship between the horizontal displacement and the slope of the terrain. Due to the lack of accurate tree height measurements in the field for our super-high density LiDAR points, it was not feasible to validate the tree heights derived from the CHM and the DSM. Thus, only the differences between the height measurements in the CHM and the DSM were used to find the relationship between the vertical displacement and the slope of the terrain. In addition,

a visual 3D comparison between the CHM and the DSM provided further insight into the results.

3.4 Experimental results

In order to create a CHM for detecting individual treetop position, the normalization process was applied to the elevation of the LiDAR points. Figure 3.4 shows the distorting influence of slope on this LiDAR height normalization on the original morphological structure of the crown of a Scots pine and the crown of a mountain pine. As can be seen, the Scots pine tree, which has a wider, more irregular crown pattern and weaker apical dominance, is affected more than the mountain pine tree, which has a smaller and narrower crown.

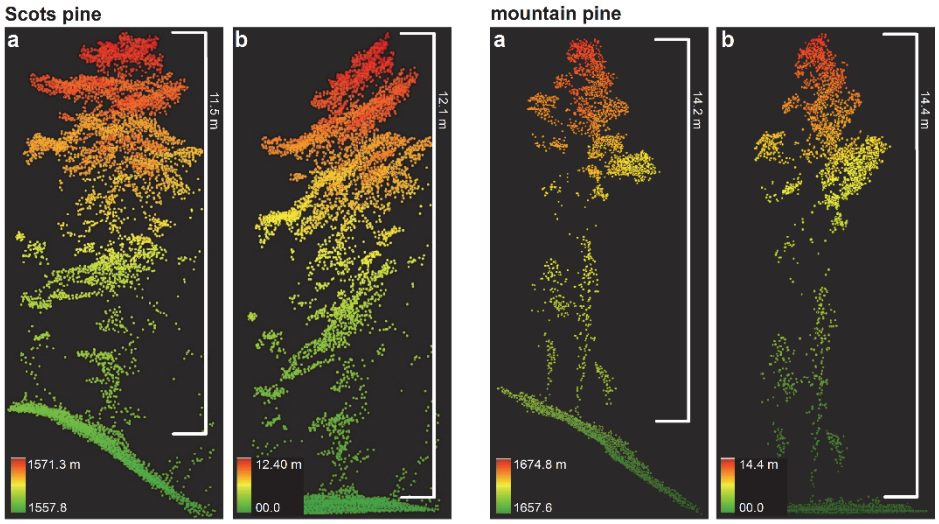

Figure 3.4: The effect of slope on the LiDAR data before normalization (a) and after normalization (b) for Scots pine and mountain pine on a slope gradient of approx. 35 degrees.

In order to quantify the effect of the slope, the treetop detection technique was applied to both the CHM and DSM. Figure 3.5 shows the CHM raster, examples of trees detected in both the CHM and the DSM, and also omission and commission errors. The Figure 3.5 also illustrates an example of the horizontal displacement of a CHM-detected treetop position compared to its location as detected in the corresponding DSM.

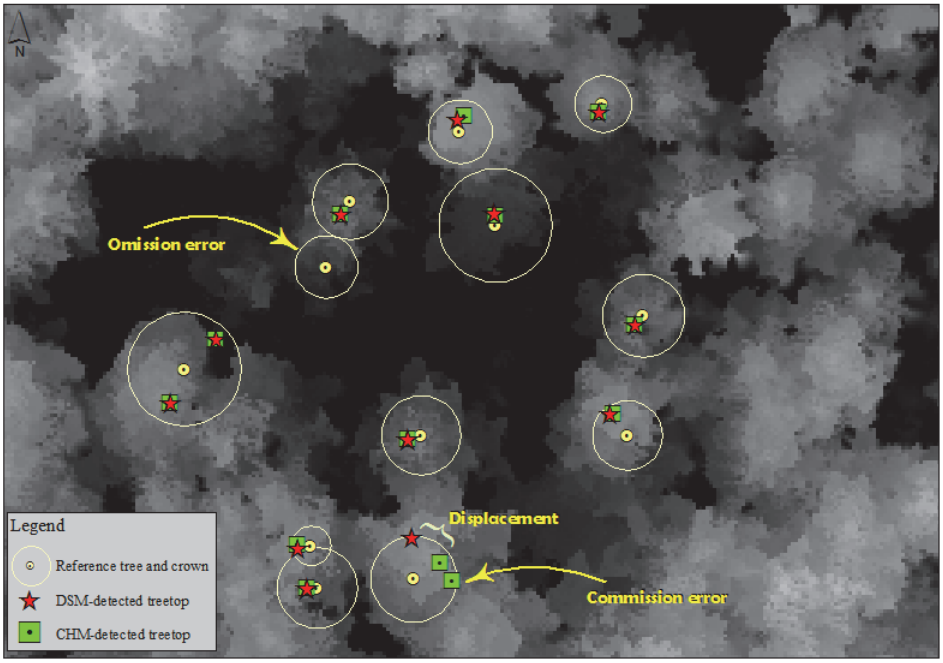

Figure 3.5: An example of identified treetops, omission and commission errors, and the horizontal displacement between a CHM-detected and a DSM-detected treetop position.

Table 3.2 presents the numbers and the percentages of correctly detected trees, omission and commission errors, assessed for Scots pine and mountain pine. The overall tree detection rate of both species was high ("Correct" Table 3.2). Note that the number of false trees results ("Commission") was higher for Scots pine than for mountain pine.

Table 3.2: tree detection results for the CHM and the DSM.

Field-measured trees		CHM			DSM		
number of trees	Species	Correct n (%)	Omission n (%)	Commission n (%)	Correct n (%)	Omission n (%)	Commission n (%)
263	Scots pine	215(81.7)	48 (18.2)	30 (11.4)	223(84.8)	40 (15.1)	25 (9.5)
251	mountain pine	207(82.4)	44 (17.5)	1 (0.3)	206(82.0)	45 (17.9)	0 (0.0)
514	Total	422(82.1)	92(17.8)	31(6.0)	429(83.4)	85 (16.5)	25 (4.8)

Out of a total 514 trees, 395 trees were detected in both the CHM and the DSM. The range of positional differences between the same CHM-

detected and DSM-detected trees was between 0.15 m (one pixel) and 1.80 m. Because remotely sensed data of high spatial resolution is often spatially auto-correlated (Chen et al., 2012; Hu et al., 2014), we used the range of semi-variogram statistics in order to adjust the minimum distance of the horizontal displacement of treetops. The semi-variograms (using the spherical model) of the both CHM and the DSM images indicated that pixels are highly correlated within a range of 0.35 m. Therefore, treetops detected in both the CHM and DSM within 0.35 m of each other were assumed to belong to the same tree (i.e. to have a positional difference of 0.0 m).

The numbers and percentages of the same treetops that were correctly detected from both the CHM and the DSM are reported in Table 3.3 per tree species and for three different slope ranges (i.e. 0 – 15, 15 – 30, and 30 – 45 degrees). On a terrain slope of less than 15 degrees there was no significant horizontal displacement of treetops between the CHM and the DSM, but the number of affected trees increased with steepness of the terrain. The maximum displacement of CHM-detected treetops from DSM-detected treetops was 1.80 m and occurred on slopes of more than 30 degrees. As expected, the horizontal positional error caused an increasing vertical displacement error (i.e., an overestimation of CHM-derived tree height). The maximum height overestimation was 1.78 m for slope of more than 30 degrees. However, the effect of the systematic error became evident only for Scots pine trees, not for mountain pine trees. A remarkable 46.6 percent of correctly detected Scots pine trees located on steep terrain (more than 30 degrees) were affected by the systematic error, whereas the conical mountain pines were not affected by this error.

Table 3.3: Percentages and numbers of correctly detected trees located on three different slopes.

Field-measured trees			Linked CHM- and DSM- detected trees								
number of trees	slope class	species	Total *n*	without displacement n (%)	with displacement						
					n (%)	Horizontal displacement (m)			Vertical displacement (m)		
						min	max	mean	min	max	mean
64	0-15	Scots pine	44	43 (97.7)	1 (2.2)	0.42	0.42		0.10	0.10	
179	15-30		142	126 (88.7)	16 (11.2)	0.42	1.71	0.74	0.03	0.75	0.16
20	30-45		15	8 (53.3)	7 (46.6)	0.80	1.80	1.39	0.01	1.78	0.97
263		Total	201	177 (88.0)	24 (11.9)	0.42	1.80	0.92	0.01	1.78	0.40
81	0-15	Mountain pine	64	64 (100)	0(0.0)						
148	15-30		114	111(97.3)	3 (2.6)	0.45	1.27	0.73	0.07	0.14	0.10
22	30-45		16	16 (100)	0(0.0)						
251		Total	194	191(98.4)	3 (1.5)	0.45	1.27	0.73	0.07	0.14	0.10

A linear regression model using slope as the independent variable explained 54% of the variance associated with the positional displacement of CHM-detected Scots pine trees (Figure 3.6). The result of its ANOVA demonstrated that the regression model is significant when predicting the horizontal displacement of CHM-detected trees ($F = (1,23) = 23.73$, $p < 0.05$). The field-measured crown radius of Scots pine species was also plotted against the horizontal displacement. Surprisingly, however, there was no correlation between the magnitude of the systematic error and the crown size within Scots pine trees (Figure 3.7).

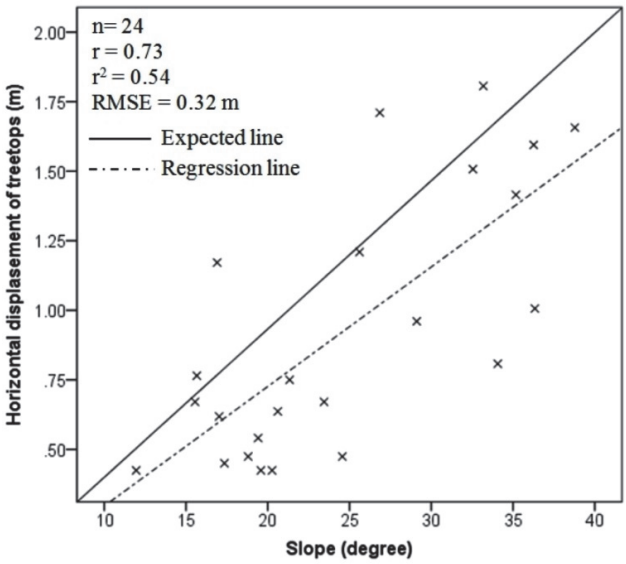

Figure 3.6: Horizontal displacement of the Scots pine treetops regressed against slope.

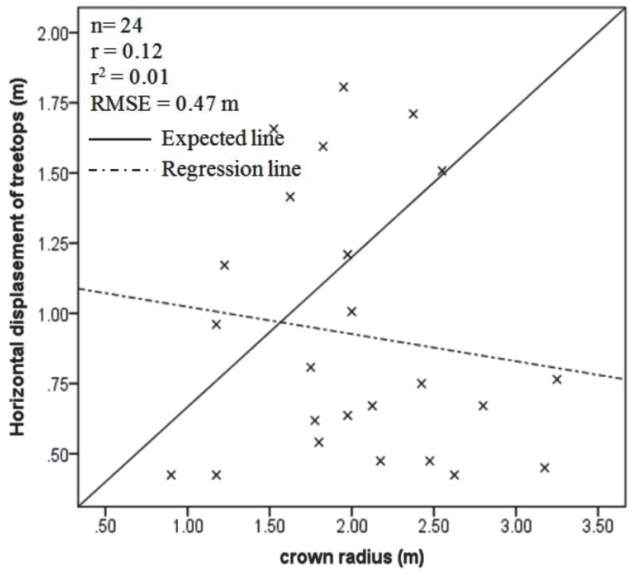

Figure 3.7: Horizontal displacement of the Scots pine treetops regressed against crown radius.

The height differences between the CHM-derived tree height and DSM-derived tree height were plotted against slope gradient. On average, the CHM-derived height was 0.40 m above the DSM-derived height, as was expected from our theoretical model. The absolute minimum difference

was 0.01 m and absolute maximum was 1.78 m. The regression model using slope terrain explained 48% of the variance associated with the vertical displacement rate (Figure 3.8). Its ANOVA result demonstrated the regression model is a significant model when predicting the height differences by slope ($F = (1, 23) = 20.44$, $p < 0.05$).

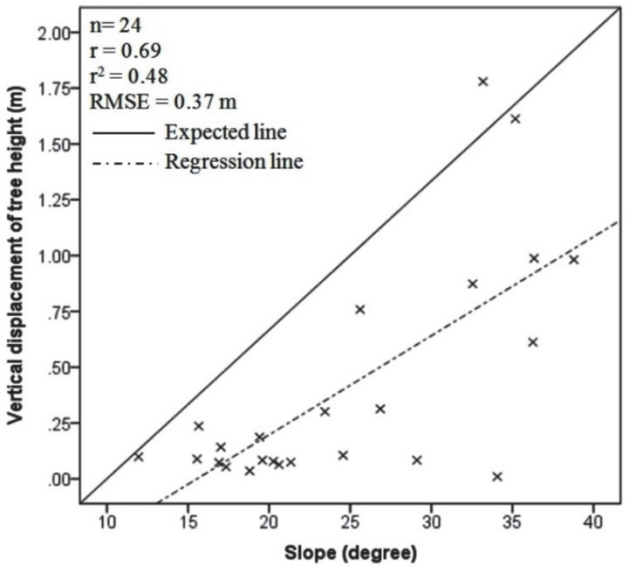

Figure 3.8: Vertical displacement of the Scots pine trees' height regressed against slope.

3.5 Discussion

One of the challenges when generating a CHM through height normalization is that a systematic error appears whenever trees are located on complex, sloping terrain. Based on this observation, we theoretically and experimentally quantified the effect of slope on the accuracy of treetop detection and its effect on the tree height estimation before and after height normalization.

The theoretical model presented the systematic error in LiDAR-derived treetop detection and height estimation as a function of terrain slope surface and tree crown radius. For a constant radius, the horizontal displacement increases asymptotically with the slope and reaches its maximum at a value equal to the radius size; the vertical displacement increases exponentially and goes to infinity as the slope approaches 90 degrees. For a constant slope, both the horizontal (i.e., treetop) and vertical

(i.e., height) displacement increase linearly, concomitantly with the crown radius. However, our idealized circular tree crown is different from the crowns that were measured as an average of two longest extending perpendicular directions in the field. This explains why we did not observe any correlation between the magnitude of the systematic error and the field crown size measurement. To better approximate other crown shapes, it would be possible to replace the circular crown contribution to the CHM-derived tree height estimate with various non-circular functions. Our idealized theoretical model is intended to show that terrain slope systematically creates an error for all crown shapes but the actual magnitude of this error will vary with each individual shape.

Our experimental results showed that the effect of CHM distortion on treetop displacement depends not only on the steepness of the slope but – more importantly – on the crown shape, which is mainly determined by species. The influence of the systematic error was only evident for the Scots pine trees (which are have a larger average crown size), not for the mountain pine trees (which have a narrow, conical crown with distinct apex). Holmgren and Persson (2004) reported that tree species conical in shape, such as the mountain pine, have a lower 90th LiDAR height percentile than Scots pine. This suggests that the LiDAR returns from the apical portion of mountain pine (i.e. the highest 10%) are distinctly higher than other canopy returns. Hence, no matter how steep the slope, the apical portion always becomes the local maximum in both the CHM and the DSM and is always identified as the correct treetop.

Our experimental results also showed that the effect of systematic error on horizontal displacement varies greatly among Scots pine trees. The probable reason is that the crown shape of Scots pine tends to differ with the age of the tree. Scots pine trees are conical when young but become more rounded and irregular as they mature (Holmgren and Persson, 2004; Ross et al., 1986). Local tree competition can also influence crown shape, with the resulting more slender and conical crown (Rouvinen and Kuuluvainen, 1997) being similar to the crown shape of mountain pine. The higher percentage of the commission error also confirmed that the Scots pine crown shape is more irregular than that of mountain pine.

Previous studies such as Popescu and Wynne (2004) and Kato et al. (2009) have reported that rounder crowns resulted in individual trees being falsely delineated by local maxima techniques.

According to the theoretical model, the height of LiDAR returns calculated from the distance between the highest crown return and its projection on the DTM on steep areas will be overestimated. Our experimental results confirmed that the average vertical displacement error between CHM-derived tree height and DSM-derived tree height was a positive value, i.e., an overestimation of tree height by CHM. The cause was obviously the horizontal downhill displacement of CHM-detected trees on sloping terrain. A few researchers have suggested that the tree height overestimation error might be caused by the differences between field-measured and LiDAR-derived heights on steeper slopes (Breidenbach et al., 2008; Takahashi et al., 2005; Véga and Durrieu, 2011). Our results demonstrate for the first time that – in steep terrain – the height normalization step causes systematic vertical errors, due to the horizontal displacement of treetops. Furthermore, we have shown that these errors depend on the crown shape of the species being measured. On the basis of our results, we recommend using raw elevation values (i.e., the un-normalized DSM) and computing the height after treetop detection and/or tree crown segmentation, in order to minimize the negative effect of steep slopes on the CHM, especially a heterogeneous forest type consisting of multiple species, or species which change their morphological characteristics as they mature.

3.6 Conclusions

We have theoretically and experimentally shown in this paper that the LiDAR height normalization process systematically reduces the accuracy of treetop detection when trees are located on sloping terrain. Our experiments also showed that the effect of slope-distorted CHMs on treetop detection strongly depends on the tree's crown shape, which is largely determined by its species. It would be interesting to investigate the effect of height normalization on various other non-conical crown shapes

(e.g., flat or ellipsoidal) located on terrain with a more complex topography (e.g. with gullies, mounds and other sudden local elevation changes).

Chapter 4

Generating spike-free digital surface models using LiDAR raw point clouds: A new approach for forestry applications*

* This chapter is based on:
Khosravipour, A., Skidmore, A.K., Isenburg, M., 2016. Generating spike-free digital surface models using LiDAR raw point clouds: A new approach for forestry applications. *International Journal of Applied Earth Observation and Geoinformation*, 52, 104-114.

Abstract

Accurately detecting single trees from LiDAR data requires generating a high-resolution Digital Surface Model (DSM) that faithfully represents the uppermost layer of the forest canopy. A high-resolution DSM raster is commonly generated by interpolating *all* first LiDAR returns through a Delaunay TIN. The first-return 2D surface interpolation struggles to produce a faithful representation of the canopy when there are first returns that have very similar *x*-*y* coordinates but very different *z* values. When triangulated together into a TIN, such constellations will form needle-shaped triangles that appear as *spikes* that geometrically disrupt the DSM and negatively affect treetop detection and subsequent extraction of biophysical parameters. We introduce a *spike-free* algorithm that considers all returns (e.g. also second and third returns) and systematically prevents spikes formation during TIN construction by ignoring any return whose insertion would result in a spike. Our algorithm takes a raw point cloud (i.e., unclassified) as input and produces a spike-free TIN as output that is then rasterized onto a corresponding pit-free DSM grid. We evaluate the new algorithm by comparing the results of treetop detection using the pit-free DSM with those achieved using a common first-return DSM. The results show that our algorithm significantly improves the accuracy of treetop detection, especially for small trees.

4.1 Introduction

In recent years, airborne LiDAR (Light Detection And Ranging) has become a common remote sensing technique for producing forest inventory data (Lim et al., 2003b). Due to its capability in providing accurate and spatially detailed information on tree structure elements (such as branches and foliage), LiDAR technology can improve the accuracy of forest parameter retrieval at the single-tree level (Duncanson et al., 2014; Hyyppä et al., 2008; Popescu, 2007; Véga and Durrieu, 2011). Acquiring accurate single-tree parameters from LiDAR data has significant applications in a variety of forest-related activities, including monitoring forest regeneration (Chen et al., 2006), sustainable forest management (Wulder et al., 2008), biomass and carbon stock estimation (Liu et al., 2010) and wildland fire risk assessment (Morsdorf et al., 2004).

As a basic unit for analysis in forestry applications, the individual tree detection approach (including treetop detection and crown delineation) has attracted much attention in the LiDAR research community (Duncanson et al., 2014; Hyyppä et al., 2012; Jing et al., 2012a; Koch et al., 2006; Li et al., 2012; Lu et al., 2014; Mongus and Žalik, 2015; Popescu and Wynne, 2004; Reitberger et al., 2009b). Unlike the optical imagery tree-detection approaches that are based on brightness or color variation (Pouliot et al., 2002), the LiDAR-based individual tree detection approaches use the geometric information captured by the LiDAR data. The initial step in most such methods relies on the generation of a Digital Surface Model (DSM) describing the geometry of the uppermost layer of the canopy (Hyyppä et al., 2008). Tree detection approaches identify the local maxima in the generated DSM that are considered to correspond to the positions of the treetops. Subsequently, the local maxima are used as reference points (or seed points) for crown delineation.

For such methods to be successful, the local maxima in the generated DSM have to correspond to actual treetops and for every actual treetop there needs to be a local maximum. The accuracy of local maxima detection relies on sufficiently high spatial resolution in the generated DSM, requiring a correspondingly high density of laser pulse footprints (Hyyppä et al., 2008; Lefsky et al., 2002). Local maxima techniques tend to use a

DSM with the highest possible resolution that represents the uppermost portion of the canopy layer with all the details that were captured. At very high spatial resolution (~10 cm) the morphology of individual trees can be detected (Wulder et al., 2000). With decreasing spatial resolution, the DSM no longer has sufficient detail to represent smaller trees, resulting in higher omission errors (undetected treetops). A low resolution DSM can easily be constructed by binning all points onto a grid and keep the highest elevation per grid cell. However, a simple binning approach is not suitable for constructing a DSM at the highest possible resolution supported by the LiDAR as many grid cells will remain empty while many others will be filled with unnaturally low elevation compared to their neighbors. Typically, a DSM at the highest resolution is generated by interpolating *all* first LiDAR returns – often by Delaunay triangulating them into a Triangulated Irregular Network (TIN) (Axelsson, 1999; Clark et al., 2004; Gaveau and Hill, 2003; Hyyppä et al., 2008). However, a first-return 2D surface interpolation struggles to produce a faithful representation of the canopy when there are first returns that have very similar *x*-*y* coordinates but very different *z* values (Axelsson, 2000). This happens when first returns are generated within the tree crown or on the ground below the canopy. When triangulated together into a TIN, such constellations will form needle-shaped triangles that appear as *spikes* (Figure 4.1 (left)) and result in cells with unnatural elevation values called *pits* when the TIN is rasterized onto a regular grid (Figure 4.1 (right)). These extreme irregularities significantly affect the geometric structure of the resulting high-resolution DSM. This reduces the accuracy with which local maxima correspond to actual treetops – increasing the errors of omission (undetected trees) and commission (falsely detected trees) (Khosravipour et al., 2014; Shamsoddini et al., 2013; Solberg et al., 2006; Van Leeuwen et al., 2010).

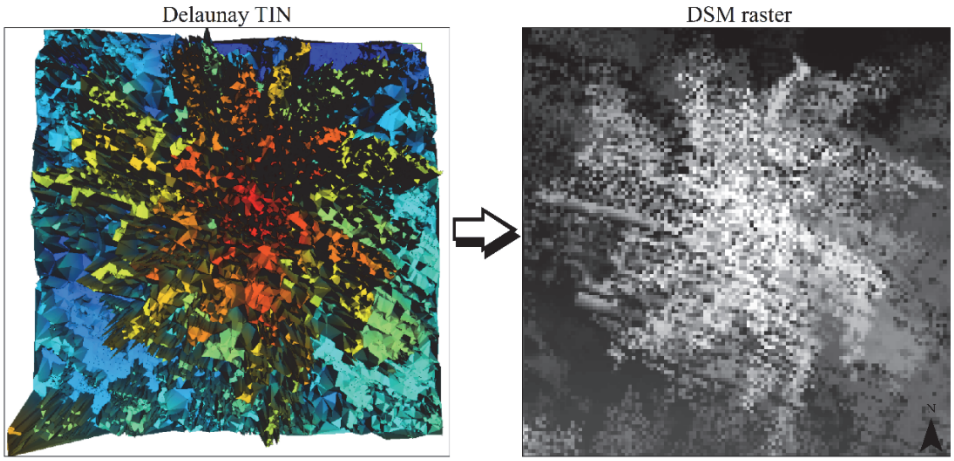

Figure 4.1: The generated Delaunay TIN using only first returns (left) and the corresponding DSM raster with a resolution of 0.15 m (right) for an individual tree.

The spikes usually appear in the TIN whenever a laser beam penetrates deeply into canopy branches and foliage before producing its first return (Ben-Arie et al., 2009; Persson et al., 2002). This not only causes the upper canopy surface to be underestimated (Gaveau and Hill, 2003; Lefsky et al., 2002) but also creates valleys within the crowns that make it difficult to discern individual crowns (Chen et al., 2006; Pitkänen et al., 2004). Spikes are also formed when merging flight lines, which is often done to sample the vegetation with a high-density LiDAR system (Hyyppä et al., 2008; Vauhkonen et al., 2012a). Because different flight lines scan the canopy from different directions, laser beams can "peek under" the tree crown and produce first returns far below the canopy in the understory and/or even on the ground (Leckie et al., 2003). This may even occur for individual flight lines at off-nadir scan angles. Finally, the planimetric error between overlapping flight strips that results from errors in the GPS and IMU measurements can also create such constellations (Vosselman, 2008) – especially for small-footprint LiDAR.

When rasterizing a first-return TIN onto a grid to create a raster DSM, many of the "spikes" in the TIN turn into "pits" in the raster. This is because the linearly-interpolated elevation value of any DSM raster cell whose x and y positions fall within a spike can be drastically different from that of its neighboring cells. A number of researchers, for example Chen

et al. (2006), have suggested filtering out first returns with low elevation by using a coarser grid before further interpolation, in order to avoid the chance of spike formation. However, this kind of filtering coarsens the DSM and thereby reduces the accuracy of individual treetop detection without necessarily removing all spikes. Other researchers have tried to remove pits from the DSM raster obtained by first-return TIN interpolation using raster-based techniques (e.g., Gaussian filter, pit-filling algorithm) (Ben-Arie et al., 2009; Brandtberg et al., 2003; Khosravipour et al., 2014; Persson et al., 2002; Shamsoddini et al., 2013; Zhao et al., 2013). However, the problem with such pit removal methods is that they do not exclusively target the sources of pit formation, but alter all pixel values in the DSM.

Another strategy to overcome the formation of spikes when interpolating all first returns is not to interpolate. Some researchers have suggested generating a grid of maxima DSM_{max} where each cell records the highest elevation value within a certain neighborhood (Leckie et al., 2003; Popescu et al., 2004). They report that compared with a first-return DSM, using a DSM_{max} can minimize pits and improve local maxima detection. However, if the chosen neighborhood is too large, the DSM_{max} will overestimate the surface model in accordance with the object properties, whereas if the chosen neighborhood is too small, pits will reoccur, especially at lower LiDAR point densities (Hollaus et al., 2010).

To avoid the complications with DSM generation altogether there are techniques that directly process the 3D point clouds using volumetric approaches (Reitberger et al., 2009b). Furthermore, some researchers have indicated that using all of the LiDAR returns can improve the detection rate of trees with small diameter at breast height (DBH), which are not usually captured by first returns, especially if the canopy is tightly interlocked and homogeneous (Li et al., 2012; Lu et al., 2014; Reitberger et al., 2009b). However, these newer point cloud-based techniques are computationally demanding and have only focused on small areas and may not be applicable across a larger range of forest types (Duncanson et al., 2014). One of these methods is alpha shapes approach. The concept of the *family of 3D alpha shapes*, introduced by Edelsbrunner and Mücke (1994), as it results in a concave surface. The alpha shapes approach was recently

used for generating geometric canopy structure from LiDAR data (Vauhkonen et al., 2015; Vauhkonen et al., 2012b). It is based on a 3D Delaunay tetrahedralization of all points and a parameter called alpha (α) that is used as a size criterion to determine the level of detail in the final result (Delfinado and Edelsbrunner, 1995).

In this study we describe a novel *spike-free* algorithm that generates a canopy surface at the highest resolution supported by LiDAR in the form of a spike-free TIN. The algorithm considers all *relevant* LiDAR returns and systematically prevents the formation of spikes during the TIN construction. The resulting spike-free TIN can either be used directly or be rasterized onto a grid in order to obtain a pit-free DSM raster. We first describe the spike-free algorithm and show results generated by this method. We then validate experimentally that using the pit-free DSM generated by our algorithm gives statistically significant improvements in the accuracy of treetop detection compared to using a first-return DSM.

4.2 Material

4.2.1 Study area

The Bois Noir forest (44° 23′ N, 6° 45′ E) is a part of Barcelonnette basin in the southern French Alps. The northern part of the study area is characterized by complex topography, with slopes ranging from 10° to 30° (Thiery et al., 2007) and the southern part is characterized by extensive steep slopes of up to 70° (Razak et al., 2011b). The area is about 1.3 km^2 and the vegetation cover is mainly mountain pine (*Pinus uncinata*), Scots pine (*Pinus sylvestris*) and a few larch (*Larix decidua*), Norway spruce (*Picea abies*) trees, mixed with deciduous broadleaved trees such as aspen (*Populus tremula*) and ash (*Fraxinus excelsior*).

4.2.2 LiDAR data

The LiDAR data were acquired during the leaf-on season in July 2009, using a helicopter flying about 300 m above the ground (Table 4.1). The small-footprint full-waveform airborne laser scanning system (RIEGL VQ-480i) utilized by Helimap has been developed specifically for mapping mountainous forested area (Vallet and Skaloud, 2004). The

system performs on-line full-waveform analysis to extract up to five discrete returns from the waveforms. The mean point density was 160 point/m^2 when counting all returns and 116 point/m^2 when counting only the last returns.

Table 4.1:The airborne laser scanning characteristics.

Acquisition (month/year)	July- 2009
Laser scanner	Riegl VQ480i
IMU system	iMAR FSAS - record 500Hz
GPS system	Topcon legacy - record 5Hz
Laser pulse repetition rate	300 kHz
Measurement rate	Up to 150 000 s^{-1}
Laser wavelength	Near infrared
Beam divergence	0.3 mrad
Laser beam footprint	75 mm at 250 m
Field of view	60°
Scanning method	Rotating multi-facet mirror

4.2.3 Field data

The following field inventory data were collected during September 2011 and 2012: tree location, tree stem DBH, tree crown diameter (CD) as well as tree species (Table 4.2). A Nikon hand-held laser rangefinder was used for tree height measurements. However, the treetops could not be seen, due to density of the canopy. Therefore, we could not collect accurate tree height measurements in the field for validating our high density LiDAR dataset. The position of individual trees and the central points of each plot were collected using a Leica 1200 Differential GPS and a Total Station. The crown diameter was measured with an average of two perpendicular directions to more accurately approximate crown diameter of each tree in every plot (Song et al., 2010). The total number of sampled trees was 694.

Table 4.2: Descriptive statistics for the tree field measurements.

	All (n= 694)		deciduous (n= 33)		Larix (n= 29)		Pinus sylvestris (n=325)		Pinus uncinata (n=307)	
	DBH (cm)	CD (m)	DBH (cm)	CD (m)	DBH (cm)	CD (m)	DBH (cm)	CD (m)	DBH (cm)	CD (m)
Min	7	0.5	13	1.5	13	3.7	8	0.9	7	0.5
Max	61	9.1	43	6.3	61	8.9	59	9.1	41	6.7
Median	23	2.6	25	3.8	36	6	25	3.4	20	1.7
Mean	24.1	3	24.8	3.6	34.9	6.2	26	3.6	20.9	1.9
SD	8.2	1.6	9.4	1.3	10.5	1.4	8.5	1.4	5.4	0.9

4.3 Methods

In this section, we describe a new method for generating a DSM using all *relevant* LiDAR returns. Our algorithm takes a raw point cloud (i.e., unclassified) as input and generates a spike-free TIN as output that is then rasterized onto a corresponding pit-free DSM at a user-defined resolution.

4.3.1 Description of spike-free DSM algorithm

Similar to the standard approach for generating a DSM from LiDAR, our algorithm first constructs a TIN that is then rasterized. However, instead of using only the first LiDAR returns, our algorithm considers all returns in constructing the TIN. This allows all relevant LiDAR returns (e.g. also second and third returns) to contribute toward capturing the details of the uppermost canopy layer in the DSM.

The core idea of our algorithm is to preferentially connect LiDAR returns into TIN triangles that are nearby not only in x and y, but also in z. After all, downward spikes in the TIN are the result of connecting LiDAR returns that are close in x and y but very distant in z (Axelsson, 1999). This is consistent with Tobler (1970)'s first law of geography: "everything is related to everything else, but near things are more related than distant things". Which – applied to our case – suggests that small triangles connecting nearby points are more relevant for accurately representing the canopy surface than triangles with very long edges.

Using all returns, our algorithm constructs a TIN, starting from the highest points and using an incremental Delaunay algorithm. It orders the LiDAR points by their z coordinate and inserts them into the TIN one by one, in order of decreasing elevation (Figure 4.2). At any time the algorithm maintains the invariant that the TIN is a Delaunay triangulation, or rather a constrained Delaunay triangulation (Chew, 1987) where any edge declared "constrained" is allowed to violate the empty-circle criterium of the standard Delaunay triangulation.

After inserting a certain number of points, the algorithm "freezes" all triangles whose three edges (in the *x*/*y* plane) are each shorter than a certain value, called the *freeze distance* (see Figure 4.2). This is done by constraining all three edges of such triangles in the Constrained Delaunay TIN. Such frozen triangles are final and will not change when the remaining points of lower elevation are inserted into the TIN. Whenever a point of lower elevation falls directly onto a frozen triangle it is simply ignored and not added to the Constrained Delaunay TIN. This freezing of higher-up triangles is what prevents the formation of downward spikes that would otherwise turn into "pits" in the rasterized DSM.

Before our algorithm starts freezing triangles, it needs to insert sufficient neighboring LiDAR points into the TIN. Therefore freezing does not start until all points have had the opportunity to form triangles with all their nearby points in a vertical downward direction (Figure 4.2 (a)). This is needed to prevent the freezing mechanism from producing artifacts in the TIN that would result from prematurely constraining triangles. Therefore, we maintain an *insertion buffer* to ensure that all triangles that still have a point in the buffer will not be frozen. This insertion buffer defines a vertical zone of a certain height starting at the elevation of the return that was last inserted.

Hence, our algorithm has two user-definable variables: the length of the *freeze distance* and the height of the *insertion buffer.* In the following section, we describe how to define these variables.

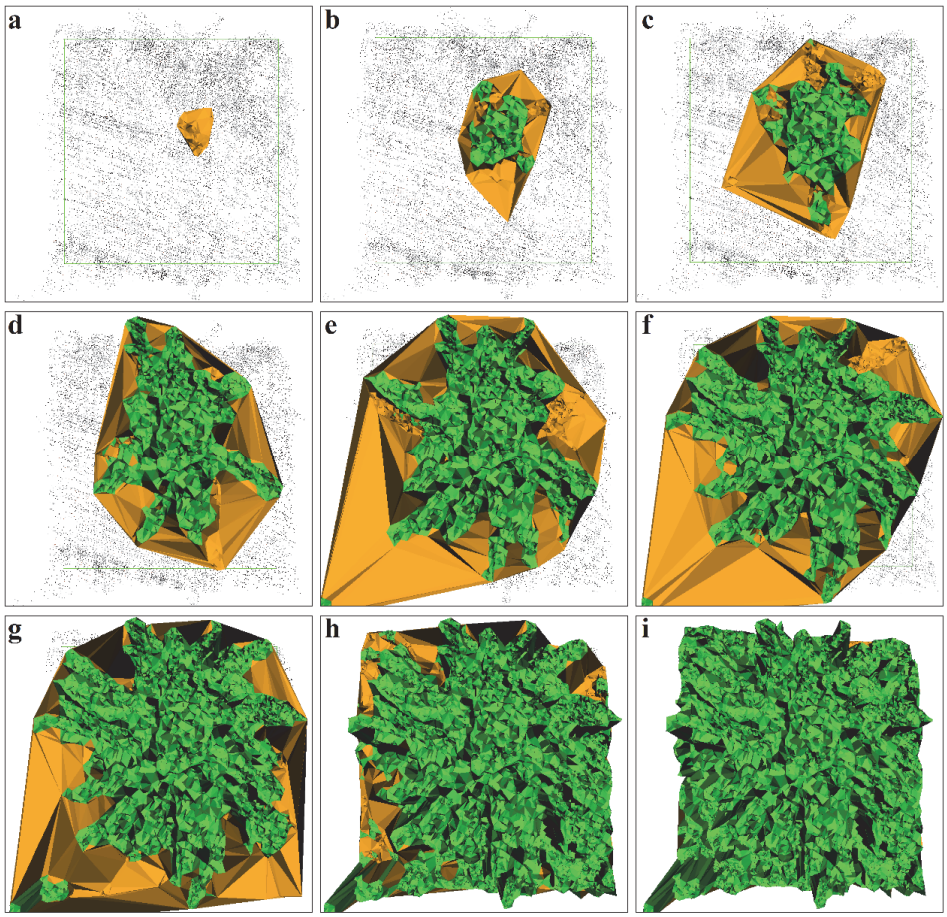

Figure 4.2: Sequence of illustrations (a to i) showing the construction of a spike-free TIN for an individual tree. The algorithm iteratively inserts all LiDAR returns from top to bottom and freezes all small triangles (green triangles) whose three edges are each shorter than 0.4 m and whose three points have all left the insertion buffer of 0.5 m. In frame (a) the freezing has not started because all points are still in the insertion buffer.

4.3.1.1 Freeze distance

To prevent the formation of spikes in the canopy surface, our algorithm freezes all triangles whose three edges are each shorter than a user-specified distance. We choose this distance such that a triangle is frozen once it reaches its target size in the sense that its three edges reach their *expected* lengths. The expected edge lengths of a triangle is related to the LiDAR *Nominal Pulse Spacing (NPS)*, which expresses the typical or average lateral distance (i.e. the horizontal distance in the *xy*-plane between the pulses) between pulses in a LiDAR dataset (Baltsavias, 1999).

Typically, the NPS is calculated as the square root of the average area, using only one return per pulse (i.e. only the last return or only the first return) as a surrogate for pulses (Heidemann, 2012). The NPS expresses the expected *xy* distances between the pulses, using a single swath on flat and open terrains for an idealized survey with nadir-only pulses of regular distribution. Under such idealized conditions, the NPS is identical to the expected length of all edges in a corresponding Delaunay TIN. For a real-world survey with multiple passes over sloped terrain and dense vegetation where the pulse distribution is neither regular nor evenly spaced, the average or *Aggregate Nominal Pulse Spacing (ANPS)* is used (Heidemann, 2012). The ANPS can be calculated by constructing a Delaunay triangulation of the last return of each pulse and by averaging the length of all edges, leaving out those associated with points on the convex hull (Balsa-Barreiro and Lerma, 2014; Shih and Huang, 2006).

Our aim is to freeze triangles in higher elevations as soon as their three edges have reached their *expected length* given the pulse spacing. The frequency distribution of edge lengths yields a histogram over the range of actual pulse spacing within our survey. The 99th percentile of this histogram covers the edge lengths we can *expect* given the actual pulse spacing, with the remaining percent corresponding to unusually long edges at the boundary or/and across water bodies. For our dataset, this 99th percentile is 0.4 m (Figure 4.3). This value was used as the freeze distance. We have informally tested this heuristic with other (lower) density LiDAR data sets and it yields a reasonable compromise between accuracy and pit formation.

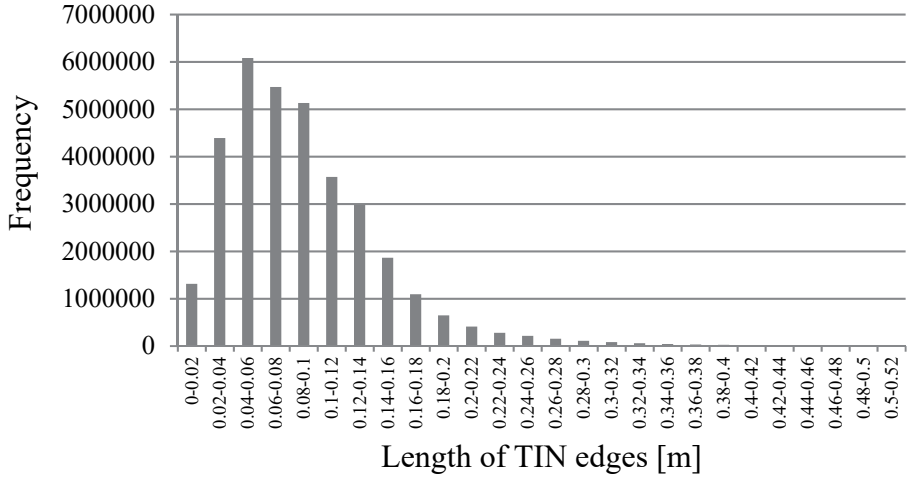

Figure 4.3: Histogram of edge length of a last-return Delaunay TIN.

4.3.1.2 Insertion buffer

The insertion buffer prevents the generation of artifacts in the TIN by delaying the freezing process. If the algorithm freezes triangles directly after inserting the points that created them (i.e. uses a zero insertion buffer), triangles may be frozen before all relevant neighboring returns have been inserted into the TIN. This means that freezing would distort the structure of TIN everywhere, even in areas without spikes. Moreover, the insertion buffer controls the depth of "allowed" spikes by defining a vertical zone within which the triangulation remains unconstrained from freezing. If the algorithm freezes triangles too late (i.e. uses a too large insertion buffer) the TIN could be full of additional spikes, as our algorithm considers not just the first but all returns for insertion. In particular, many spikes would be generated when two subsequent returns from the same pulse (e.g., the first and the second) are triangulated together (Figure 4.4). Thus, the buffer size should definitely not be larger than the minimum vertical distance between two returns of the same pulse.

The smallest possible distance between subsequent returns of the same pulse depends on the scanning hardware (Gaveau and Hill, 2003). According to the manufacturer, the reliable multi-target range for the VQ-

480i scanner starts at 1.0 m (RIEGL, 2015). We chose an insertion buffer size of 0.5 m, which was a reasonable size in view of our experiments.

We assessed the accuracy of individual tree detection, using the final pit-free DSM to evaluate our choice of variables for the spike-free algorithm (i.e. a freeze distance of 0.4 m and an insertion buffer of 0.5 m) for generating a high-resolution DSM.

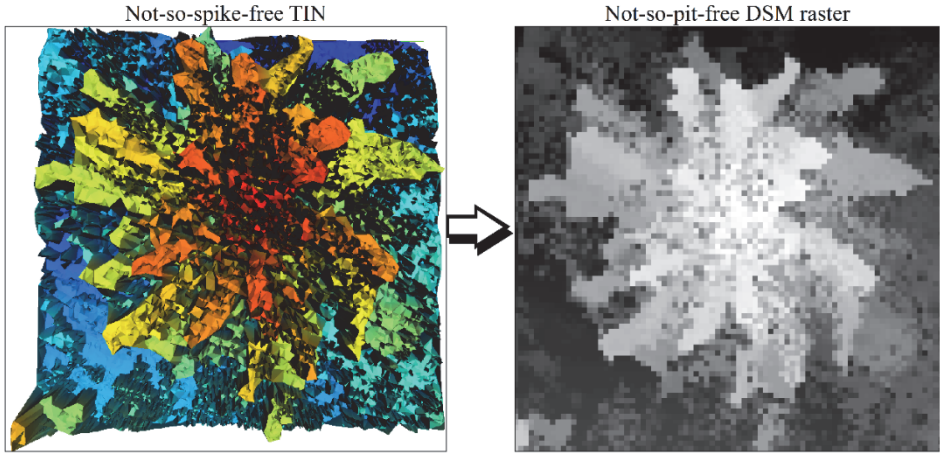

Figure 4.4: Additional spikes and pits appear in the not-so-spike-free TIN (left) and the not-so-pit-free DSM (right) when using a too large insertion buffer of 5.0 m.

4.3.1.3 Generating a raster-based pit-free DSM

The pit-free DSM is generated through simple linear interpolation of the spike-free TIN (Figure 4.5 (left)) onto a raster (Figure 4.5 (right)). The cell size is a key parameter for rasterizing a DSM, especially for accurate derivation of treetops (Chen et al., 2006) . The cell size cannot be bigger than half the size of the minimum object of interest (e.g. the tree crown size) as Nyquist sampling theory tells us (Nyquist, 1928). It should also not be much smaller than the average pulse spacing (Chow and Hodgson, 2009). We therefore use a grid size of 0.15 m for the pit-free DSM, which is sufficient for recognizing the minimum crown diameter of 0.50 m recorded in the field and is well supported by our pulse spacing of 0.09 m.

We used a working prototype of this algorithm, which was implemented as part of the LAStools software suite (rapidlasso GmbH, 2015).

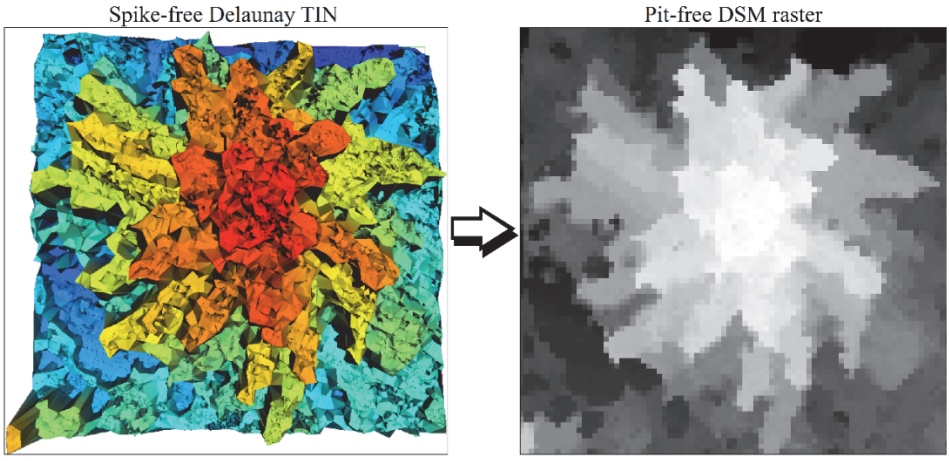

Figure 4.5: The generated spike-free Delaunay TIN using all relevant returns (left) and the corresponding pit-free DSM raster with a resolution of 0.15 m (right).

4.3.2 Individual tree detection

Unlike most methods that first height-normalize the DSM before detecting treetops, we directly use the pit-free DSM for the treetop detection. The normalized DSM (nDSM) – also called Canopy Height Model (CHM) – can be generated by subtracting a Digital Terrain Model (DTM) from the DSM raster. However, using a CHM to detect treetops results in systematic errors when trees are on sloping terrain (Khosravipour et al., 2015), so the direct use of a DSM is recommended for extracting treetops from forests on topographically complex terrains (Vega et al., 2014).

For treetop detection, a method based on the morphological opening and reconstruction was applied to the DSMs. The morphological opening operations (erosion and dilation) with an appropriate structural element are well known for separating differently sized objects (Serra, 1982; Vincent, 1993) and preserving the structure of each object (Wang et al., 2004) in a gray-scale imagery. Previous researchers have stated that the structural element is set empirically for each case study (Jing et al., 2012b). We followed Khosravipour et al. (2015) who used morphological opening for identifying treetops in this study area. They found experimentally that a flat disk with a diameter of 1.05 m (7 pixels in size) was an appropriate structural element for detecting treetops given the minimum object of interest (minimum crown diameter is 0.50 m) and the 0.15 m pixel

resolution. The purpose of the opening operation is to remove "*foreground*" objects (i.e., treetops) that are smaller than the structural element in the DSM raster, and to generate an *opened image*. Then the morphological reconstruction is applied. The previously generated opened image is then selected as a *marker* under the original canopy surface (i.e. the original DSM) – which is used as the *mask* image – in order to retrieve the shape of tree crown boundaries that were smoothed by the opening operation. The subtraction of the resulting reconstructed image from the original DSM gives us the *regional maxima* image. Finally, for each area of the DSM that has a corresponding component in the regional maxima image a local maximum is extracted. These local maxima are the estimated treetop to which *x*, *y* and *z* coordinates are attributed.

4.3.2.1 Accuracy assessment of individual tree detection

The performance of treetop detection was evaluated by comparing the detected local maxima with the trees measured in the field. For each tree species, if one local maximum had been detected within a reference crown boundary, the detection was considered to be correct. If more than one local maximum was detected within a reference crown boundary, the closest one was considered to be a correctly detected tree, and the others were then defined as commission errors. If no local maximum was detected, this error was considered as an omission error. Subsequently, the overall accuracy of the tree detection was calculated by the Accuracy Index (AI) as expressed by Pouliot et al. (2002):

$$AI\ (\%) = \left[(n - O + C)\right)/n] \times 100$$

where n is the number of reference trees in the study area, O is the omission error and C is the commission error.

4.4 Results

A visual comparison demonstrates that our spike-free algorithm is able to produce a high-resolution DSM without pits. Figure 4.6 details a pit-free DSM side by side with a standard DSM generated by first-return interpolation, with their associated x-axis histograms. The spike-free algorithm successfully removed all pits – small dark squares – by

constraining the TIN construction to ensure that the only LiDAR returns connected in the final triangulation are those that are nearby when hitting the canopy at various levels. By observing the original profile, pits are clearly visible in the standard DSM generated by a TIN that simply interpolates all first returns. Interestingly, the top of the low vegetation (Figure 4.6) is well sampled in the pit-free DSM because our algorithm is considering all relevant returns when constructing the TIN. However, when using only first returns these canopy details are lost in the final DSM. In order to evaluate the utility of the pit-free DSM for forest area management, the treetop detection method was applied both to the first-return DSM raster and to our pit-free DSM raster.

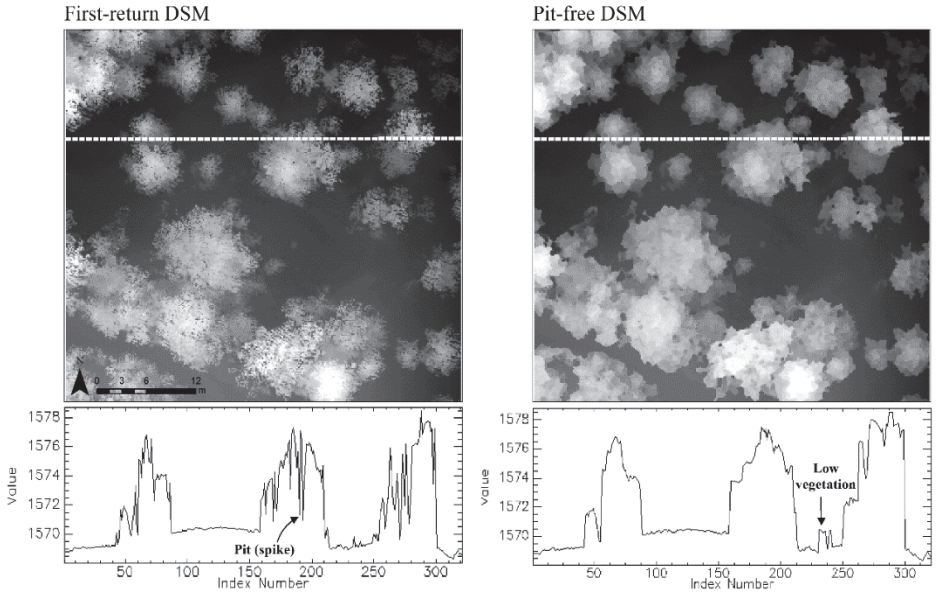

Figure 4.6: A visual comparison of the x-axis profile of pit-free DSM derived from the spike-free algorithm (left) with that of a standard DSM derived from a first-return interpolation (right). The x-axis represent pixel values from the white dashed line in the corresponding DSMs.

Figure 4.7 shows an example of correctly detected treetops, omission errors and commission errors in the pit-free DSM compared to the first-return DSM. Table 4.3 presents the number and percentage of correctly detected trees, omission, commission errors and the overall AI, assessed for different tree species. The results demonstrate that the total accuracy

index for tree detection from the pit-free DSM (80.5 percent) is higher than that from the first-return DSM (65.7 percent). The chi-square test showed a statistically significant difference between the number of correctly detected trees in the pit-free DSM (594) and the first-return DSM (482): $x^2 = 51.863$, and $p = 0.00$. When considering the treetop detection accuracy across different tree species, the pit-free DSM achieved greater accuracy for both deciduous broadleaved and coniferous trees.

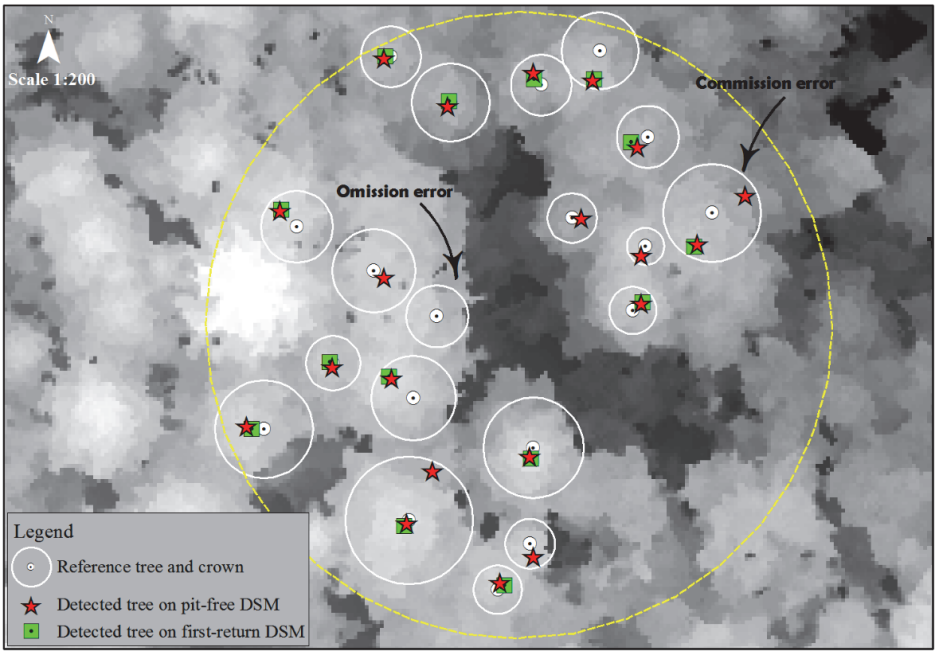

Figure 4.7: Visual representation of correctly identified treetops, omission errors, and commission errors of the first-return DSM versus the pit-free DSM.

For two deciduous species *(Fraxinus excelsior, Populus tremula)*, the detection accuracy was 63.6 percent for the pit-free DSM and 54.5 percent for the first-return DSM. The overall accuracy index rate was higher for the 29 measured *Larix decidua* trees. However, there was no *significant* difference in detecting trees for deciduous broadleaved trees ($x^2 = 2.853$, and $p = 0.10$) and *Larix decidua* ($x^2 = 1.074$, and $p = 0.30$). For *Pinus sylvestris* and *Pinus uncinata*, the chi-square test indicated a significant difference between the pit-free DSM and the first-return DSM, with the pit-free DSM resulting in a higher number of correctly detected *Pinus*

sylvestris trees (x^2 = 12.941, and p = 0.00) and *Pinus uncinata* trees (x^2 = 38.741, and p = 0.00).

Table 4.3: Tree detection results for the first-return DSM and pit-free DSM.

Field-measured trees		First-return DSM				Pit-free DSM			
number of trees	Species	Correct n (%)	Omission n (%)	Commission n (%)	AI (%)	Correct n (%)	Omission n (%)	Commission n (%)	AI (%)
33	Deciduous (broadleaved trees)	20 (60.6)	13 (39.4)	2 (6.0)	54.5	26 (78.8)	7 (21.2)	5 (15.1)	63.6
29	Larix decidua	26 (89.7)	3 (10.3)	7 (24.1)	65.5	28 (96.5)	1 (3.5)	6 (20.6)	75.9
325	Pinus sylvestris	240 (73.9)	85 (26.1)	15 (4.6)	69.2	277 (85.2)	48 (14.8)	23 (7.0)	78.2
307	Pinus uncinata	196 (63.9)	111 (36.1)	2 (0.6)	63.2	263 (85.7)	44 (14.3)	1 (0.3)	85.3
694	Total	482 (69.5)	212 (30.5)	26 (3.7)	**65.7**	594 (85.6)	100 (14.4)	35 (5.0)	**80.5**

The range of DBH values in this study (Table 4.4) allowed us to assess how the proposed pit-free DSM algorithm improves the detection of small trees by comparison with the first-return DSM derived from first LiDAR returns. Based on the DBH distribution (Table 4.2), the range in DBH was classified into three classes: DBH less than 20 cm, DBH from 20 – 40 cm and DBH greater than 40 cm. A chi-square test demonstrated a statistically significant difference between the pit-free DSM and the first-return DSM in detecting trees with DBH of less than 20 cm (x^2 = 26.237, and p = 0.00) and DBH between 20 to 40 cm (x^2 = 29.505, and p = 0.00). There is no difference between the DSMs in detecting trees with DBH greater than 40 cm.

Table 4.4: Proportion of correctly detected trees for three DBH ranges for the first-return DSM and the pit-free DSM.

	All (n= 694)		
Portion of DBH range (cm)	< 20 (n = 258)	20 to 40 (n = 397)	> 40 (n = 39)
First-return DSM	150 (58.1%)	299 (75.3 %)	33 (84.6 %)
Pit-free DSM	204 (79.0 %)	357 (90.0 %)	33 (84.6 %)

4.5 Discussion and conclusions

This paper focuses on improving the input raster for algorithms that perform treetop detection on a 2D canopy surface. Generating such a high-resolution raster by standard interpolation of only the first returns tends to give a poor representation of the canopy structure. Often there are first returns with similar *x*-*y* coordinates but very different *z* elevations that are scanned from different canopy layers and/or the ground. These first returns are vertically above each other and therefore form needle-shaped triangles that appear as *spikes* when interpolated by a Delaunay triangulation. When such a TIN is rasterized onto a regular grid the spikes often result in cells that are called *pits* because their value is of abruptly lower elevation than that of their neighboring cells. In this study, we propose a novel "spike-free" algorithm which systematically prevents the formation of spikes during the TIN construction. Our method considers all LiDAR returns (e.g. also second and third returns) but ignores all those returns whose insertion would result in a spike. By considering the contribution of all relevant returns, our algorithm can also model details in the canopy structure that are also captured by intermediate or last returns. Our experimental analysis clearly demonstrated that a DSM generated by the spike-free algorithm significantly improves treetop detection.

We verified experimentally that the freeze distance derived from the actual pulse spacing yields the best results in terms of covering all spikes without connecting nearby features. If we use a smaller freeze distance, fewer triangles are frozen and "spikes" reappear in the canopy surface. This increases commission errors in treetop detection, as it becomes more likely that individual crowns are fragmented into multiple local maxima. If we use a larger freeze distance, triangles are frozen too early and details of the morphological structure of the canopy are lost. This increases the omission error, as it becomes more likely that neighboring crowns are joined together.

We should point out that a fixed value for the freeze distance will not be optimal when the pulse spacing varies locally across the dataset. This may happen when merging different numbers of overlapping flight lines, or when there are sudden changes in the pitch of the aircraft due to flight

turbulence that compress or stretch the spacing of subsequent scan lines. Moreover, scanning systems that are based on oscillating mirrors exhibit systematic changes in pulse spacing along and across scan lines (Wehr and Lohr, 1999). In the future it may be useful to locally adapt the freeze to the observed pulse spacing in order to further improve the accuracy of the algorithm.

The insertion buffer prevents the freezing mechanism from generating unwanted artifacts in the TIN and controls the depth of "allowed" spikes. Although we have confirmed the suitability of a 0.5 m insertion buffer for detecting individual trees, its size does affect the results of our algorithm. Using a size larger than the minimum distance between subsequent returns of the same pulse defeats the whole purpose of freezing and results in additional spikes. Using a size smaller than the vertical neighborhood of points affects the quality of the TIN as many thin and skinny triangles that would usually only exist temporarily become permanently frozen. We believe that the ideal buffer lies somewhere between a *minimum buffer* that does not affect TIN quality and a *maximum buffer* that does not result in excessive spikes. In future studies it would be interesting to determine an ideal insertion buffer size by testing how different sizes affect the overall result for a particular application.

We investigate the robustness and transferability of the freeze and the buffer parameters for other forest types scanned by different LiDAR systems in our current research.

4.5.1 Comparison with prior algorithms

To our knowledge, this is the first study that has rigorously removed spikes from a TIN during the triangulation of raw point clouds for the purpose of DSM generation. Most previous "pit-removal" algorithms are pixel-based smoothing techniques (e.g. Gaussian, median and mean filtering) that operate on the final raster (Chan et al., 2005; Dralle and Rudemo, 1996). They usually alter all pixels of the raster by smoothing their values according to their neighbors, which often reduces the accuracy of tree top detection by increasing the omission error (Solberg et al., 2006).

The only comparable method is the pit-free CHM algorithm developed by Khosravipour et al. (2014) that also avoids smoothing. It generates a stack of CHMs that are partially pit-free – each representing a different height interval of the canopy – and which are then merged in a final step into a pit-free CHM. The main similarity is the "rasterization threshold" that tries to ensure that only triangles connecting first returns from the same tree crown are rasterized, which is basically identical to the freeze distance we use here. However, there are five main differences:

(1) The pit-free CHM algorithm is impractical for generating pit-free DSM rasters due to the excessive number of partial DSM that would be required – especially for steep terrains. Our new spike-free algorithm does not require partial rasters.
(2) The pit-free CHM algorithm controls the depths of pits via a set of "height thresholds", and reducing their spacing increases the number of partial CHMs. Our new spike-free algorithm controls the depths via the "insertion buffer" instead.
(3) The pit-free CHM algorithm rasters all triangles below the "rasterization threshold", no matter how poorly shaped. Our new spike-free algorithm uses an "insertion buffer" to ensure all nearby points arrive before triangles are frozen.
(4) The pit-free CHM algorithm used only the first returns, potentially missing canopy details captured by second, third, or fourth returns. Our new spike-free algorithm chooses the most relevant from all returns.
(5) The pit-free CHM algorithm can only output a pit-free raster as the final result. Our new spike-free algorithm can output both, a spike-free TIN and a pit-free raster.

Our spike-free algorithm has similarities with the alpha shape approach. This technique entails removing each simplex – a tetrahedron – of their 3D Delaunay tetrahedralization whose (empty) circumscribing sphere has a squared radius larger than the α-shape value (Edelsbrunner and Mücke, 1994). The final alpha shape is the boundary enclosing all remaining tetrahedral; it can be concave and even disconnected (i.e., one or multiple surface components of any genus). In contrast, our algorithm neither

inserts all points (i.e. those falling on frozen triangles are ignored) nor removes any simplices – here triangles – from our Constrained 2D Delaunay triangulation (but it freezes triangles whose edges are smaller than the freeze distance). The final result of our spike-free algorithm is a triangulation that is equivalent to a planar graph – a single connected surface with a genus of zero.

4.5.2 Comparison with prior results

Previous studies have reported treetop detection accuracy in the range of 40% to 70% for a first-return DSM raster (Persson et al., 2002; Pitkänen et al., 2004; Yu et al., 2011) but with less than 20% accuracy for intermediate and small trees (Kaartinen et al., 2012). Our experiments demonstrated that a significant improvement in treetop detection using the pit-free DSM (80% accuracy) compared to the first-return DSM (65% accuracy). Our experiments further improve on the result of Khosravipour et al. (2014), which have used a pit-free CHM. They reported accuracies from 50% to 70% in deciduous and coniferous trees, while our results provided tree detection rates ranging from 60% to 80% for deciduous and coniferous trees and 80% to 90% accuracy for detecting small trees with DBH of less than 20 cm and 40 cm.

Our findings appear to be in the range of values reported by techniques operating directly on the 3D point clouds, with detection rates varying from 70% to 90% (Li et al., 2012; Lu et al., 2014; Reitberger et al., 2009a; Vega et al., 2014). This means our novel DSM generation method is capable not only of significantly improving treetop detection, but also of competing with significantly more complex 3D point cloud techniques that require much more computation power. Our algorithm may prove to be a more practical method for treetop detection at the local or regional scale.

4.5.3 other opportunities

The spike-free algorithm offers the possibility of improving the extraction of other tree crown component characteristics critical to forest management, such as the length of the green crown and crown diameters. It yields a DSM at the highest resolution supported by the LiDAR density, while keeping the most relevant of all returns, which has the potential to

capture more details about the canopy structure. It may also prove useful for improving the estimation accuracy for tree heights, and subsequent biophysical parameters such as biomass and carbon.

The spike-free algorithm was originally developed solely for application in forestry. However, initial experiments show that it also gives noticeable improvements when applied to LiDAR from urban scenes, especially along building edges. Any feature that an off-nadir pulse can "peek" under, such as eaves of roofs, covered walkways, or bridges, results in excessive spikes in a first-return DSM and significant distortions in the corresponding raster. In all such cases, our spike-free algorithm can produce a cleaner surface with better-defined edges (see Figure 4.8). This could prove useful for automated reconstruction of building outlines from DSMs.

We should point out that the DSM produced by the spike-free algorithm may not necessarily be better for all applications. For example, when computing a hill-shading for visualization purposes it seems that excessive aliasing in the shaded image due to spikes in the first-return DSM result makes it easier to visually discern individual trees in an urban scene or distinguish certain types of vegetation.

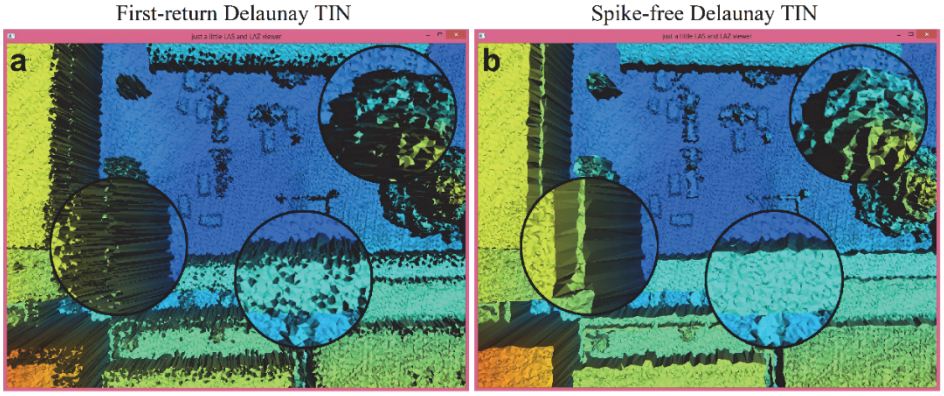

Figure 4.8: A visual comparison of a first-return TIN (a) and spike-free TIN (b) for an urban area. The data is courtesy of the open-access for Canton Zurich in Switzerland.

Chapter 5

Comparative testing and evaluation of LiDAR-derived spike-free digital surface models for individual tree detection across multiple forest ecosystems*

* This chapter is based on:
Khosravipour, A., Skidmore, A.K., Isenburg, M., Hussin, Y.A., Jones, S.D., Heurich, M., Bradford, M., 2016. Comparative testing and evaluation of LiDAR-derived spike-free digital surface models for individual tree detection across multiple forest ecosystems. resubmitted: *Agricultural and Forest Meteorology*.

Abstract

A main challenge, when using LiDAR data to detect individual trees, is the strong effect the method used to derive the Digital Surface Model (DSM) from the LiDAR data can have on the accuracy. Commonly used methods that interpolate first, highest, or last LiDAR returns often struggle to produce a reliable representation of canopy surface. The recently developed spike-free algorithm, however, considers all LiDAR returns, but only uses those it deems relevant for generating the DSM raster. In this study, we evaluate the impact of both forest complexity and number of LiDAR pulse density on the performance of the spike-free algorithm for detecting individual treetop using LiDAR data. We also compared the accuracy of treetop detection achieved with a spike-free DSM to the accuracies achieved with DSMs generated from first, highest and last returns. Three different case studies, with three different real-work LiDAR pulse densities and two thinned datasets, were selected in order to evaluate the performance of spike-free free DSM: a temperate plantation in France (116 LiDAR pulse/m^2 and a thinned dataset of 5 pulse/m^2), temperate mixed deciduous-coniferous forest in Germany (16 LiDAR pulse/m^2 and a thinned dataset of 5 pulse/m^2) and a tropical rainforest in Australia (5 LiDAR pulse/m^2). The results show that the spike-free algorithm improved the accuracy of treetop detection across multiple forest types and LiDAR of different pulse densities. The map accuracy is affected by both the LiDAR pulse density and forest complexity. After normalizing datasets to an equal LiDAR density, the highest accuracy based on the spike-free algorithm was obtained within the Bois Noir forest in France, a coniferous plantation. The lowest detection result was obtained at Robson Creek in Australia, a mix of multi-layered broad-leaved schlerophyllous trees.

5.1 Introduction

Forests are three-dimensional (3D) systems that have a significant impact on ecosystem function and structure, and figure prominently in any discussion of terrestrial essential biodiversity variables (EBVs) (Pettorelli et al., 2016; Skidmore et al., 2015). Accurate measurement and monitoring of forest structural parameters are increasingly needed across multiple ecosystems and spatial scales to support a variety of activities related to sustainable forest management, biomass/carbon estimation and understanding the impacts of natural and anthropogenic influences on biodiversity (Rosenqvist et al., 2003; Wu et al., 2016; Wulder et al., 2012). Forest tree structure can be described by various attributes, such as tree position, tree height, crown size, as well as species that are closely linked with ecosystem function (Palace et al., 2015; Spies, 1998). Small-footprint airborne Light Detection and Ranging (LiDAR) systems offer an efficient remote sensing technique for acquiring forest structural variables capable of providing detailed and accurate 3D information (Lim et al., 2003b). The advantages of LiDAR-based forest inventory have been detailed for a wide variety of forest ecosystems worldwide, ranging from boreal (Hyyppä et al., 2008; Vastaranta et al., 2011) to temperate (Amiri et al., 2016; Latifi et al., 2015) and tropical ecosystems (Asner and Mascaro, 2014; Ferraz et al., 2016).

As a basic unit for identifying forest variables, the individual tree detection approach (including treetop detection and crown delineation) has attracted much attention in the LiDAR research community (Brandtberg et al., 2003; Koch et al., 2006; Leckie et al., 2003; Li et al., 2012; Mongus and Žalik, 2015; Pitkänen et al., 2004). Numerous individual tree detection approaches utilizing LiDAR data, have been developed in the past, such as Region Growing (Hyyppä et al., 2001), Watershed (Chen et al., 2006) and Normalized Cut (Yao et al., 2012). What the most popular individual tree detection approaches have in common is that they first identify local maxima that correspond to the positions of treetops (Duncanson et al., 2014; Mongus and Žalik, 2015; Vastaranta et al., 2011; Véga and Durrieu, 2011; Zhang et al., 2014). Trees are typically detected using a search radius (i.e., window size) that moves systematically across either the original

LiDAR raw data point clouds (Ferraz et al., 2012; Li et al., 2012; Lu et al., 2014; Reitberger et al., 2009b; Yao et al., 2012) or the LiDAR-derived DSM raster – or a normalized DSM (nDSM) also known as Canopy Height Model (CHM) (Chen et al., 2006; Duncanson et al., 2014; Heurich, 2008; Jing et al., 2012a; Wu et al., 2016). The LiDAR-detected local maxima are later used as reference points (or seed points) for crown segmentation and height estimation (Monnet et al., 2010; Popescu and Wynne, 2004; Véga and Durrieu, 2011; Zhang et al., 2014).

The main challenges faced in local maxima detection are omission errors (missed trees) and commission errors (falsely detected trees). It is claimed that these errors mainly rely on the quality of acquired LiDAR data, the data processing and the forest complexity (Eysn et al., 2015; Kaartinen et al., 2012; Vauhkonen et al., 2012a; Zhen et al., 2016). For example, augmenting the density of laser pulse footprints increases the chance of the laser sampling the "true" treetop, irrespective of whether the approaches are based on a raster DSM or the point cloud (Chen et al., 2006; Lefsky et al., 2002; Li et al., 2012; White et al., 2016). To reduce omission and commission errors, an efficient local maxima technique is required – in others words, an appropriate window size for the particular crown size – enhances treetop detection by reducing omission and commission errors (Kathuria et al., 2016; Wulder et al., 2000). However, a major shortcoming of treetop detection approaches is that accuracy is largely dependent upon the structural complexity of forest structure (Falkowski et al., 2008). High accuracy of treetop detection is normally achieved in open canopy, whereas comparatively lower accuracy is achieved in closed multilayer stands (Mongus and Žalik, 2015; Reitberger et al., 2009b; Vauhkonen et al., 2012a). This is due to the fact that trees growing closely together often have overlapping or interlocking crowns, making it difficult to distinguish trees (Falkowski et al., 2008; Heurich, 2008). Although numerous previous studies have highlighted this drawback, few studies directly evaluated how increasing forest complexity influences the accuracy of treetop detection using LiDAR data (Vauhkonen et al., 2012a).

Another potential source of error in treetop detection, when using the local maxima, is formed by the methods used to generate the DSM. There are

two ways to use a DSM for tree detection: as a raster image interpolated from LiDAR points depicting the uppermost layer of the canopy, or as a point cloud. The major advantage of using the point cloud DSM is that all LiDAR returns can be used so that no information is omitted (Duncanson et al., 2014). However, the point cloud-based tree detection techniques are computationally demanding and limited to small areas, and therefore may not be applicable across a larger range of forest types (Duncanson et al., 2014; Hu et al., 2014; Mongus and Žalik, 2015; Wu et al., 2016). A literature review study conducted by Zhen et al. (2016) has reported that 66 % of tree detection approaches are based on using raster DSMs, 20% of the methods are based on LiDAR point cloud, and the remainder are based on combining raster, point cloud and a priori information.

Previous studies have suggested different techniques to generate a raster DSM. For almost two decades, the most popular way to generate a DSM is to interpolate all first LiDAR returns – often via Delaunay triangulation into a Triangulated Irregular Network (TIN) (Axelsson, 1999; Khosravipour et al., 2015; Van Leeuwen et al., 2010; Wu et al., 2016). The reason goes back to 1980s when the earlier small-footprint LiDAR systems were only able to record the distance from the plane to the forest canopy or the distance from the plane to the ground for each pulse (Maclean and Martin, 1984; Nelson et al., 1984). The first return of each pulse always captured the uppermost portion of a forest canopy profile (Nelson et al., 1988). Although over the past decade there have been dramatic improvements in LiDAR technologies to record a higher number of discrete laser returns for each pulse (e.g., up to five or more returns), first returns are still popular when calculating the LiDAR-derived DSMs (Hyyppä et al., 2008; Kathuria et al., 2016; Lim et al., 2003b; Solberg et al., 2006). Nevertheless, any two-dimensional (2D) interpolation of first returns struggles to produce a realistic representation of the canopy surface when there are first returns that have very similar x-y coordinates but very different z values (Axelsson, 1999). When triangulated into a TIN, such variations will form needle-shaped triangles that appear as spikes and result in pixels with unnaturally low values called “pits” when the TIN is rasterized (Khosravipour et al., 2016). These geometric irregularities often

turn the first-return DSM or raster into extremely jagged surfaces, which subsequently reduce the accuracy of treetop detection wherever local maxima methods are used (increasing omission and commission errors) (Ben-Arie et al., 2009; Khosravipour et al., 2014; Persson et al., 2002). Previous studies have reported treetop detection accuracy, based on first-return DSMs, to be in the range of 40–70% for different forest complexity (Pitkänen et al., 2004; Yu et al., 2011) and even below 20% for intermediate and small trees (Kaartinen et al., 2012; Kathuria et al., 2016).

A number of researchers use the benefit of other laser returns by generating a regular grid with each cell recording the maximum laser elevation value within a defined neighborhood of cells (Chen et al., 2006; Holmgren and Persson, 2004; Persson et al., 2002; Popescu, 2007). The assumption here is that in a DSM, the highest value, of any returns, will correspond to the treetop as detected by the local maxima. Researchers have reported that, compared to a first-return DSM, a highest-return DSM using local maxim does improve treetop detection essentially by removing irrelevant first returns with a lower z coordinate that do not represent actual treetops (Chen et al., 2006; Zhen et al., 2016). However, if the chosen neighborhood is too large, the highest-return DSM will overestimate the surface model; and if the chosen neighborhood is too small, empty pixels as well as data pits will appear, especially at lower LiDAR pulse densities (Hollaus et al., 2010; Khosravipour et al., 2016). After a while, Hyyppä et al. (2012) suggest interpolating DSMs using the last return instead of the first or highest return of each pulse, in order to overcome the limitations of the first-return and the highest-return methods in detecting small tree position in complex forests where trees are tightly interlocked. This approach exploits the capability of the small-footprint airborne laser scanner to deeply penetrate between canopy branches and foliage before producing the last return. When trees overlap, the surface model based on last-return DSMs results in a drop in elevation that can be used for separating individual trees.

Recently, Khosravipour et al. (2016) developed the spike-free algorithm for generating higher accuracy DSM rasters for treetop detection. This technique retains the simplicity of raster DSM methods but incorporates

more of the 3D information from the raw point clouds when generating the interpolated surface. The algorithm considers all raw LiDAR returns (i.e., first, second, third, … to last) and systematically prevents the formation of spikes during TIN construction by selectively ignoring those returns that would result in a spike if inserted. Khosravipour et al. (2016) reported that a spike-free DSM significantly improves the accuracy of treetop detection due to its potential to capture more details about the canopy structure which are not usually captured by first-return DSMs. However, to date this has only been tested in a coniferous plantation forest and only compared with a first-return DSM on a LiDAR point cloud with very high pulse density. Therefore, the performance of the spike-free algorithm still unknown for different forest types and LiDAR pulse densities in compare with other previous DSM generation techniques.

The aim of this study is to assess the accuracy of treetop detection using a DSM generated with the spike-free algorithm for different types of forest. The specific objectives of this study are: (a) to evaluate the applicability of spike-free DSMs at different LiDAR pulse densities, and (b) to statistically compare the accuracy of treetop detection achieved with a spike-free DSM to the accuracies achieved with DSMs generated from first-return, highest-return, and last-return LiDAR pulse.

5.2 Materials

5.2.1 Study area and data acquisition

Three different case study areas were selected each with different LiDAR pulse densities, to pursue our objectives covering diverse forest environments. Test site 1 is a temperate plantation forest (Bois Noir, France), test site 2 is a temperate mixed deciduous-coniferous forest (Bavarian Forest National Park, Germany), and test site 3 is a tropical rainforest (Robson Creek, Australia). These three areas are surveyed by 115.85 pulse/m^2, 16.37 pulse/m^2 and 4.63 pulse/m^2, respectively. In the following sections, we describe the characteristics of these case studies and their acquired LiDAR data in more detail.

5.2.1.1 Test site #1

The Bois Noir (black wood) forest is part of the Barcelonnette basin, which is situated in the southern French Alps (44° 23′ N, 6° 45′ E) in the dry intra-Alpine zone, and is characterized by a temperate, Mediterranean climate (annual rainfall 400 - 1400 mm and a mean annual temperature of 7.5ºC) (Flageollet et al., 1999). In the 19th century reforestation was started in the area, enforced by local laws (Arnaud, 1895). The Bois Noir catchment is located on the north-facing slope of the basin with the elevation ranging from 1,400 to 2,380 m above sea level. The catchment is characterized by irregular rugged topography with slope gradients of 10° to 70° (Thiery et al., 2007). The study area is 1.3 km^2 in size and predominantly comprises mountain pine (*Pinus uncinata*) and Scots pine (*Pinus sylvestris*), plus a few larch (*Larix decidua*) and an occasional deciduous tree (*Populus tremula* and *Fraxinus excelsior*).

The field data, which were collected during September 2011 (seven plots) and September 2012 (48 plots), include, tree location and tree stem DBH. Within each plot the DBH of all trees with in diameter larger than 7.0 cm at 1.3 m above the ground was measured using a 60 cm caliper. The position of the individual trees and the center of each plot were recorded using the Leica 1200 Differential GPS System and a total station (see Khosravipour et al. (2014) for more details). In total, 694 trees were measured.

LiDAR data acquisition flights were performed in July 2009. The small footprint full-waveform LiDAR system (RIEGL VQ-480i) utilized by Helimap has been developed specifically for mapping mountainous forested areas (Vallet and Skaloud, 2004). The system was operated at a laser pulse repetition rate of 300-kHz and a scan width of 60° and performed on-line full-waveform analysis to extract up to five discrete returns for each pulse. The survey was flown 250 m above ground level, resulting in a mean footprint diameter of 75 mm on the ground. In order to increase the laser pulse density, the area was covered by seven overlapping flight lines. On average, the pulse density computed from last returns was 115.95 pulse/m^2 and the point density of all returns 164.43 points/m^2.

5.2.1.2 Test site #2

This study area is part of the Bavarian Forest National Park, which is located in south-eastern Germany along the border with the Czech Republic (49° 4′ N, 13° 17′ E). The forest is in a temperate region featuring a cool (mean annual temperature 3 - 6.5°C) and humid (precipitation 1200 - 1850 mm) climate with heavy and long-lasting snow cover in the higher elevations. The area is dominated by rough terrain with the elevation ranging from 600 to 1,453 m above sea level (Heurich et al., 2010). The area mainly encompasses three major forest communities, namely sub-alpine forests dominated by Norway spruce (*Picea abies*) interspersed with a few Mountain ash (*Sorbus aucuparia*); mountain mixed forests dominated by a mixture of Norway spruce, Silver fir (*Abies alba*), European beech (*Fagus sylvatica*), Norway maple (*Acer platanoides*) and Sycamore maple (*Acer pseudoplatanus*); and alluvial spruce forests comprised of Norway spruce, Mountain ash, and Birches (*Betula pendula* and *Betula subescens*) (Cailleret et al., 2014). In the past few years, the forest has hosted several remote sensing-based studies (i.e., LiDAR-based), due to the availability of the field database and feasibility of using various remote sensing systems (Amiri et al., 2016; Heurich and Thoma, 2008; Reitberger et al., 2009b; Yao et al., 2012).

We used field data sets collected for previous research, including Heurich (2008), Yao et al. (2012), and Latifi et al. (2015). For this research 15 sample plots with sizes of between 20 m × 50 m and 50 m × 50 m were selected. The position of each plot and its living trees was precisely measured twice with a Differential GPS System using the post-processing routine. The residual error was less than 5.0 cm (Heurich, 2008). The parameters such as DBH and tree species were collected for all 746 European beech (*Fagus sylvatica*), 579 Norway spruce (*Picea abies*), 12 silver fir (*Abies alba*), 12 Sycamore maple (*Acer pseudoplatanus*), 4 Mountain ash (*Sorbus aucuparia*) and 2 Norway maple (*Acer Platanoides*). The total number of measured trees was 1355.

Full-waveform LiDAR data were available for the entire national park (Latifi et al., 2015), having been collected by Milan Flug GmbH with Riegl LMS-Q680i sensor in three days during July 2012. The survey was flown

650 m above ground level, resulting in a footprint diameter of 32 cm on the ground. The scanning frequency was set to 350-KHz with a scan angle of ± 60° and up to six discrete returns were extracted for each pulse. On average, the pulse density computed from last returns was 16.37 pulse/m^2 and the point density of all returns 33.05 points/m^2.

5.2.1.3 Test site #3

The third case study is located at Robson Creek (17° 7′ S, 145° 37′ E) in Danbulla National Park, which lies within the Wet Tropics World Heritage Area of Queensland, Australia. The forest is representative of upland (400-1000 m) rainforest, boasting highest rates of biodiversity in Australia (Woodgate et al., 2015) and amongst the highest above ground biomass per hectare in the world (Bradford et al., 2014; Murphy et al., 2013). The area consists of complex mesophyll and notophyll vine forest on granite and meta-sediment alluvium (Bradford et al., 2014). The climate in the area is considered seasonal with 61% of the annual rainfall occurring in the months January to March (TERN, 2015). The mean annual rainfall is approximately 2300 mm and the mean annual temperature 19 C° (Woodgate et al., 2012).

The site is locally managed by CSIRO Tropical Forest Research and overseen by James Cook University. The fieldwork and LiDAR data collection was carried out by AusCover field and airborne data collection campaigns of The Australian Terrestrial Ecosystem Research Network (TERN, 2013) between December 2009 and November 2012. All stems of a sample plot with of 500 m × 500 m were identified, mapped, the species noted, and the DBH measured (see Bradford et al. (2014) for more detail). The initial survey of all stems with a DBH ≥ 10 cm recorded 23,416 stems covering 208 species in 128 genera and 53 families, Lauraceae, Rutaceae, Proteacea, Elaeocarpaceae, and Atherspermataceae dominated the list. For this research, however, random sampling determined the position of a central 40 circular subplots (r = 12.6 m) within the initial 25-ha plot. The number of measured trees thus selected was 1711.

Small-footprint full-waveform LiDAR data were acquired in September 2012 over the 25-ha original study site at Robson Creek using a Riegl

LMS-Q560 laser scanner. The provided full-waveform data was subsequently decomposed using Gaussian pulse estimation (Riegl, 2006), which resulted in six returns identified per out going pulse (Wilkes et al., 2015). The flying height was 500 m above the ground, yielding an individual return footprint of approximately 20 cm in diameter. This LiDAR dataset consists of five different flight lines with drastically varying pulse densities. Four of the five flight lines have a low density of 2.03 pulse/m^2 and 2.74 points/m^2. The one very high density flight line that crosses the surveyed area has a density of 6.67 pulse/m^2 and 10.13 points/$m^{2.}$. However, on average, the pulse density computed from last returns of all flight lines in this dataset was 5 pulse/m^2 and the point density of all returns 6.71 points/m^2.

5.3 Methods

Four LiDAR-derived DSM generation techniques are compared in this study, namely interpolation of first returns, of highest returns, of last returns, and of all relevant returns (i.e., spike-free). The input LiDAR point clouds included all returns (i.e., ground and non-ground) with UTM projected *x*-*y* coordinates, ellipsoidal elevation for the z coordinates, and a return numbering to distinguish first from last returns. The pre-processing into DSM rasters was implemented using the LAStools software suite (rapidlasso GmbH, 2016). The output DSM rasters were used as input to a tree detection algorithm that extracted treetop positions with the local maxima approach. The accuracy of the treetop detection was assessed by tree species and by stem diameter (DBH) for each test site using the field data.

5.3.1 LiDAR data processing

The original LiDAR data were stored as tile datasets per project. Besides using the original datasets, we artificially thinned both the original high LiDAR pulse density datasets (Bois Noir forest and Bavarian Forest National Park LiDAR datasets) down to 5.00 pulse/m^2, in order to directly evaluate how increasing forest complexity impacts on the performance of the spike-free algorithm. Unlike other methods that typically create a thinned LiDAR dataset by keeping only every n^{th} return along the time

line, we simulated lower densities by either keeping all returns of a pulse or by removing all returns of a pulse using their GPS timestamp.

However, we should point out that thinning a LiDAR dataset does not exactly simulate a real LiDAR survey. The diameter of the laser beam on the canopy increases with the altitude of the aircraft's flight path due to beam divergence of the laser (Khosravipour et al., 2014; Lim et al., 2008). In an actual survey of lower density LiDAR, fewer laser pulses would sample the ground, each with a wider footprint and thus more likely to interact with the canopy higher-up (Hall et al., 2009).

5.3.2 Generating raster DSMs

To generate the first-return and last-return DSM raster, only all first returns and last returns, respectively, were interpolated through Delaunay triangulation. The resulting triangulations were then rasterized onto a grid with the respective cell size. To generate the highest-return DSM raster, only the highest return within the defined grid cell was used. The resulting subset of returns was again interpolated through Delaunay triangulation, and then rasterized onto a grid with the respective cell size.

The spike-free algorithm, developed by Khosravipour et al. (2016), was used for generating the spike-free DSM raster. This algorithm considers all returns (i.e., first, second, third, … to last) arranged from highest to lowest elevation for insertion into a Constrained Delaunay TIN. However, it only inserts those returns into the TIN that it deems "relevant". There are two user-defined parameters that affect which returns are inserted: (a) freeze distance and (b) the insertion buffer. Freeze distance prevents the formation of spikes in the incrementally constructed Constrained Delaunay TIN by "freezing" triangles with three edges shorter than this specified distance and by ignoring returns that fall onto "frozen triangle". The insertion buffer prevents the generating of artifacts due to premature freezing of triangles during the TIN construction by delaying the freezing process. The freeze distance is defined based on the 99^{th} percentile of the frequency of triangles' edge lengths, which captures the range of actual pulse spacing within the surveyed area. Therefore, the calculated freeze distances are 0.45 m, 0.70 m and 1.60 m ,respectively, for the Bois Noir

forest, Bavarian Forest National Park and Robson Creek LiDAR data sets. For the thinned datasets, the freeze size of 1.35 and 1.25 m were determined for the Bois Noir forest and Bavarian Forest National Park, respectively. The insertion buffer should not be larger than the minimum vertical distance between two returns of the same pulse. The smallest possible distance between subsequent returns was defined based on the scanning hardware. For this research, we chose an insertion buffer size of 0.5 m, which is a reasonable size for Riegl scanners (Khosravipour et al., 2016). The algorithm results in a spike-free TIN that interpolates all relevant returns, and is rasterized onto a grid with the respective cell size.

The cell size for the DSM rasters should not be much smaller than the mean LiDAR pulse spacing (Chow and Hodgson, 2009). This cell size determines the smallest detectable object (i.e., a tree) as expressed by the Nyquist sampling theory (i.e., the minimum object of interest cannot be smaller than two cells) (Nygren et al., 1993). We selected a cell size within a 0.15 m spatial resolution (and 0.25 m for the thinned datasets) for the Bois Noir forest and Bavarian Forest National Park LiDAR data sets; and a 0.25 m spatial resolution for Robson Creek based on their LiDAR pulse spacing.

5.3.3 Individual tree detection

A method based on morphological opening and reconstruction was applied to all four generated DSMs. Morphological opening is a well-known image-processing method for separating different objects (Vincent, 1993), while preserving their structure in images (Wang et al., 2004). Morphological opening is achieved by two sequential moving window operations (i.e., erosion and dilation) with the Structural Element (SE) as a template (Serra, 1982). The shape and size of the structural element are commonly based on the shape and size of the object of interest (for example, a disk shape for tree crown objects). However, if the selected SE is too large, more parts of the crowns will be removed, while if the SE selected is too small, some branches might be mistaken for individual trees. The efficient approach is to set this parameter empirically for each local area, in order to deal with the natural variations in crown size (Jing et al., 2012b). We found empirically that a combination of flat disks with

a diameter of 5 and 7 pixels in size provided appropriate structural elements for detecting treetops with the natural variation in crown size in our case studies. The opening operations removed *foreground* objects (i.e., treetops) that were smaller than the defined SE in the DSM raster. The output was an *opened image*. Next, the morphological reconstruction, an efficient method for extracting regional maxima (Vincent, 1993), was implemented. To extract the regional maxima, the morphological reconstruction method selected the previously generated opened image as a *marker* and selected the original DSM image as a *mask* image in order to retrieve the shape of tree crown boundaries. The result is a *reconstructed* image. Subsequently, the reconstructed image was subtracted from the original DSM in order to isolate the regional maxima that had been removed by the opening operation as *foreground* objects. Finally, the local maxima of each regional maxima component were extracted from the image. These local maxima form the estimated treetop points (x, y and z).

5.3.3.1 Accuracy assessment of individual tree detection

An evaluation of the accuracy of treetop detection was carried out by calculating the Kappa coefficient (Cohen, 1960) using an error matrix. Accuracy assessment was done by associating the detected local maxima (laser measured trees) with the actual field measured trees within a defined tree radius boundary. Each of the local maxima was associated with the closest field measured tree within a radius of 60% of the mean distance (i.e., the distance from each tree to its closest neighbor divided by the number of trees in each plot) (Heurich, 2008). If more than one local maximum was detected within the boundary, the closest one was considered to be a correctly detected tree, and the others were then defined as commission errors. If at the end of the process there were field measured trees without an associated local maximum, these trees were considered to be omission errors.

In order to create the error matrix, we converted the local maxima information into a classified grid raster representing four classes inside the defined tree boundaries (Figure 1). The cells that correspond correctly to LiDAR-detected trees (i.e. treetops) were classified as True Positive (TP); the cells that correspond to falsely detected trees (i.e. commission errors)

were classified as False Positive (FP); the cells that correspond to omission errors were classified as False Negative (FN); and the remaining cells, those correctly not assigned to any local maxima, were considered to be True Negative (TN). In order to avoid an overestimation of TN, the cell size of the classified grid was selected based on the average radius boundary in each case study.

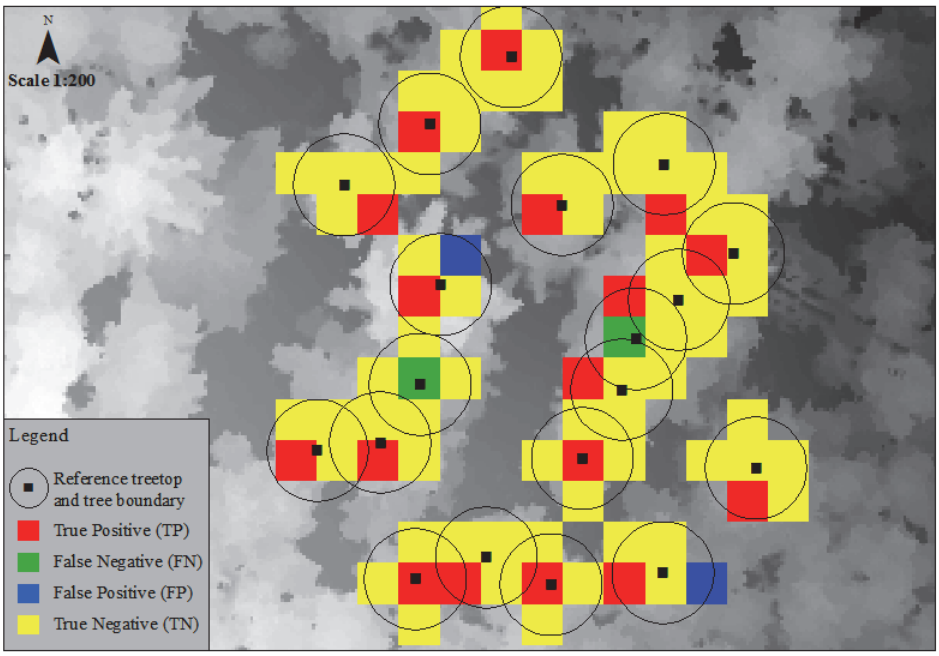

Figure 5.1: Visual representation of the classified grid, illustrating correctly detected trees, omission errors, and commission errors of the DSM generated by the spike-free DSM (Bois Noir, France).

Once Cohen's Kappa is calculated, the pairwise comparison of the Z-statistic test (Congalton and Green, 1999) was performed to determine if the error matrix of the spike-free method is significantly different from the other methods. The Z-statistic test for testing if two independent error matrices are significantly different is expressed by:

$$Z = \frac{\left|\hat{K}_{SF} - \hat{K}_{Fr}\right|}{\sqrt{\widehat{var}\left(\hat{K}_{SF}\right) + \widehat{var}\left(\hat{K}_{Fr}\right)}}$$

where $\widehat{K}_{SF}$ and $\widehat{K}_{Fr}$ denote the estimates of the Kappa statistic for the error matrix of the spike-free method and the first-return method, respectively; and $\widehat{var}(\widehat{K}_{SF})$ and $\widehat{var}(\widehat{K}_{Fr})$ are the corresponding estimates of the variance as computed from the appropriate equations proposed by Fleiss et al. (1969). Given the null hypothesis H_0: $\widehat{K}_{SF} - \widehat{K}_{Fr} = 0$, the alternative H_1: $\widehat{K}_{SF} - \widehat{K}_{Fr} \neq 0$ is rejected if $Z \geq z_{a/2}$ (e.g. at the 99% confidence interval the value is 2.575). Note that $\widehat{K}_{Fr}$ may be replaced by estimates of the Kappa statistic of the other methods.

Based on the DBH distribution at each site, the range of DBH was classified into three classes: DBH less than 20 cm, DBH from 20 to 40 cm, and DBH greater than 40 cm. This allowed us to assess and compare the accuracy of the detection of various ranges of DBH using the four DSM generating methods.

5.4 Results

The number of extracted individual tree species, the Kappa (K) and the Z-Statistic values for the Bois Noir forest, the Bavarian Forest National Park and for Robson Creek, using different LiDAR-derived DSMs, are shown in Table 5.1 to 5.6. The Kappa coefficients ranging from 0.28 to 0.85 were obtained. The highest accuracy (Kappa = 0.85) was obtained using the spike-free algorithm within the Bois Noir forest (France), while the lowest accuracy (Kappa = 0.28) was obtained using the highest-return DSM generation method within Robson Creek (Australia). For both coniferous and broadleaf tree species, the spike-free method outperformed the other methods in all case studies (Table 5.1 to Table 5.3). Interestingly, regardless of which DSM generation method was used, the accuracy rate was consistently reduced based on LiDAR pulse density as well as forest complexity, as can be seen in Table 5.1 and 5.2. The result showed that all DSM generation techniques performed best with dense LiDAR pulse density.

Table 5.1: Treetop detection results for all DSMs derived from the original high pulse density (116 pulse/m^2) and the thinned dataset (5 pulse/m^2) in the Bois Noir forest.

Bois Noir forest (France)																**Original dataset**			
Field-measured trees		First-return DSM				Highest-return DSM				Last-return DSM				Spike free DSM			
n	Species	correct n	omission n	commission n	κ	correct n	omission n	commission n	κ	correct n	omission n	commission n	κ	correct n	omission n	commission n	κ
33	Deciduous	24	9	3	0.75	25	8	12	0.62	16	17	1	0.57	31	2	10	0.78
29	Larch (*Larix decidua*)	26	3	4	0.86	28	1	8	0.83	24	5	4	0.81	28	1	6	0.86
325	scots pine (*pinus sylvestris*)	245	80	17	0.78	277	48	34	0.82	190	135	14	0.64	280	45	37	0.82
307	mountain pine *(pinus uncinata)*	244	63	27	0.73	272	35	34	0.79	218	89	31	0.63	285	22	19	0.88
694	Total	539	155	51	0.77	602	92	88	0.81	448	246	50	0.66	624	70	72	0.85
Bois Noir forest (France)																**Thinned dataset**	
33	Deciduous	14	19	1	0.51	13	20	0	0.49	15	18	3	0.50	19	14	0	0.67
29	Larch (*Larix decidua*)	26	3	0	0.93	22	7	1	0.81	21	8	0	0.81	24	5	0	0.88
325	scots pine (*pinus sylvestris*)	203	122	3	0.69	167	158	3	0.59	174	151	8	0.60	213	112	0	0.73
307	mountain pine *(pinus uncinata)*	173	134	5	0.56	143	164	5	0.46	149	158	9	0.47	173	134	0	0.58
694	Total	416	278	9	0.65	345	349	9	0.56	359	335	20	0.56	429	265	0	0.68

Table 5.2: Treetop detection results for all DSMs derived from the original high pulse density (16 pulse/m^2) and the thinned dataset (5 pulse/m^2) in the Bavarian Forest National Park.

Bavarian National Park (Germany)																**Original dataset**
Field-measured trees			First-return DSM				Highest-return DSM				Last-return DSM				Spike free DSM			
n		Species	correct n	omission n	commission n	K	correct n	omission n	commission n	K	correct n	omission n	commission n	K	correct n	omission n	commission n	K
746	Deciduous	European beech (*Fagus sylvatica*)	463	283	146		458	288	143		519	227	227		525	221	157	
18	Deciduous	Other deciduous*	7	11			10	8	3		10	8	3		12	6	2	
764	Deciduous	Total	470	294	146	0.53	468	296	146	0.53	529	235	230	0.53	537	227	159	0.60
579	Coniferous	Norway spruce (*Picea abies*)	386	193	70		366	213	58		394	185	129		396	183	20	
12	Coniferous	silver fir (*Abies alba*)	9	3	2		9	3			9	3	6		10	2	2	
591	Coniferous	Total	395	196	72	0.57	375	216	58	0.56	403	188	135	0.49	406	185	22	0.67
1355		Total	865	490	218	0.55	843	512	204	0.55	932	423	365	0.52	943	412	181	0.63
Bavarian National Park (Germany)																**Thinned dataset**		
746	Deciduous	European beech (*Fagus sylvatica*)	301	445	20		281	465	25		301	445	35		293	453	10	
18	Deciduous	Other deciduous*	5	13			6	12	1		8	10			10	8		
764	Deciduous	Total	306	458	20	0.44	287	477	26	0.41	309	455	35	0.43	303	461	10	0.44
579	Coniferous	Norway spruce (*Picea abies*)	313	266	16		296	283	22		317	262	38		326	253	1	
12	Coniferous	silver fir (*Abies alba*)	6	6			8	4			4	8	2		6	6		
591	Coniferous	Total	319	272	16	0.53	304	287	22	0.50	321	270	40	0.50	332	259	1	0.57
1355		Total	625	730	36	0.48	591	764	48	0.45	630	725	75	0.46	635	720	11	0.51

*: a few Sycamore maple (*Acer pseudoplatanus*), Norway maple (*Acer platanoides*) and Mountain ash (*Sorbus aucuparia*).

Table 5.3: Treetop detection results for all DSMs derived from the original pulse density (in average 5 pulse/m^2) and in the Robson creek.

Robson Creek (Australia)*																**Original dataset**
Field-measured trees		First-return DSM				Highest-return DSM				Last-return DSM				Spike free DSM			
n	Species	correct n	omission n	commission n	K	correct n	omission n	commission n	K	correct n	omission n	commission n	K	correct n	omission n	commission n	K
104	Atherspermataceae	53	51	35	0.18	61	43	35	0.26	56	48	29	0	59	45	10	0.47
192	Elaeocarpaceae	112	80	63	0.26	108	84	55	0.28	111	81	57	0.28	103	89	11	0.48
337	Lauraceae	183	154	75	0.34	210	127	29	0.55	193	144	96	0.31	182	155	25	0.48
266	Proteaceae	156	110	74	0.33	174	92	122	0.22	153	113	77	0.30	124	142	21	0.40
84	Rhamnaceae	46	38	23	0.30	51	33	26	0.33	51	33	19	0.41	41	43	7	0.42
264	Rutaceae	159	105	81	0.30	176	88	109	0.26	180	84	113	0.26	159	105	24	0.51
1668	Total	943	725	468	0.29	1034	634	578	0.28	983	685	525	0.29	875	793	131	0.45

**this table presents only the most dominant species' families at Robson creek.*

The pairwise comparisons using the Z statistics for the spike-free method and other DSM generated methods is presented in Table 5.4. The test indicated that the spike-free algorithm was significantly better than the first-return (3.96) and last-return (8.56) methods using the high pulse density for detecting treetops at Bois Noir forest (France). However, the Z-Statistic comparing the spike-free and highest-return DSMs (2.23) was slightly less than the critical Z value (2.57) for an alpha 0.01, thus indicating no significant difference between these methods for detecting treetops in this forest type. The pairwise test revealed that there was a significant difference between using the spike-free and all three other methods in the Bavarian National Park (Germany) using high pulse density, but not significant when using the thinned dataset (5 pulse/m^2).

Table 5.4: Results of the Kappa analysis, comparing between the spike-free, the first-return, the highest-return, and last-return methods using both the original dataset and the thinned datasets.

Bois Noir forest				**France**
	Original dataset		**Thinned dataset**	
Comparison	Z Statistic	Result*	Z Statistic	Result
Spike-free vs. First-return	3.96	S**	1.02	NS
Spike-free vs. Highest-return	2.23	NS	4.45	S
Spike-free vs. Last-return	8.56	S	4.19	S
Bavarian National Park				**Germany**
Spike-free vs. First-return	3.65	S	0.97	NS
Spike-free vs. Highest-return	3.99	S	2.36	NS
Spike-free vs. Last-return	5.41	S	1.81	NS
Robson Creek				**Australia**
Spike-free vs. First-return	6.97	S	–	
Spike-free vs. Highest-return	7.39	S	–	
Spike-free vs. Last-return	7.37	S	–	

**: at the 99% confidence level interval the value is 2.575*
***: Significant*

Tree detection accuracy was also assessed for a range of DBH classes using the original datasets. At the Bois Noir forest, the spike-free method outperformed the other techniques for DBHs of less than 40 cm (Table 5.5). The Z test indicated that there was a statistically significant difference between using the spike-free and the first- and last-return methods in detecting trees with a DBH of less than 20 cm as well as a DBH between 20-40 cm (Table 5.6). However, for a DBH of more than 40 cm, all DSM

techniques performed well (Table 5.5 and 5.6). For the Bavarian National Park and Robson Creek sites the spike-free method's kappa values were not as high as the results show at the Bois Noir site regarding detecting trees, but the spike-free method did consistently outperform the other techniques in all DBH ranges (Table 5.5 and 5.6).

Table 5.5: Tree detection results for three DBH ranges for the first-return, highest-return, last-return and spike-free method.

Bois Noir forest																	**France**
Field-measured trees		First-return DSM				Highest-return DSM				Last-return DSM				Spike free DSM			
n	Portion of DBH range (cm)	correct n	omission n	commission n	κ	correct n	omission n	commission n	κ	correct n	omission n	commission n	κ	correct n	omission n	commission n	κ
258	< 20	188	70	22	0.69	214	44	40	0.72	156	102	17	0.59	224	34	29	0.79
397	20-40	317	80	27	0.80	354	43	40	0.85	262	135	30	0.68	368	29	37	0.88
39	> 40	34	5	2	0.88	34	5	8	0.80	30	9	3	0.80	32	7	6	0.79
Bavarian National Park																	**Germany**
477	< 20	220	257	60	0.35	243	234	55	0.41	268	209	99	0.37	244	233	47	0.42
451	20-40	299	152	56	0.57	293	158	77	0.52	320	131	114	0.51	332	119	56	0.64
427	> 40	346	81	102	0.70	307	120	72	0.67	344	83	152	0.63	367	60	78	0.77
Robson Creek																	**Australia**
1060	< 20	583	477	263	0.31	632	428	345	0.28	595	465	327	0.26	519	541	74	0.42
463	20-40	285	178	162	0.26	316	147	186	0.28	291	172	166	0.27	270	193	43	0.49
145	> 40	75	70	43	0.29	86	59	47	0.34	97	48	32	0.50	86	59	14	0.54

Table 5.6: Results of the Kappa analysis, comparing between the spike-free method and the first-return, highest-return, and last-return methods.

Bois Noir forest			**France**
Comparison	Portion of DBH range (cm)	Z Statistic	Result
Spike-free vs. First-return	< 20	2.66	S
	20-40	3.51	S
	> 40	-1.34	NS
Spike-free vs. Highest-return	< 20	1.84	NS
	20-40	1.48	NS
	> 40	-0.10	NS
Spike-free vs. Last-return	< 20	4.85	S
	20-40	7.42	S
	> 40	-0.08	NS
Bavarian National Par			**Germany**
Spike-free vs. First-return	< 20	1.83	NS
	20-40	1.95	NS
	> 40	2.65	S
Spike-free vs. Highest-return	< 20	0.44	NS
	20-40	3.37	S
	> 40	3.59	S
Spike-free vs. Last-return	< 20	1.30	NS
	20-40	3.75	S
	> 40	5.07	S
Robson Creek			**Australia**
Spike-free vs. First-return	< 20	4.06	S
	20-40	5.28	S
	> 40	3.38	S
Spike-free vs. Highest-return	< 20	5.10	S
	20-40	4.95	S
	> 40	2.71	S
Spike-free vs. Last-return	< 20	5.71	S
	20-40	5.19	S
	> 40	0.49	NS

5.5 Discussion

The spike-free algorithm and three other conventional DSM generation techniques for detecting individual trees from LiDAR data were compared and evaluated across multiple forest types and different LiDAR pulse densities. Although our results show that the use of a spike-free DSM can improve the accuracy of treetop detection in compare with other approaches, the accuracy strongly depends on the LiDAR pulse density and forest complexity.

5.5.1 Effect of forest complexity

In order to directly evaluate how increasing forest complexity influences the accuracy of tree detection using the spike-free algorithm, we artificially thinned both the original high pulse density LiDAR datasets (the Bois Noir forest and Bavarian Forest National Park LiDAR datasets) to 5 pulse/m^2. The best detection result was obtained within the Bois Noir forest (France) which consists of coniferous plantation trees with only a small amount of understory density (original data = 0.85 $_{kappa}$, thinned data = 0.68 $_{kappa}$). The lowest detection result using the spike-free DSM was obtained at Robson Creek, Australia (original data = 0.45 $_{kappa}$), an area that consists of mixed multi-layered broad-leaved trees scanned with drastically varying low pulse densities. These results reveal that it is relatively "easy" to detect local maxima of conifers that have a conical crown shape with a distinct apex (e.g., mountain pine trees in the Bois Noir forest). In contrast, it is relatively difficult to determine broadleaved trees that have a rounded and irregular crown shape (e.g., European beech in the Bavarian national park) or/and have distinct layers of separating crown, which heavily overlap (e.g., Lauraceae species at Robson Creek). Although the spike-free method outperformed the other techniques at the Bavarian National Park and particularly at Robson Creek, their overall results were low. These experiments were consistent with those reported in the literature in that the accuracy of treetop detection varies from study to study based on the structural complexity of the forest stand. For example, Heurich and Thoma (2008) and Popescu and Wynne (2004) noted that the rate of detection is much greater for conifers than for deciduous trees. Conifers can usually be separated easily from neighboring trees, while deciduous trees are often

tightly interlocked, especially in homogeneous forests. Vauhkonen et al. (2012a) have reported a treetop detection rate of 48% to 60 % for different types of forest: boreal forest in Norway and Sweden, coniferous and broadleaved forest in Germany, and tropical pulpwood plantations in Brazil.

The result of our treetop detection experiments using the first-return, highest-return and last-return DSMs is in agreement with the results of previous studies. They have also reported treetop detection accuracies using first-return DSMs in the range of 40–70% for different forest types (Kaartinen et al., 2012; Kathuria et al., 2016; Yu et al., 2011). Heurich (2008) reported a detection accuracy of 45% in the Bavarian National Park and Véga and Durrieu (2011) achieved a 70% overall accuracy for the southern French Alps using the highest-return DSM. However, using the spike-free DSM we achieved a much better treetop detection rate even if the study areas scanned with low pulse density. Our findings demonstrate that the commission error is very high using all other types of DSM for deciduous trees, particularly in the tropical forest with tree crowns heavily overlapping. Eysn et al. (2015) and Kaartinen et al. (2012) found that the highest-return DSMs generated a high rate of commission error for multi-layered mixed forests that consist of complex crown shapes (e.g., deciduous trees). This is principally because deciduous tree crowns have a wide range of sizes with irregular shapes and their branches and sub-crowns resemble small trees that cause the false detections (Duncanson et al., 2014; Jing et al., 2012a; Kato et al., 2009; Popescu and Wynne, 2004). Hyyppä et al. (2012) stated that last-return DSM is prone to create too many commission errors when there are gaps within individual tree crown and the area is covered by bushes. The remarkable result of this study is that the rate of commission error is significantly lower for both coniferous and broadleaved trees using the spike-free DSM. This is because the spike-free algorithm systematically prevents formation of spikes during TIN construction by ignoring any return that would result in increasing commission error if inserted.

5.5.2 Effect of LiDAR pulse density

Our results show the strong effect of LiDAR pulse density on the accuracy of treetop detection using the spike-free DSM, especially at complex forests. Previous studies have claimed that the success in accurately detecting local maxima relies on sufficiently high density of laser pulse footprints (Holmgren and Persson, 2004). Our spike-free tree detection results of thinned low LiDAR pulse density datasets showed that the use of a higher density of laser pulses increases the chance to sample the treetops and consequently reduces the omission errors, especially for dense stands (Lefsky et al., 2002; White et al., 2016).

The current implementation of the spike-free algorithm is sensitive to variations in the actual spacing between laser pulses. This is because the spike-free algorithm relies on a "single" freeze distance for the entire data set, implicitly assuming a more or less uniform distance between all neighboring laser pulses. Wherever we use a freeze distance larger than the actual pulse spacing, triangles are 'frozen' too soon, details, particularly small trees and trees in dense stands with a narrow spacing, are lost, and the likelihood of neighboring crowns being joined together increases. This leads to an increased omission error. Wherever we use a freeze distance smaller than the actual pulse spacing, triangles remain "unfrozen" for too long so that "spikes" can reappear in the DSM and cause commission errors. The Robson Creek data set was covered by several various pulse density flight lines (see the section 2.1.3). The higher number of omission errors in the Robson Creek data set can be explained by us using the 99th percentile of the edge length of a last-return triangulation as fixed value for the freeze distance. These results agree with the observation of Khosravipour et al. (2016) that a fixed freeze distance is not optimal when the pulse spacing varies across the data set. The freeze distance needs to be adapted locally to the observed pulse spacing to improve treetop detection using low pulse density with irregular distribution.

5.6 Conclusion

In this study the performance of a DSM generated from the spike-free algorithm was validated to improve treetop detection. The findings show that the spike-free DSM method improves tree detection across a range of spatial and temporal scales for different forest types/biomes, including coniferous, broadleaf deciduous and broadleaf evergreen. The results indicate the impact of both forest complexity and pulse density on the performance of the spike-free algorithm. The best performance of the algorithm achieved within a coniferous plantation (Bois Noir forest, France) scanned with high point density.

Chapter 6

Synthesis

6.1 Introduction

Individual tree detection (ITD) using LiDAR data plays an increasingly significant role in efficiently and accurately monitoring and managing forest activities, such as ecosystem modelling and biodiversity assessment (White et al., 2016; Wu et al., 2016). The initial and important step in detecting individual trees using LiDAR data relies on the generation of Digital Surface Models (DSMs) or their normalized Digital Surface Models (nDSMs) describing the geometry of the uppermost layer of the canopy. The ITD approaches identify local maxima using the geometric information of DSMs. The main challenge faced in ITD approaches is to identify only "true" treetops. How successful this identification is, depends strongly on the quality of the DSM derived from the LiDAR data.

The quality of the LiDAR derived DSMs depends on several factors: the quality of the acquired LiDAR data, data pre-processing and post-processing, as well as forest conditions (Kaartinen et al., 2012). For example, the use of a higher density of laser pulse footprints improves the chance of the laser hitting the treetops (Hyyppä et al., 2008; Lefsky et al., 2002), and the use of more sophisticated DSM generating techniques boosts the correctness of subsequent treetop identification by reducing commission and omission errors (Chen et al., 2006; Kaartinen et al., 2012; Vauhkonen et al., 2012a). A number of studies have indicated that the various forest conditions (e.g., crown size, age, tree species, site type and steep terrain) can significantly influence intermediate LiDAR derivatives and thereby the performance of ITD approaches (Falkowski et al., 2008; Pitkänen et al., 2004; Popescu and Wynne, 2004; Vauhkonen et al., 2012a; Yu et al., 2011).

The major focus of this thesis has been to develop a new approach in order to generate a high-quality LiDAR-derived DSM that is able to improve the accuracy of tree detection across multiple forest types and LiDAR point densities. Chapter 2 discussed the development of a new pit-free algorithm that efficiently removes "pits" in the Canopy Height Models (CHM), but for height-normalized LiDAR data only. Chapter 3 quantified the effect of slope on the accuracy of treetop detection due to the height-normalization step used with a CHM. In Chapter 4 the main objective was the

development of a novel spike-free algorithm that can remove "pits" in the DSM directly, without needing to normalize the LiDAR elevations. Chapter 5 evaluated the applicability of these spike-free DSMs for different forest types and LiDAR point densities.

6.2 Generating pit-free Canopy Height Models from airborne LiDAR

A LiDAR-derived Canopy Height Model (CHM) or a normalized Digital Surfaced Model (nDSM) has typically been used for ITD approaches. A CHM represents the relative canopy height above the ground. However, it is often generated by interpolating the first return LiDAR points. This often leads to height irregularities in the CHM as first returns may also be generated far below the top of the canopy. This happens either when the laser beam is able to penetrate deeply through canopy branches and foliage before producing a first return or when the laser beam glances under the vegetation when scanning at highly off-nadir scan angles. This disruptive influence of the resulting "pits" forms a challenging problem as it can considerably reduce the accuracy of single tree detection.

Chapter 2 proposed a new algorithm that generates a pit-free CHM raster by using a set of partial CHM rasters to close those pits. The algorithm operated robustly on both a high and a low point density LiDAR dataset. The pit-free CHMs derived from both LiDAR datasets were evaluated by visual comparison with the first-return CHMs smoothed with a 5×5 Gaussian filter. Figure 6.1 details pit-free CHMs side by side with Gaussian smoothed CHMs, with their associated x-axis histograms. The pit-free algorithm successfully removed all pits (small dark squares) within tree crowns that were not completely removed by the Gaussian filter. As can be seen, the Gaussian filter over-smoothed the CHMs – especially the CHM derived from the low-density LiDAR dataset – leading to an underestimation of the canopy height. In contrast, the pit-free algorithm removed pits from the CHM without altering the original structure of the tree crowns. The profiles depicted in Figure 6.1illustrate that the overall morphological structure of canopy vegetation is preserved well in the pit-free CHM, especially for the high-density LiDAR dataset.

Chapter 2 also experimentally validated that using the pit-free CHMs generated by the pit-free algorithm statistically significantly improved the accuracy of tree detection compared to using the Gaussian-smoothed first-return CHMs. The pit-free algorithm removed pits from the CHM without smoothing and altering the value of all other pixels and thus achieved high accuracy in tree detection for both high-point density (74%) and low-point density (67%) LiDAR data. The Gaussian filter smoothed the entire CHM, thereby affecting its structure everywhere and thus achieving significant lower accuracy in detecting trees for both high-point density (70%) and low-point density (35%) LiDAR data – especially regarding small trees.

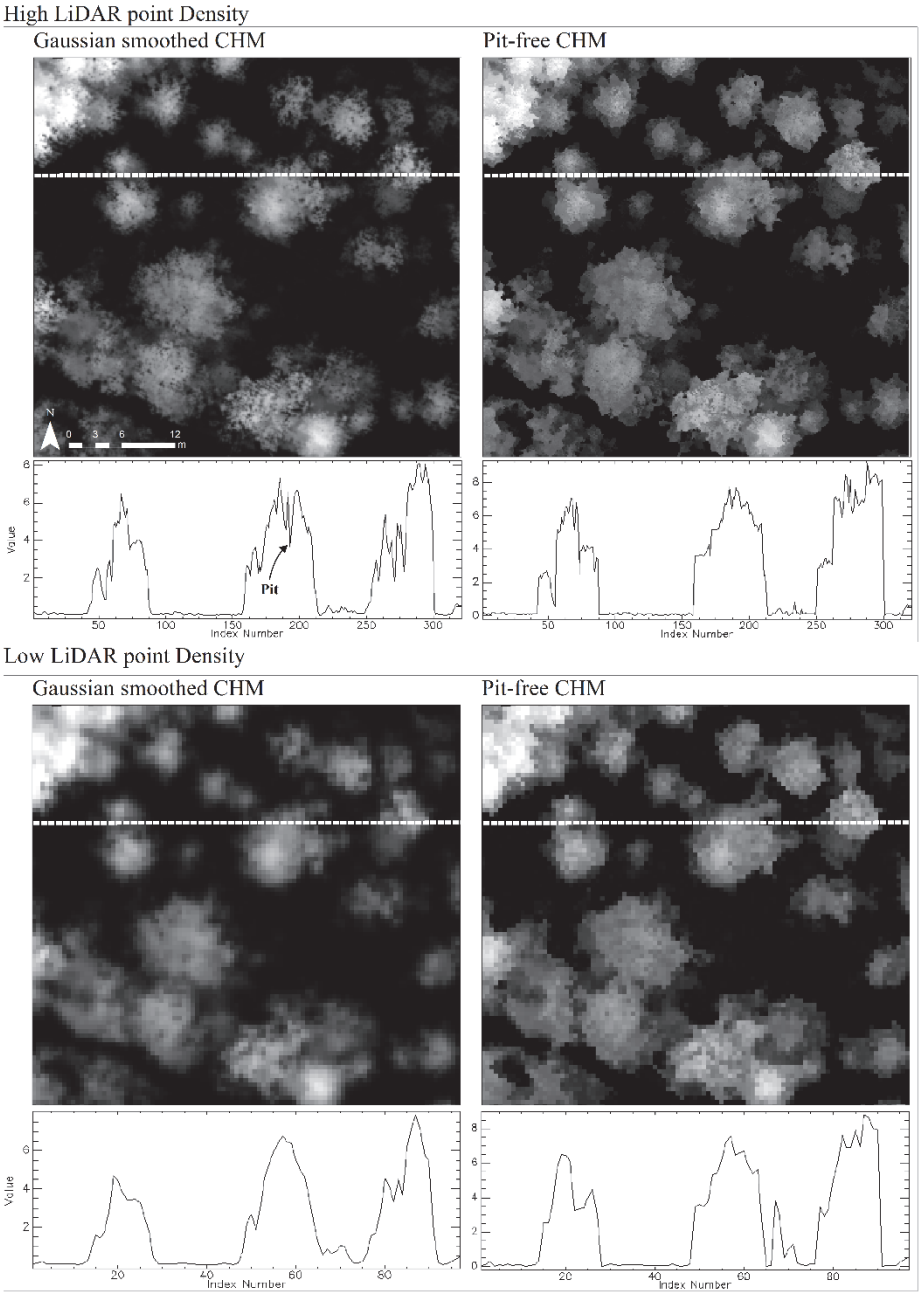

Figure 6.1: A visual comparison of the x-axis profiles of pit-free CHMs with those of smoothed first-return CHMs derived from both high- and low-density LiDAR data. The x-axis represents pixel values from the white dashed line in the corresponding CHMs.

6.3 Effect of slope on tree detection in a CHM

Complex forest terrain presents a challenging problem as it distorts the structure of the vegetation in a CHM during the height normalization step, thus possibly reducing the accuracy of tree detection (Vega et al., 2014). On steep slopes, the raw elevation values located on either the downhill or uphill part of a tree crown are height-normalized with parts of the DSM that may be much lower or higher than the tree stem base, respectively (fig. 6.2). Therefore, in the CHM, the downhill part of the crown will "rise" while the uphill part will "sink", causing the entire tree crown to be systematically distorted (Figure 6.2).

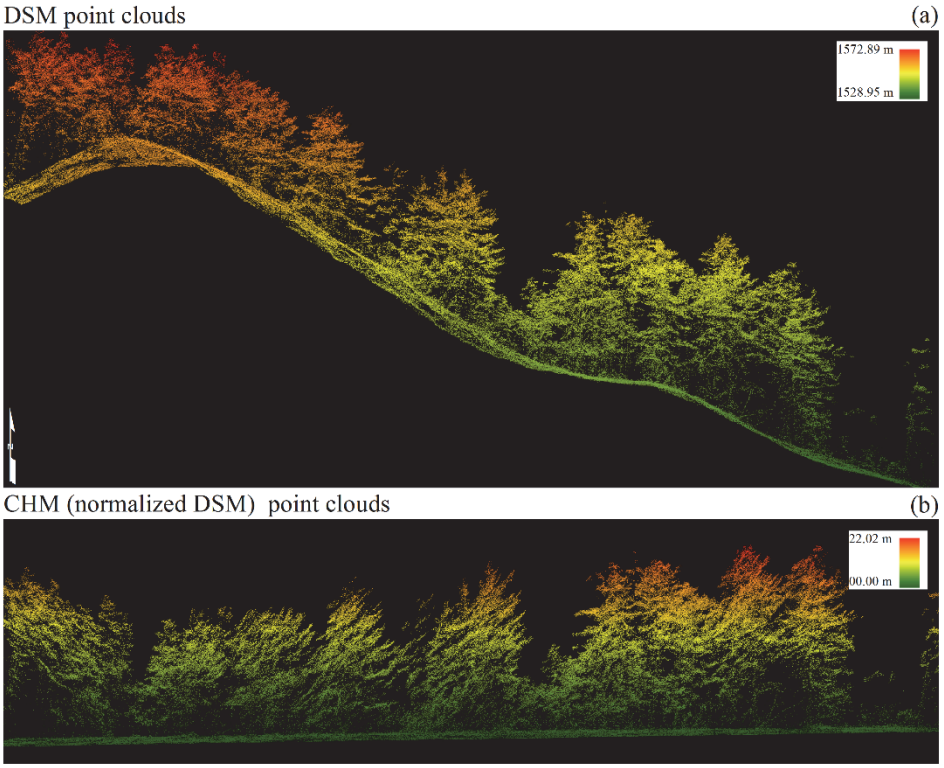

Figure 6.2: The effect of slope on LiDAR point clouds during the normalization step: (a) before normalization and (b) after normalization.

Chapter 3 theoretically and experimentally quantified the effect of slope on the accuracy of tree detection. In ITD approaches, the "rising" branch overhanging lower terrain in the downhill part can turn into a "false" local

maximum that differs from the "true" treetop (Fig 6.3). The theoretical model captured the systematic horizontal displacement of treetops that causes tree height to be systematically displaced as a function of terrain slope and crown shape. For example, if we assume a tree (Fig. 6.3) located on a 40-degree slope surface, with an idealized spherical crown with a radius of 3.5 m, the detected local maximum has a horizontal positional displacement error of 2.20 m and thus the tree height will be overestimated by 1.06 m (vertical displacement error) on a CHM.

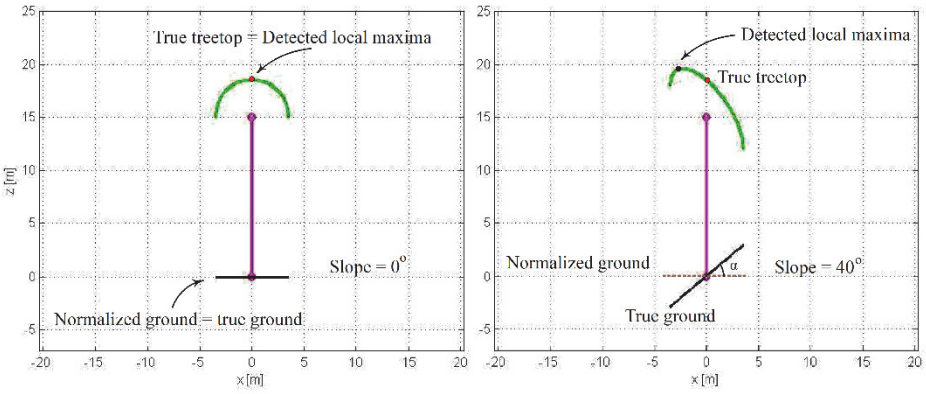

Figure 6.3: Schematic diagram of an idealized spherical crown shape distorted by a slope gradient of 40 degrees during the normalization step.

However, an idealized spherical crown in a theoretical model differs from crowns in the field. The experimental results demonstrated that the effect of CHM distortion on treetop displacement strongly depends on the particular tree crown shape, which is largely determined by its species. For example, the influence of the systematic error showed only significance for Scots pine trees, which have an irregular crown shape with a weak apical dominance, but not for mountain pine trees, which have a narrow conical crown with a distinct apex.

On the basis of our results, Chapter 3 recommended using raw elevation values (i.e., the un-normalized DSM) for detecting the location of treetops and performing the normalization step for computing the height of the trees afterwards in order to circumvent the distorting effect the steep slopes have on crown structure in a CHM, especially in heterogeneous forests

consisting of multiple species. The next step is an appropriate method for generating a high-quality LiDAR-derived DSM for ITD approaches.

6.4 Generating spike-free DSMs from LiDAR data

As mentioned in the Chapter 2, a DSM (or an nDSM/CHM) raster has typically been generated from LiDAR by interpolating all first returns. This method cannot faithfully represent the uppermost layer of the canopy forest for ITD approaches, as first returns may also be generated far below the top canopy (see 6.2). Such first returns may cause large height variations – called *pits* in the raster and *spikes* in the TIN – within single tree crowns, impeding the detection of individual trees. In Chapter 2, we presented a pit-free algorithm able to generate a pit-free CHM (or normalized DSM). However, the pit-free algorithm is impractical for generating a pit-free DSM raster due to the excessive number of partial DSMs that would be required, especially in steep and complex forested terrain. Moreover, the pit-free CHM algorithm used only first returns, potentially missing canopy details captured by second, third, or fourth returns.

Chapter 4 presented a novel "spike-free" algorithm that can generate a DSM at the highest resolution supported by LiDAR in the form of a spike-free TIN. The algorithm considers all LiDAR returns and systematically prevents the formation of spikes during TIN construction by selectively ignoring returns for which insertion will result in a spike. Although the pit-free algorithm (as presented in Chapter 2) is already able to remove pits efficiently and showed the potential to improve the detection of trees, the spike-free DSM generated from all relevant returns can capture more details (especially in low vegetation) than the corresponding pit-free CHM generated from only the first returns (Figure 6.4).

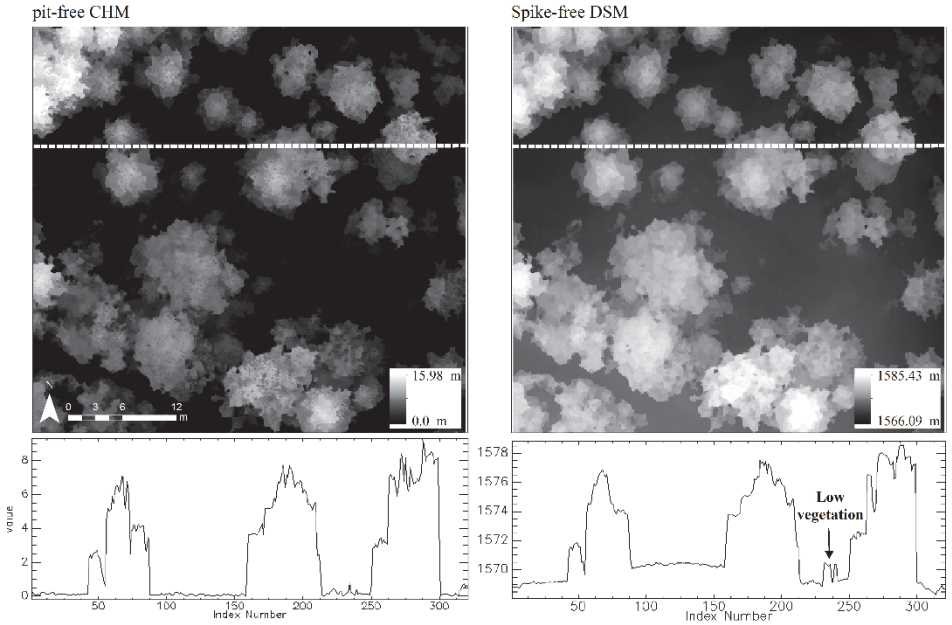

Figure 6.4: Illustrating the spike-free DSM side by side with its corresponding pit-free CHM. The x-axis presents pixel values from the white dashed line in the rasters.

By considering the contribution of all relevant returns, the spike-free algorithm significantly improved the accuracy of tree detection compared to the first-return DSM. Chapter 4 demonstrated a further improvement on the result of Chapter 2, which with a pit-free CHM for detecting trees, especially small trees (Table 6.1).

Table 6.1: Proportion of correctly detected trees for three DBH ranges for the first-return DSM, the pit-free CHM and the spike-free DSM.

Portion of DBH range (cm)	All (n= 694)		
	< 20 (n = 258)	20-40 (n = 397)	> 40 (n = 39)
First-return DSM	150 (58.1%)	299 (75.3 %)	33 (84.6 %)
Pit-free CHM	184 (71.3 %)	326 (82.1 %)	34 (87.1 %)
Spike-free DSM	**204 (79.0 %)**	**357 (90 %)**	**33 (84.6 %)**

6.5 Evaluation of spike-free DSMs across different forest types

The quality of a LiDAR-derived DSM largely depends on the quality of the acquired LiDAR data, as well as on forest conditions (Falkowski et al., 2008; Pitkänen et al., 2004; Popescu and Wynne, 2004; Vauhkonen et al., 2012a; Yu et al., 2011). In Chapter 5 the applicability of spike-free DSMs was evaluated for the purpose of tree detection at different LiDAR point densities (high, moderate and low) and for different forest types (a temperate plantation in France, a temperate mixed deciduous-coniferous forest in Germany and a tropical rain-forest in Australia). Chapter 5 statistically compared the accuracy of treetop detection on the spike-free DSM to the accuracies achieved on DSMs generated from first-return, highest-return and last-return LiDAR points.

Although Chapter 5 established that the spike-free DSM significantly improves the accuracy of tree detection across multiple forest types and across different LiDAR point densities, the results did indicate that forest structure as well as the LiDAR point density affect how much a spike-free DSM can improve the accuracy. For example, the best detection result was obtained within the Bois Noir Forest, France (Kappa = 0.85), which consists of coniferous plantation trees with only a small amount of understory scanned with very high point density, while the lowest detection result on a spike-free DSM was obtained at Robson Creek, Australia (Kappa = 0.45), which consists of a mix of multi-layered broad-leaved trees scanned at low point density. As expected, the ITD approach easily identified local maxima of conifers that have a conical crown shape with a distinct apex (e.g. mountain pine trees at Bois Noir Forest), while it was relatively difficult to identify local maxima of broadleaved trees that have a rounded and irregular crown shape (e.g. European beech at Bavarian National Park) or/and have distinct layers of separating crown, which heavily overlap (e.g. Lauraceae species at Robson Creek).

Chapter 5 showed the effect of low LiDAR point density with large variations in the point spacing on the accuracy of treetop detection using the spike-free DSM. This is because the spike-free algorithm relies on a "single" freeze distance for the entire data set, which implicitly assumes a

more or less uniform distance between all neighboring laser pulses. The result of the ITD approach showed a high number of omission errors (undetected trees) in the Robson Creek data, which are scanned by several low-density flight lines with the point density ranging from 1.63 to 10.13 points/m^2 and the pulse spacing ranging from 0.73 to 0.31 m. In area where the freeze distance was significantly larger than the actual pulse spacing, triangles in that area were frozen too early and details, particularly small trees and trees in dense stands with narrow spacing, were lost. These results agree with the observation made in Chapter 4 that a "fixed freeze" distance is not optimal when the pulse spacing varies across a dataset. Ideally, the freeze distance should be constantly adapted to the observed pulse spacing to improve the treetop detection for low point density with irregular pulse spacing.

6.6 Broader usage of a spike-free DSM

The spike-free algorithm improves accuracy of tree detection and, subsequently, offers the possibility of improving accuracy of tree crown extraction and height estimation, which in turn are useful inputs for growth and volume estimation modeling (Popescu et al., 2003). Acquiring accurate individual tree parameters from LiDAR-derived spike-free DSM will have significant applications in a variety of forest activities, including sustainable forest management, biomass estimation, carbon stock estimation, and wildland fire risk assessment at regional and global scale.

Recently, the use of multi-sensoral data based on integrating LiDAR data with hyperspectral or multi-spectral images has attracted much attention for forest applications, including species identification, age, and environmental stress (Erdody and Moskal, 2010; Popescu et al., 2004; Swatantran et al., 2011; Verrelst et al., 2009). In theory, a major limitation of ITD approaches based on LiDAR is the lack of spectral information and a major limitation of ITD approaches based on multispectral imagery is the lack of height information. The integration of LiDAR-derived spike-free DSMs and imagery offers may lead to higher accuracies in extraction of forest parameters.

Initial experiments in Chapter 4 of applying the spike-free algorithm to airborne LiDAR collected over towns and cities showed noticeable improvements in the modeling of urban scenes, especially along the sides of buildings. The spike-free algorithm produces a much cleaner surfaces with better defined edges. The spike-free algorithm will generally produce a cleaner surface for objects that laser pulse can peek under, such as eaves of roofs, covered walkways, or bridges. This could prove useful for automated reconstruction of building outlines from a DSM or similar automated extraction tasks.

6.7 Future research

The current implementation of the spike-free algorithm is sensitive to variations in the actual spacing between laser pulses. This is because of the spike-free algorithm relies on a "single" freeze distance for the entire data. A fixed value for the freeze distance will not be optimal when the pulse spacing varies constantly across the dataset. Wherever a freeze distance larger than the actual pulse spacing is used, triangles will be frozen too early and details, particularly small trees and trees in dense stands with a narrow spacing, will be lost, making it more likely for neighboring crowns to be joined together, and increasing the omission error. Wherever a freeze distance smaller than the actual pulse spacing is used, triangles remain "unfrozen" for too long so "spikes" can reappear in the DSM and cause commission errors. In the future, it may be useful to locally adapt the freeze to the observed pulse spacing in order to further improve the accuracy of the algorithm.

The general performance of the spike-free algorithm was only validated to improve tree detection using one of the ITD approaches (e.g., morphological opening and reconstruction methods). Further tests should be carried out to evaluate if and how much a spike-free DSM improves the accuracy of tree detection for other ITD methods, particularly in tropical forests. As the spike-free algorithm can produce more clearly delineated surfaces with better defined edges, it would be interesting to evaluate how the use of a spike-free DSM affects the derivation of crown area for various crown delineation techniques.

Bibliography

ASPRS. (2008). LAS file format specifications. URL: http://www.asprs.org/a/society/committees/standards/asprs_las_format_v12.

Amiri, N., Yao, W., Heurich, M., Krzystek, P., and Skidmore, A. K. (2016). Estimation of regeneration coverage in a temperate forest by 3D segmentation using airborne laser scanning data. *International Journal of Applied Earth Observation and Geoinformation* **52**, 252-262.

Arnaud, F. o. (1895). "Notice historique sur les torrents de la vallée de l'Ubaye," Impr. Nationale, Paris.

Asner, G. P., and Mascaro, J. (2014). Mapping tropical forest carbon: Calibrating plot estimates to a simple LiDAR metric. *Remote Sensing of Environment* **140**, 614-624.

Axelsson, P. (1999). Processing of laser scanner data—algorithms and applications. *ISPRS Journal of Photogrammetry and Remote Sensing* **54**, 138-147.

Axelsson, P. (2000). DEM generation from laser scanner data using adaptive TIN models. *International Archives of Photogrammetry and Remote Sensing* **33**, 110-117.

Balsa-Barreiro, J., and Lerma, J. L. (2014). A new methodology to estimate the discrete-return point density on airborne lidar surveys. *International Journal of Remote Sensing* **35**, 1496-1510.

Baltsavias, E. P. (1999). Airborne laser scanning: basic relations and formulas. *ISPRS Journal of Photogrammetry and Remote Sensing* **54**, 199-214.

Ben-Arie, J. R., Hay, G. J., Powers, R. P., Castilla, G., and St-Onge, B. (2009). Development of a pit filling algorithm for LiDAR canopy height models. *Computers and Geosciences* **35**, 1940-1949.

Benayas, J. M. R., Newton, A. C., Diaz, A., and Bullock, J. M. (2009). Enhancement of Biodiversity and Ecosystem Services by Ecological Restoration: A Meta-Analysis. *Science* **325**, 1121-1124.

Biging, G. S., and Gill, S. J. (1997). Stochastic Models for Conifer Tree Crown Profiles. *Forest Science* **43**, 25-34.

Bortolot, Z. J., and Wynne, R. H. (2005). Estimating forest biomass using small footprint LiDAR data: An individual tree-based approach that incorporates training data. *ISPRS Journal of Photogrammetry and Remote Sensing* **59**, 342-360.

Bradford, M., Metcalfe, D. J., Ford, A., Liddell, M., and McKeown, A. (2014). Floristics, stand structure and aboveground biomass of a 25-ha rainforest plot in the Wet Tropics of Australia. *Journal of Tropical Forest Science*, 543-553.

Brandtberg, T., Warner, T. A., Landenberger, R. E., and McGraw, J. B. (2003). Detection and analysis of individual leaf-off tree crowns in small footprint, high sampling density lidar data from the eastern deciduous forest in North America. *Remote Sensing of Environment* **85**, 290-303.

Breidenbach, J., Koch, B., Kändler, G., and Kleusberg, A. (2008). Quantifying the influence of slope, aspect, crown shape and stem density on the estimation of tree height at plot level using lidar and InSAR data. *International Journal of Remote Sensing* **29**, 1511-1536.

Brown, S. (2002). Measuring carbon in forests: current status and future challenges. *Environmental Pollution* **116**, 363-372.

Cailleret, M., Heurich, M., and Bugmann, H. (2014). Reduction in browsing intensity may not compensate climate change effects on tree species composition in the Bavarian Forest National Park. *Forest Ecology and Management* **328**, 179-192.

Chan, R. H., Chung-Wa, H., and Nikolova, M. (2005). Salt-and-pepper noise removal by median-type noise detectors and detail-preserving regularization. *Image Processing, IEEE Transactions on* **14**, 1479-1485.

Chen, Q., Baldocchi, D., Gong, P., and Kelly, M. (2006). Isolating individual trees in a savanna woodland using small footprint lidar data. *Photogrammetric Engineering and Remote Sensing* **72**, 923-932.

Chen, Y. X., Qin, K., Liu, Y., Gan, S. Z., and Zhan, Y. (2012). Feature Modelling of High Resolution Remote Sensing Images Considering Spatial Autocorrelation. *International Archives of the Photogrammetry, Remote Sensing and Spatial Information Sciences* **1**, 467-472.

Chew, L. P. (1987). Constrained Delaunay triangulations. *In* "Proceedings of the third annual symposium on Computational geometry", pp. 215-222. ACM, Waterloo, Ontario, Canada.

Chow, T. E., and Hodgson, M. E. (2009). Effects of lidar post-spacing and DEM resolution to mean slope estimation. *International Journal of Geographical Information Science* **23**, 1277-1295.

Clark, M. L., Clark, D. B., and Roberts, D. A. (2004). Small-footprint lidar estimation of sub-canopy elevation and tree height in a tropical rain forest landscape. *Remote Sensing of Environment* **91**, 68-89.

Cohen, J. (1960). A Coefficient of Agreement for Nominal Scales. *Educational and Psychological Measurement* **20**, 37-46.

Congalton, R. G., and Green, K. (1999). "Assessing the accuracy of remotely sensed data: principles and practices," CRC press, Boca Raton, Florida.

Delfinado, C. J. A., and Edelsbrunner, H. (1995). An incremental algorithm for Betti numbers of simplicial complexes on the 3-sphere. *Computer Aided Geometric Design* **12**, 771-784.

Doruska, P. F., and Burkhart, H. E. (1994). Modeling the diameter and locational distribution of branches within the crowns of loblolly pine trees in unthinned plantations. *Canadian Journal of Forest Research* **24**, 2362-2376.

Dralle, K., and Rudemo, M. (1996). Stem number estimation by kernel smoothing of aerial photos. *Canadian Journal of Forest Research* **26**, 1228-1236.

Duncanson, L. I., Cook, B. D., Hurtt, G. C., and Dubayah, R. O. (2014). An efficient, multi-layered crown delineation algorithm for mapping individual tree structure across multiple ecosystems. *Remote Sensing of Environment* **154**, 378-386.

Edelsbrunner, H., and Mücke, E. P. (1994). Three-dimensional alpha shapes. *ACM Transactions on Graphics* **13**, 43-72.

Erdody, T. L., and Moskal, L. M. (2010). Fusion of LiDAR and imagery for estimating forest canopy fuels. *Remote Sensing of Environment* **114**, 725-737.

Eysn, L., Hollaus, M., Lindberg, E., Berger, F., Monnet, J.-M., Dalponte, M., Kobal, M., Pellegrini, M., Lingua, E., Mongus, D., and Pfeifer, N. (2015). A Benchmark of Lidar-Based Single Tree Detection Methods Using Heterogeneous Forest Data from the Alpine Space. *Forests* **6**, 1721.

Falkowski, M. J., Smith, A. M. S., Gessler, P. E., Hudak, A. T., Vierling, L. A., and Evans, J. S. (2008). The influence of conifer forest canopy cover on the accuracy of two individual tree measurement algorithms using lidar data. *Canadian Journal of Remote Sensing* **34**, S338-S350.

Falkowski, M. J., Smith, A. M. S., Hudak, A. T., Gessler, P. E., Vierling, L. A., and Crookston, N. L. (2006). Automated estimation of individual conifer tree height and crown diameter via two-dimensional spatial wavelet analysis of lidar data. *Canadian Journal of Remote Sensing* **32**, 153-161.

Ferraz, A., Bretar, F., Jacquemoud, S., Gonçalves, G., Pereira, L., Tomé, M., and Soares, P. (2012). 3-D mapping of a multi-layered Mediterranean forest using ALS data. *Remote Sensing of Environment* **121**, 210-223.

Ferraz, A., Saatchi, S., Mallet, C., and Meyer, V. (2016). Lidar detection of individual tree size in tropical forests. *Remote Sensing of Environment* **183**, 318-333.

Flageollet, J.-C., Maquaire, O., Martin, B., and Weber, D. (1999). Landslides and climatic conditions in the Barcelonnette and Vars basins (Southern French Alps, France). *Geomorphology* **30**, 65-78.

Fleiss, J. L., Cohen, J., and Everitt, B. (1969). Large sample standard errors of kappa and weighted kappa. *Psychological Bulletin* **72**, 323.

Forzieri, G., Guarnieri, L., Vivoni, E. R., Castelli, F., and Preti, F. (2009). Multiple attribute decision making for individual tree detection using high-resolution laser scanning. *Forest Ecology and Management* **258**, 2501-2510.

Gaveau, D. L., and Hill, R. A. (2003). Quantifying canopy height underestimation by laser pulse penetration in small-footprint airborne laser scanning data. *Canadian Journal of Remote Sensing* **29**, 650-657.

Gebreslasie, M. T., Ahmed, F. B., Van Aardt, J. A. N., and Blakeway, F. (2011). Individual tree detection based on variable and fixed window size local maxima filtering applied to IKONOS imagery for even-aged Eucalyptus plantation forests. *International Journal of Remote Sensing* **32**, 4141-4154.

Hall, R., Watkins, R., Heggem, D., Jones, K., Kaufmann, P., Moore, S., and Gregory, S. (2009). Quantifying structural physical habitat attributes using LIDAR and hyperspectral imagery. *Environmental Monitoring and Assessment* **159**, 63-83.

Heidemann, H. K. (2012). Lidar base specification version 1.0. *US Geological Survey Techniques and Methods*, 63.

Heurich, M. (2008). Automatic recognition and measurement of single trees based on data from airborne laser scanning over the richly structured natural forests of the Bavarian Forest National Park. *Forest Ecology and Management* **255**, 2416-2433.

Heurich, M., Beudert, B., Rall, H., and Křenová, Z. (2010). National Parks as Model Regions for Interdisciplinary Long-Term Ecological Research: The Bavarian Forest and Šumavá National Parks Underway to Transboundary Ecosystem Research. *In* "Long-Term Ecological Research: Between Theory and Application" (F. Müller, C. Baessler, H. Schubert and S. Klotz, eds.), pp. 327-344. Springer Netherlands, Dordrecht.

Heurich, M., Schneider, T., and Kennel, E. (2003). Laser scanning for identification of forest structure in the Bavarian forest national park. *In* "Proc. Scandlaser scientific workshop on airborne laser scanning of forests", pp. 97–106, Umeå.

Heurich, M., and Thoma, F. (2008). Estimation of forestry stand parameters using laser scanning data in temperate, structurally rich natural European beech (Fagus sylvatica) and Norway spruce (Picea abies) forests. *Forestry: An International Journal of Forest Research* **81**, 645-661.

Hollaus, M., Mandlburger, G., Pfeifer, N., and Mücke, W. (2010). Land cover dependent derivation of digital surface models from airborne laser scanning data. *IAPRS* **38**, 1-3.

Holmgren, J., and Persson, Å. (2004). Identifying species of individual trees using airborne laser scanner. *Remote Sensing of Environment* **90**, 415-423.

Holmgren, J., Persson, A., and Soderman, U. (2008). Species identification of individual trees by combining high resolution LIDAR data with multi-spectral images. *International Journal of Remote Sensing* **29**, 1537-1552.

Horn, B. K. P. (1981). Hill shading and the reflectance map. *Proc. IEEE* **69**, 14-47.

Hosoi, F., Matsugami, H., Watanuki, K., Shimizu, Y., and Omasa, K. (2012). Accurate detection of tree apexes in coniferous canopies from airborne scanning light detection and ranging images based on crown-extraction filtering. *Journal of Applied Remote Sensing* **6**.

Hu, B., Li, J., Jing, L., and Judah, A. (2014). Improving the efficiency and accuracy of individual tree crown delineation from high-density LiDAR data. *International Journal of Applied Earth Observation and Geoinformation* **26**, 145-155.

Husch, B., Miller, C. I., and Beers, T. W. (1982). "Forest mensuration," Third/Ed. John Wiley & Sons Inc., New York.

Hyyppä, J., Hyyppä, H., Leckie, D., Gougeon, F., Yu, X., and Maltamo, M. (2008). Review of methods of small-footprint airborne laser scanning for extracting forest inventory data in boreal forests. *International Journal of Remote Sensing* **29**, 1339-1366.

Hyyppä, J., and Inkinen, M. (1999). Detection and estimating attributes for single trees using lasar scanning. *Photogrammetrci Journal of finland* **16**, 27-42.

Hyyppä, J., Kelle, O., Lehikoinen, M., and Inkinen, M. (2001). A segmentation-based method to retrieve stem volume estimates from 3-D tree height models produced by laser scanners. *Ieee Transactions on Geoscience and Remote Sensing* **39**, 969-975.

Hyyppä, J., Pyysalo, U., Hyyppä, H., and Samberg, A. (2000). Elevation accuracy of laser scanning-derived digital terrain and target models in forest environment. *In* "4th Workshop on lidar remote sensing of land and sea. Dresden, Germany: EARSeL".

Hyyppä, J., Yu, X., Hyyppä, H., Vastaranta, M., Holopainen, M., Kukko, A., Kaartinen, H., Jaakkola, A., Vaaja, M., Koskinen, J., and Alho, P. (2012). Advances in Forest Inventory Using Airborne Laser Scanning. *Remote Sensing* **4**, 1190-1207.

Isenburg, M. (2012). The story of LAStools. *In* "Proc. Silvilaser2012". Vancouver, 19 September, Keynote speech.

Isenburg, M., Liu, Y., Shewchuk, J., and Snoeyink, J. (2006a). Streaming computation of Delaunay triangulations. *Proc. ACM Transactions on Graphics* **25**, 1049-1056.

Isenburg, M., Liu, Y., Shewchuk, J., Snoeyink, J., and Thirion, T. (2006b). Generating Raster DEM from Mass Points Via TIN Streaming. *In* "Geographic Information Science" (M. Raubal, H. Miller, A. Frank and M. Goodchild, eds.), Vol. 4197, pp. 186-198. Springer Berlin Heidelberg.

Jing, L., Hu, B., Li, J., and Noland, T. (2012a). Automated delineation of individual tree crowns from LiDAR data by multi-scale analysis and segmentation. *Photogrammetric Engineering & Remote Sensing* **78**, 1275-1284.

Jing, L., Hu, B., Noland, T., and Li, J. (2012b). An individual tree crown delineation method based on multi-scale segmentation of imagery. *ISPRS Journal of Photogrammetry and Remote Sensing* **70**, 88-98.

Kaartinen, H., Hyyppä, J., Yu, X., Vastaranta, M., Hyyppä, H., Kukko, A., Holopainen, M., Heipke, C., Hirschmugl, M., Morsdorf, F., Næsset, E., Pitkänen, J., Popescu, S., Solberg, S., Wolf, B. M., and Wu, J.-C. (2012). An International Comparison of Individual Tree Detection and Extraction Using Airborne Laser Scanning. *Remote Sensing* **4**, 950-974.

Kathuria, A., Turner, R., Stone, C., Duque-Lazo, J., and West, R. (2016). Development of an automated individual tree detection model using point cloud LiDAR data for accurate tree counts in a Pinus radiata plantation. *Australian Forestry* **79**, 126-136.

Kato, A., Moskal, L. M., Schiess, P., Swanson, M. E., Calhoun, D., and Stuetzle, W. (2009). Capturing tree crown formation through implicit surface reconstruction using airborne lidar data. *Remote Sensing of Environment* **113**, 1148-1162.

Ke, Y., Quackenbush, L. J., and Im, J. (2010). Synergistic use of QuickBird multispectral imagery and LIDAR data for object-based forest species classification. *Remote Sensing of Environment* **114**, 1141-1154.

Khoshelham, K., Nardinocchi, C., Frontoni, E., Mancini, A., and Zingaretti, P. (2010). Performance evaluation of automated approaches to building detection in multi-source aerial data. *ISPRS Journal of Photogrammetry and Remote Sensing* **65**, 123-133.

Khosravipour, A., Skidmore, A. K., and Isenburg, M. (2016). Generating spike-free digital surface models using LiDAR raw point clouds: A new approach for forestry applications. *International Journal of Applied Earth Observation and Geoinformation* **52**, 104-114.

Khosravipour, A., Skidmore, A. K., Isenburg, M., Wang, T., and Hussin, Y. A. (2014). Generating Pit-free Canopy Height Models from Airborne Lidar. *Photogrammetric Engineering & Remote Sensing* **80**, 863-872.

Khosravipour, A., Skidmore, A. K., Wang, T., Isenburg, M., and Khoshelham, K. (2015). Effect of slope on treetop detection using a LiDAR Canopy Height Model. *ISPRS Journal of Photogrammetry and Remote Sensing* **104**, 44-52.

Koch, B., Heyder, U., and Weinacker, H. (2006). Detection of individual tree crowns in airborne lidar data. *Photogrammetric Engineering and Remote Sensing* **72**, 357-363.

Kraus, K., and Pfeifer, N. (1998). Determination of terrain models in wooded areas with airborne laser scanner data. *ISPRS Journal of Photogrammetry and Remote Sensing* **53**, 193-203.

Latifi, H. (2012). "Characterizing forest structure by means of remote sensing: A review," INTECH Open Access Publisher.

Latifi, H., Fassnacht, F. E., Müller, J., Tharani, A., Dech, S., and Heurich, M. (2015). Forest inventories by LiDAR data: A comparison of single tree segmentation and metric-based methods for inventories

of a heterogeneous temperate forest. *International Journal of Applied Earth Observation and Geoinformation* **42**, 162-174.

Leckie, D., Gougeon, F., Hill, D., Quinn, R., Armstrong, L., and Shreenan, R. (2003). Combined high-density lidar and multispectral imagery for individual tree crown analysis. *Canadian Journal of Remote Sensing* **29**, 633-649.

Lefsky, M. A., Cohen, W. B., Parker, G. G., and Harding, D. J. (2002). Lidar remote sensing for ecosystem studies. *Bioscience* **52**, 19-30.

Li, J., Hu, B., and Noland, T. L. (2013). Classification of tree species based on structural features derived from high density LiDAR data. *Agricultural and Forest Meteorology* **171–172**, 104-114.

Li, W., Guo, Q., Jakubowski, M. K., and Kelly, M. (2012). A New Method for Segmenting Individual Trees from the Lidar Point Cloud. *Photogrammetric Engineering & Remote Sensing* **78**, 75-84.

Lichstein, J. W., Dushoff, J., Ogle, K., Chen, A., Purves, D. W., Caspersen, J. P., and Pacala, S. W. (2010). Unlocking the forest inventory data: relating individual tree performance to unmeasured environmental factors. *Ecological Applications* **20**, 684-699.

Lim, K., Hopkinson, C., and Treitz, P. (2008). Examining the effects of sampling point densities on laser canopy height and density metrics. *Forestry Chronicle* **84**, 876-885.

Lim, K., Treitz, P., Baldwin, K., Morrison, I., and Green, J. (2003a). Lidar remote sensing of biophysical properties of tolerant northern hardwood forests. *Canadian Journal of Remote Sensing* **29**, 658-678.

Lim, K., Treitz, P., Wulder, M., St-Onge, B., and Flood, M. (2003b). LiDAR remote sensing of forest structure. *Progress in Physical Geography* **27**, 88-106.

Liu, Q., Li, Z., Chen, E., Pang, Y., Tian, X., and Cao, C. (2010). Estimating biomass of individual trees using point cloud data of airborne LIDAR. *Gaojishu Tongxin/Chinese High Technology Letters* **20**, 765-770.

Lu, X., Guo, Q., Li, W., and Flanagan, J. (2014). A bottom-up approach to segment individual deciduous trees using leaf-off lidar point cloud

data. *ISPRS Journal of Photogrammetry and Remote Sensing* **94**, 1-12.

Maclean, G. A., and Martin, G. L. (1984). Merchantable timber volume estimation using cross-sectional photogrammetric and densitometric methods. *Canadian Journal of Forest Research* **14**, 803-810.

Magnussen, S., Næsset, E., and Gobakken, T. (2010). Reliability of LiDAR derived predictors of forest inventory attributes: A case study with Norway spruce. *Remote Sensing of Environment* **114**, 700-712.

Martinuzzi, S., Vierling, L. A., Gould, W. A., Falkowski, M. J., Evans, J. S., Hudak, A. T., and Vierling, K. T. (2009). Mapping snags and understory shrubs for a LiDAR-based assessment of wildlife habitat suitability. *Remote Sensing of Environment* **113**, 2533-2546.

Mongus, D., and Žalik, B. (2015). An efficient approach to 3D single tree-crown delineation in LiDAR data. *ISPRS Journal of Photogrammetry and Remote Sensing* **108**, 219-233.

Monnet, J.-M., Mermin, É., Chanussot, J., and Berger, F. (2010). Tree top detection using local maxima filtering: a parameter sensitivity analysis. *Proceedings of Silvilaser 2010*.

Morsdorf, F., Meier, E., Kötz, B., Itten, K. I., Dobbertin, M., and Allgöwer, B. (2004). LIDAR-based geometric reconstruction of boreal type forest stands at single tree level for forest and wildland fire management. *Remote Sensing of Environment* **92**, 353-362.

Murphy, H. T., Bradford, M. G., Dalongeville, A., Ford, A. J., and Metcalfe, D. J. (2013). No evidence for long-term increases in biomass and stem density in the tropical rain forests of Australia. *Journal of Ecology* **101**, 1589-1597.

Næsset, E. (2002). Predicting forest stand characteristics with airborne scanning laser using a practical two-stage procedure and field data. *Remote Sensing of Environment* **80**, 88-99.

Næsset, E., and Økland, T. (2002). Estimating tree height and tree crown properties using airborne scanning laser in a boreal nature reserve. *Remote Sensing of Environment* **79**, 105-115.

Nelson, R., Krabill, W., and MacLean, G. (1984). Determining forest canopy characteristics using airborne laser data. *Remote Sensing of Environment* **15**, 201-212.

Nelson, R., Krabill, W., and Tonelli, J. (1988). Estimating forest biomass and volume using airborne laser data. *Remote Sensing of Environment* **24**, 247-267.

Nygren, P., Rebottaro, S., and Chavarría, R. (1993). Application of the pipe model theory to non-destructive estimation of leaf biomass and leaf area of pruned agroforestry trees. *Agroforestry Systems* **23**, 63-77.

Nyquist, H. (1928). Certain topics in telegraph transmission theory. *Trans.Amer. Inst. Electr. Eng* **47**, 617–644.

Office National des Forêts, 2000. The National Forests Office (France), URL: http://www.onf.fr/, Paris, France (last data accessed: 30 June 2014).

Palace, M. W., Sullivan, F. B., Ducey, M. J., Treuhaft, R. N., Herrick, C., Shimbo, J. Z., and Mota-E-Silva, J. (2015). Estimating forest structure in a tropical forest using field measurements, a synthetic model and discrete return lidar data. *Remote Sensing of Environment* **161**, 1-11.

Patenaude, G., Milne, R., and Dawson, T. P. (2005). Synthesis of remote sensing approaches for forest carbon estimation: reporting to the Kyoto Protocol. *Environmental Science & Policy* **8**, 161-178.

Persson, Å., Holmgren, J., and Soderman, U. (2002). Detecting and measuring individual trees using an airborne laser scanner. *Photogrammetric Engineering and Remote Sensing* **68**, 925-932.

Pettorelli, N., Wegmann, M., Skidmore, A., Mücher, S., Dawson, T. P., Fernandez, M., Lucas, R., Schaepman, M. E., Wang, T., and O'Connor, B. (2016). Framing the concept of satellite remote sensing essential biodiversity variables: challenges and future directions. *Remote Sensing in Ecology and Conservation*.

Pierce, K. B., Ohmann, J. L., Wimberly, M. C., Gregory, M. J., and Fried, J. S. (2009). Mapping wildland fuels and forest structure for land management: a comparison of nearest neighbor imputation and

other methods. *Canadian Journal of Forest Research* **39**, 1901-1916.

Pitkänen, J., Maltamo, M., Hyyppä, J., and Yu, X. (2004). Adaptive methods for individual tree detection on airborne laser based canopy height model. *International Archives of Photogrammetry, Remote Sensing and Spatial Information Sciences* **36**, 187-191.

Pond, N. C., Froese, R. E., and Nagel, L. M. (2014). Sustainability of the Selection System in Northern Hardwood Forests. *Forest Science* **60**, 374-381.

Popescu, S. C. (2007). Estimating biomass of individual pine trees using airborne lidar. *Biomass and Bioenergy* **31**, 646-655.

Popescu, S. C., and Wynne, R. H. (2004). Seeing the trees in the forest: Using lidar and multispectral data fusion with local filtering and variable window size for estimating tree height. *Photogrammetric Engineering and Remote Sensing* **70**, 589-604.

Popescu, S. C., Wynne, R. H., and Nelson, R. F. (2003). Measuring individual tree crown diameter with lidar and assessing its influence on estimating forest volume and biomass. *Canadian Journal of Remote Sensing* **29**, 564-577.

Popescu, S. C., Wynne, R. H., and Scrivani, J. A. (2004). Fusion of small-footprint lidar and multispectral data to estimate plot-level volume and biomass in deciduous and pine forests in Virginia, USA. *Forest Science* **50**, 551-565.

Pouliot, D., King, D., and Pitt, D. (2005). Development and evaluation of an automated tree detection delineation algorithm for monitoring regenerating coniferous forests. *Canadian Journal of Forest Research* **35**, 2332-2345.

Pouliot, D. A., King, D. J., Bell, F. W., and Pitt, D. G. (2002). Automated tree crown detection and delineation in high-resolution digital camera imagery of coniferous forest regeneration. *Remote Sensing of Environment* **82**, 322-334.

Rapidlasso GmbH, LAStools Rapid LiDAR Processing, URL: http://www.rapidlasso.com, Gilching, Germany (last data accessed: 30 June 2017).

Razak, K. A., Bucksch, A., Straatsma, M., Van Westen, C. J., Bakar, R. A., and De Jong, S. M. (2013). High density airborne LIDAR estimation of disrupted trees induced by landslides. *In* "Proc. International Geoscience and Remote Sensing Symposium", pp. 2617-2620, Melbourne.

Razak, K. A., Buksch, A., Damen, M. C. J., van Westen, C. J., Straatsma, M. W., and de Jong, S. (2011a). Characterizing tree growth anomaly induced by landslides using LiDAR. *In* "Proc. 2nd World Landslide Forum", pp. 235-241, Rome.

Razak, K. A., Straatsma, M. W., van Westen, C. J., Malet, J. P., and de Jong, S. M. (2011b). Airborne laser scanning of forested landslides characterization: Terrain model quality and visualization. *Geomorphology* **126**, 186-200.

Reitberger, J., Krzystek, P., and Stilla, U. (2009a). Benefit of airborne full waveform lidar for 3D segmentation and classification of single trees. *In* "ASPRS 2009 Annual Conference", pp. 1–9.

Reitberger, J., Schnörr, C., Krzystek, P., and Stilla, U. (2009b). 3D segmentation of single trees exploiting full waveform LIDAR data. *ISPRS Journal of Photogrammetry and Remote Sensing* **64**, 561-574.

RIEGL, 2015. Datasheet RIEGL-VQ480i. URL: http://www.riegl.com (accessed10.04.15.).

Rosenqvist, Å., Milne, A., Lucas, R., Imhoff, M., and Dobson, C. (2003). A review of remote sensing technology in support of the Kyoto Protocol. *Environmental Science & Policy* **6**, 441-455.

Ross, J., Kellomäki, S., Oker-Blom, P., Ross, V., and Vilikainen, L. (1986). Architecture of Scots pine crown: phytometrical characteristics of needles and shoots. *Silva Fennica* **20**, 91-105.

Rouvinen, S., and Kuuluvainen, T. (1997). Structure and asymmetry of tree crowns in relation to local competition in a natural mature Scots pine forest. *Canadian Journal of Forest Research* **27**, 890-902.

Säynäjoki, R., Packalén, P., Maltamo, M., Vehmas, M., and Eerikäinen, K. (2008). Detection of Aspens Using High Resolution Aerial

Laser Scanning Data and Digital Aerial Images. *Sensors* **8**, 5037-5054.

Serra, J. (1982). "Image analysis and mathematical morphology," Academic Press Inc., London.

Shamsoddini, A., Turner, R., and Trinder, J. C. (2013). Improving lidar-based forest structure mapping with crown-level pit removal. *Journal of Spatial Science* **58**, 29-51.

Shih, P., and Huang, C.-M. (2006). Airborne LiDAR point cloud density indices. *In* "AGU Fall Meeting Abstracts", Vol. 1, pp. 0919.

Skidmore, A. K., Pettorelli, N., Coops, N. C., Geller, G. N., Hansen, M., Lucas, R., Müncher, C. A., O'Connor, B., Paganini, M., Pereira, H. M., Schaepman, M. E., Turner, W., Wang, T. J., and Wegmann, M. (2015). Environmental science : agree on biodiversity metrics to track from space : comment. *Nature : international weekly journal of science* **523**, 403-405.

Solberg, S., Naesset, E., and Bollandsas, O. M. (2006). Single tree segmentation using airborne laser scanner data in a structurally heterogeneous spruce forest. *Photogrammetric Engineering and Remote Sensing* **72**, 1369-1378.

Song, C., Dickinson, M. B., Su, L., Zhang, S., and Yaussey, D. (2010). Estimating average tree crown size using spatial information from Ikonos and QuickBird images: Across-sensor and across-site comparisons. *Remote Sensing of Environment* **114**, 1099-1107.

Spies, T. A. (1998). Forest structure: a key to the ecosystem. *Northwest science* **72**, 34-36.

Spurr, S. H. (1951). "Forest inventory," Ronald Press Co., New York.

Swatantran, A., Dubayah, R., Roberts, D., Hofton, M., and Blair, J. B. (2011). Mapping biomass and stress in the Sierra Nevada using lidar and hyperspectral data fusion. *Remote Sensing of Environment* **115**, 2917-2930.

Takahashi, T., Yamamoto, K., Senda, Y., and Tsuzuku, M. (2005). Estimating individual tree heights of sugi (Cryptomeria japonica D. Don) plantations in mountainous areas using small-footprint airborne LiDAR. *Journal of Forest Research* **10**, 135-142.

Thiery, Y., Malet, J. P., Sterlacchini, S., Puissant, A., and Maquaire, O. (2007). Landslide susceptibility assessment by bivariate methods at large scales: Application to a complex mountainous environment. *Geomorphology* **92**, 38-59.

Tobler, W. R. (1970). A Computer Movie Simulating Urban Growth in the Detroit Region. *Economic Geography* **46**, 234-240.

Turner, W., Spector, S., Gardiner, N., Fladeland, M., Sterling, E., and Steininger, M. (2003). Remote sensing for biodiversity science and conservation. *Trends in Ecology & Evolution* **18**, 306-314.

Vallet, J., and Skaloud, J. (2004). Development and Experiences with A Fully-Digital Handheld Mapping System Operated from A Helicopter. *International Archives of Photogrammetry, Remote Sensing and Spatial Information Sciences* **35 (Part B)**, 791-796.

Van Leeuwen, M., Coops, N. C., and Wulder, M. A. (2010). Canopy surface reconstruction from a LiDAR point cloud using Hough transform. *Remote Sensing Letters* **1**, 125-132.

Vastaranta, M., Holopainen, M., Yu, X., Hyyppä, J., Mäkinen, A., Rasinmäki, J., Melkas, T., Kaartinen, H., and Hyyppä, H. (2011). Effects of Individual Tree Detection Error Sources on Forest Management Planning Calculations. *Remote Sensing* **3**, 1614-1626.

Vastaranta, M., Kankare, V., Holopainen, M., Yu, X., Hyyppä, J., and Hyyppä, H. (2012). Combination of individual tree detection and area-based approach in imputation of forest variables using airborne laser data. *ISPRS Journal of Photogrammetry and Remote Sensing* **67**, 73-79.

Vauhkonen, J., Ene, L., Gupta, S., Heinzel, J., Holmgren, J., Pitkänen, J., Solberg, S., Wang, Y., Weinacker, H., Hauglin, K. M., Lien, V., Packalén, P., Gobakken, T., Koch, B., Næsset, E., Tokola, T., and Maltamo, M. (2012a). Comparative testing of single-tree detection algorithms under different types of forest. *Forestry* **85**, 27-40.

Vauhkonen, J., Holopainen, M., Kankare, V., Vastaranta, M., and Viitala, R. (2015). Geometrically explicit description of forest canopy based on 3D triangulations of airborne laser scanning data. *Remote Sensing of Environment* **173**, 248–257.

Vauhkonen, J., Seppänen, A., Packalén, P., and Tokola, T. (2012b). Improving species-specific plot volume estimates based on airborne laser scanning and image data using alpha shape metrics and balanced field data. *Remote Sensing of Environment* **124**, 534-541.

Véga, C., and Durrieu, S. (2011). Multi-level filtering segmentation to measure individual tree parameters based on Lidar data: Application to a mountainous forest with heterogeneous stands. *International Journal of Applied Earth Observation and Geoinformation* **13**, 646-656.

Véga, C., Hamrouni, A., El Mokhtari, S., Morel, J., Bock, J., Renaud, J. P., Bouvier, M., and Durrieu, S. (2014). PTrees: A point-based approach to forest tree extraction from lidar data. *International Journal of Applied Earth Observation and Geoinformation* **33**, 98-108.

Verrelst, J., Geerling, G. W., Sykora, K. V., and Clevers, J. G. P. W. (2009). Mapping of aggregated floodplain plant communities using image fusion of CASI and LiDAR data. *International Journal of Applied Earth Observation and Geoinformation* **11**, 83-94.

Vincent, L. (1993). Morphological grayscale reconstruction in image analysis: applications and efficient algorithms. *IEEE Transactions on Image Analysis* **2**, 176-201.

Vosselman, G. (2008). Analysis of planimetric accuracy of airborne laser scanning surveys. *International Archives of Photogrammetry, Remote Sensing and Spatial Information Sciences* **37**, 99-104.

Wang, L., Gong, P., and Biging, G. S. (2004). Individual tree-crown delineation and treetop detection high-spatial-resolution aerial imagery. *Photogrammetric Engineering and Remote Sensing* **70**, 351-357.

Wehr, A., and Lohr, U. (1999). Airborne laser scanning—an introduction and overview. *ISPRS Journal of Photogrammetry and Remote Sensing* **54**, 68-82.

White, J. C., Coops, N. C., Wulder, M. A., Vastaranta, M., Hilker, T., and Tompalski, P. (2016). Remote Sensing Technologies for

Enhancing Forest Inventories: A Review. *Canadian Journal of Remote Sensing*, 1-23.

Wilkes, P., Jones, S. D., Suarez, L., Haywood, A., Mellor, A., Woodgate, W., Soto-Berelov, M., and Skidmore, A. K. (2015). Using discrete-return airborne laser scanning to quantify number of canopy strata across diverse forest types. *Methods in Ecology and Evolution*.

Woodgate, W., Jones, S. D., Suarez, L., Hill, M. J., Armston, J. D., Wilkes, P., Soto-Berelov, M., Haywood, A., and Mellor, A. (2015). Understanding the variability in ground-based methods for retrieving canopy openness, gap fraction, and leaf area index in diverse forest systems. *Agricultural and Forest Meteorology* **205**, 83-95.

Woodgate, W., Soto-Berelov, M., Suarez, L., Jones, S. D., Hill, M. J., Wilkes, P., Axelsson, C., Haywood, A., and Mellor, A. (2012). Searching for the Optimal Sampling Design for Measuring LAI in an Upland Rainforest. *In* "GSR".

Wu, B., Yu, B., Wu, Q., Huang, Y., Chen, Z., and Wu, J. (2016). Individual tree crown delineation using localized contour tree method and airborne LiDAR data in coniferous forests. *International Journal of Applied Earth Observation and Geoinformation* **52**, 82-94.

Wulder, M., Niemann, K. O., and Goodenough, D. G. (2000). Local Maximum Filtering for the Extraction of Tree Locations and Basal Area from High Spatial Resolution Imagery. *Remote Sensing of Environment* **73**, 103-114.

Wulder, M. A., Bater, C. W., Coops, N. C., Hilker, T., and White, J. C. (2008). The role of LiDAR in sustainable forest management. *The Forestry Chronicle* **84**, 807-826.

Wulder, M. A., White, J. C., Nelson, R. F., Næsset, E., Ørka, H. O., Coops, N. C., Hilker, T., Bater, C. W., and Gobakken, T. (2012). Lidar sampling for large-area forest characterization: A review. *Remote Sensing of Environment* **121**, 196-209.

Yao, W., Krzystek, P., and Heurich, M. (2012). Tree species classification and estimation of stem volume and DBH based on single tree extraction by exploiting airborne full-waveform LiDAR data. *Remote Sensing of Environment* **123**, 368-380.

Yu, X., Hyyppä, J., Vastaranta, M., Holopainen, M., and Viitala, R. (2011). Predicting individual tree attributes from airborne laser point clouds based on the random forests technique. *ISPRS Journal of Photogrammetry and Remote Sensing* **66**, 28-37.

Zhang, J., Sohn, G., and Brédif, M. (2014). A hybrid framework for single tree detection from airborne laser scanning data: A case study in temperate mature coniferous forests in Ontario, Canada. *ISPRS Journal of Photogrammetry and Remote Sensing* **98**, 44-57.

Zhao, D., Pang, Y., Li, Z., and Sun, G. (2013). Filling invalid values in a lidar-derived canopy height model with morphological crown control. *International Journal of Remote Sensing* **34**, 4636-4654.

Zhao, K., Popescu, S., and Nelson, R. (2009). Lidar remote sensing of forest biomass: A scale-invariant estimation approach using airborne lasers. *Remote Sensing of Environment* **113**, 182-196.

Zhen, Z., Quackenbush, L. J., and Zhang, L. (2016). Trends in Automatic Individual Tree Crown Detection and Delineation—Evolution of LiDAR Data. *Remote Sensing* **8**, 333.

Summary

Individual tree detection (ITD) using airborne LiDAR data plays an increasingly significant role in the efficient and accurate monitoring and managing of forest activities. A first step in detecting individual trees using LiDAR data is the generation of a Digital Surface Model (DSM) or a normalized Digital Surface Model (nDSM/CHM) that describes the geometry of the uppermost layer of the canopy. A DSM or a nDSM/CHM is typically calculated by interpolating first-return LiDAR points. Various ITD approaches then identify local maxima in the resulting elevation or height rasters. ITD approaches trying to identify all "true" treetops are strongly affected by the quality of the LiDAR-derived rasters, which in turn are determined by factors such as the quality of the acquired LiDAR point clouds, the pre-processing, the post-processing, as well as the forest conditions and the complexity of the terrain.

The aim of this thesis is to develop a new approach for generating a high quality LiDAR-derived DSM that improves the accuracy of individual tree detection across multiple forest types and LiDAR point densities. The research in this thesis firstly presents a new "pit-free" algorithm able to create a pit-free CHM raster and efficiently remove those canopy height variations (called *pits* in a raster and *spikes* in a TIN) that cause difficulty in detecting individual trees. The algorithm operates robustly on high- and low-density LiDAR data and significantly improves the accuracy of tree detection in comparison to the accuracies achieved using a smoothed first-return CHM. As complex forest terrain presents a challenging problem for the performance of the height normalization step by distorting the normalized DSM (nDSM/CHM), the thesis subsequently aims to quantify the effect of slope on the accuracy of treetop detection in a pit-free LiDAR-derived CHM. To avoid the height normalization step, the research moves on to develop a novel "spike-free" algorithm that can directly generate a DSM (without the need to normalize) at the highest possible resolution using all relevant LiDAR returns. This algorithm considers all LiDAR returns (not just the first returns), while systematically preventing the formation of spikes during the TIN construction process. This spike-free algorithm significantly improves the accuracy of tree detection across

multiple forest sites (a temperate plantation in France, a temperate mixed deciduous-coniferous forest in Germany and a tropical rain-forest in Australia) and across different LiDAR point densities. The algorithm offers the possibility of improving accuracy of crown delineation, height estimation, and other biophysical parameters at both a regional and global scale.

Samenvatting

Individuele Boom Detectie (ITD) gebaseerd op LiDAR data speelt een steeds grotere rol bij het efficiënt en nauwkeurig volgen en manipuleren van bos processen. Een eerst stap in het herkennen van individuele bomen, gebruikmakend van LiDAR gegevens, is het genereren van een Digital Surface Model (DSM) of een genormaliseerd Digital Surface Model (nDSM/CHM) dat de geometrie van de allerbovenste laag van de vegetatie beschrijft. Een DSM of een nDSM/CHM wordt over het algemeen berekend door 'first-return' LiDAR punten te interpoleren. Vervolgens zijn er verschillende wijzen waarop ITD kan worden aangepakt om lokale maxima te identificeren in de resulterende hoogte rasters. Een ITD aanpak waarbij getracht wordt alle 'ware' boomkruinen te identificeren, wordt sterk beïnvloed door de kwaliteit van de met LiDAR geproduceerde rasters, welke zelf weer afhankelijk zijn van factoren zoals de kwaliteit van de verkregen LiDAR 'point clouds', de gegevens verwerking, zowel van tevoren als achteraf, als van de complexiteit van het bos en het terrein zelf.

Het doel van dit onderzoek is om op een nieuwe wijze een op LiDAR gebaseerde DSM van hoge kwaliteit te genereren, die de exactheid van de detectie van individuele bomen verbetert voor zowel verschillende bos typen als LiDAR punt dichtheden. Het onderzoek presenteert eerst een nieuw 'pit-free' algoritme, dat een 'pit-free' CHM raster kan creëren en op efficiënte wijze variaties in de kruin hoogte kan verwijderen (in een raster 'pits' en in een TIN 'spikes' genoemd), die het moeilijk maken om individuele bomen te onderscheiden. Dit algoritme werkt robuust bij zowel hoge- als lage-dichtheid LiDAR data en verbetert de kwaliteit van boom detectie sterk in vergelijking met uitkomsten van een 'smoothed first-return' CHM. Omdat complex terrein een grote uitdaging vormt bij de stap waar hoogtes worden genormaliseerd, doordat de genormaliseerde DSM (nDSM/CHM) dan wordt verwrongen, poogt dit onderzoek vervolgens om het effect van helling op de nauwkeurigheid van boomtop detectie te kwantificeren in een 'pit-free', op LiDAR gebaseerde CHM. Om de stap van hoogte normalisatie te vermijden, wordt getracht een nieuw, 'spike-free' algoritme te ontwikkelen, dat zonder normalisatie een DSM kan

genereren met de hoogste resolutie, gebruikmakend van alle relevante LiDAR ‘returns’. Dit algoritme maakt gebruik van alle LiDAR ‘returns’ (niet alleen van de ‘first returns’), tegelijkertijd voorkomend dat er gedurende het TIN constructie proces ‘spikes’ worden gevormd. Dit ‘spike-free’ algoritme verbetert de detectie van bomen significant in verschillende bos typen (een plantage in gematigd klimaat in Frankrijk, een gemengd loof-naaldbos in gematigd klimaat in Duitsland en een tropisch regenwoud in Australië) alsmede voor verschillende LiDAR punt dichtheden. Dit algoritme presenteert een wijze om de kwaliteit te verbeteren van kruin herkenning, hoogte schattingen en andere biofysische parameters op zowel regionaal als wereld niveau

ITC Dissertation List

https://www.itc.nl/Pub/research_programme/Research-review-and-output/PhD-Graduates